KAUNAS UNIVERSITY OF TECHNOLOGY

NORA ŠLEKIENĖ

FUNCTIONALISATION OF GRAPHENE/GRAPHENE OXIDE AND THE APPLICATION OF IT AND ITS DERIVATIVES IN NANOMEDICINE

Doctoral Dissertation

Technological sciences, Chemical engineering (05T)

2016, KAUNAS

UDK 546.26 + 615](043.3)

Scientific Supervisor:

Prof. Habil. Dr Valentinas SNITKA (Kaunas University of Technology, Technological sciences, Chemical engineering, 05T).

This doctoral dissertation has been published in:
http://ktu.edu

English Language Editor:

UAB "Synergium"

KAUNO TECHNOLOGIJOS UNIVERSITETAS

NORA ŠLEKIENĖ

GRAFENO / GRAFENO OKSIDO FUNKCIONALIZAVIMAS IR JO BEI JO DARINIŲ TAIKYMAS NANOMEDICINOJE

Daktaro disertacija

Technologijos mokslai, chemijos inžinerija (05T)

2016, KAUNAS

TABLE OF CONTENTS

LIST OF ABBREVIATIONS

AFM- atom force microscopy
BLM- bilayer lipid membrane
BSA- bovine serum albumin
CHO- Chinese hamster ovary
CNT- carbon nanotubes
CVD- chemical vapour deposition
DLS- dynamic light scattering
DOPC-1,2-dioleoyl-*sn*-glycero-3-phosphocholine
DOPE- 1,2-dioleoyl-*sn*-glycero-3-phosphoethanolamine
DOPS-1,2-dioleoyl-*sn*-glycero-3-phospho-*L*-serine
DOX- doxorubicin
EDX- energy dispersive X-Ray spectroscopy
FCS- fluorescence correlation spectroscopy
FeTPPS$_4$- iron meso-tetra (4-sulfonatophenyl) porphine
FTIR- Fourier transform infrared spectroscopy
G- graphene
GO- graphene oxide
HOMO- highest occupied molecular orbital
HP- hematoporphyrin
LM- lipid membrane
LOM- light optical microscopy
LUMO- lowest unoccupied molecular orbital
MH-22A- mouse hepatoma MH-22A
MWCNT- multi-walled carbon nanotubes
NP-nanoparticle
PdI- polydispersity index
PBS- phosphate-buffered saline
SA- sulphuric acid
SAF- supercritical angle fluorescence
SAM- self-assembled monolayers
SEM- scanning electron microscopy
SERS- surface-enhanced Raman spectroscopy
SPM- scanning probe microscopy
SWCNT- single-walled carbon nanotubes
TERS- tip-enhanced Raman spectroscopy
TPyP- meso-tetra (4-pyridyl) porphine
TPPS$_4$- 5,10,15,20-tetrakis (4-sulfonatophenyl) porphine
UAF- undercritical angle fluorescence

LIST OF FIGURES

LIST OF TABLES

1   INTRODUCTION

"Graphene may be the most remarkable substance ever discovered. But what's it for?"- John Colapinto, a staff writer at The New Yorker.

After Andre Geim, a physics professor at the University of Manchester, and a colleague Kostya Novoselov discovered an unusual new material called graphene; he wrote a three-page paper describing their discoveries. It was twice rejected by the journal Nature, where reviewers stated that isolating a stable, two-dimensional material is impossible and that it was not a sufficient scientific advance. Indeed, in 2004 the paper, "Electric Field Effect in Atomically Thin Carbon Films" was published in Science, and it astonished scientists - science fiction had become reality.

Graphene, the two-dimensional sp^2-hybridised carbon, is currently the most intensively studied material. This single-atom-thick sheet of carbon atoms situated in a honeycomb pattern is the world's strongest and thinnest material, also being an excellent conductor of both electricity and heat. From the application viewpoint, this two-dimensional material is considered to be more promising than other nanostructured carbon allotropes (1-dimensional nanotubes or 0-dimensional fullerenes) (Georgakilas et al., 2012).

The intensive research about graphene in recent years is promising a revolution in chemical and electrical engineering. Chemical Engineering of graphene-based materials applies physical sciences (nanographene for improving drilling fluids performance, integrated graphene dispersion to create high performance fluids, graphene-enhanced composites added to rubber to increase its strength, conductivity and impermeability, etc.) and life sciences. The bio-applications of graphene and its derivatives is due to many desirable properties, such as a high specific surface area (2,630 m^2/g), mechanical strength (Young's modulus, ~1,100 GPa), electrical conductivity (200,000 cm^2 V^{-1} s^{-1}), thermal conductivity (~5,000 W/m/K) of graphene and bio-compatibility, low cost, scalable production and facile biological/chemical functionalisation of GO (Jiang, 2011; Guo and Dong, 2011). Graphene oxide easily combines with many other nanoscale materials leading to new applications in the fields of drug delivery, cancer therapeutics, tissue engineering, diagnostics and bioimaging (Wu, An and Hulme, 2015).

The critical issue to be resolved before further applications of graphene in nanomedicine is the potential short and long-term toxicity of this new nanomaterial. Many previous investigations have shown GO and its hybrid structures to induce low cell toxicity, but reports remain conflicting. A number of groups have performed experiments to explore the suitability in nanomedicine and effects of graphene, but this question still is not properly understood and needs further investigations.

The aim of the thesis is the synthesis of new hybrid nanostructures by functionalisation of graphene/graphene oxide with porphyrins and doxorubicin, also the investigation and evaluation of it as a possible drug delivery platform in nanomedicine.

Objectives of the thesis

1) Development and optimisation of methods for the functionalisation of graphene/graphene oxide nanoparticles with organic molecules and characterisation of physicochemical properties of functionalised structures.

2) Development and optimisation of methods to synthesise new hybrid macromolecules using graphene oxide with organic molecules and characterisation of synthesised macromolecules.

3) Analysis of graphene oxide nanoparticles interaction with lipid membranes, as a model for nanoparticles interaction with bio-membranes.

4) Determining the mechanism of graphene oxide transfer into the living cell and the possible toxicity of graphene oxide in different cell lines.

5) Determining the toxicity of functionalised graphene oxide with doxorubicin for cancer cells.

Scientific novelty

During this study, the novel methodology of graphene oxide functionalisation with hematoporphyrin (GO-HP) by chemical covalent binding was designed. New graphene-based hybrid nanostructures (GO-HP) and macromolecules (GO/TPyP) were synthesised. The interaction of GO, ZnO and TiO_2 nanoparticles with lipid membranes was performed and the influence of nanoparticles on lipid membranes dynamics and membranes disruption was evaluated.

For the first time, the impact of graphene oxide and graphene oxide with protein "corona" on the viability of different cell lines (Chinese hamster ovary and mouse hepatoma MH-22A cells) and the impact of functionalised graphene oxide with doxorubicin on the viability of mouse hepatoma MH-22A cells were evaluated.

Defended statements

1. The synthesised graphene and porphyrin structures could be interconnected through non-covalent interactions and in the case of grapheme oxide and porphyrin, through both non-covalent interactions and covalent bonds.

2. Due to the different physicochemical properties of GO, ZnO and TiO_2 (e.g. size of nanoparticles, shape, zeta potential) they exhibit different mechanisms of interaction with synthesised lipid membranes (formed of DOPS and DOPC phospholipids).

3. MH-22A cancerous cells are better at absorbing graphene oxide nanoparticles than healthy CHO cells.

4. Functionalisation of GO with doxorubicin enhances the anticancer effect of doxorubicin. The concentration of the toxic anticancer drug doxorubicin can be

reduced more than 10,000 times by using a hybrid compound of graphene oxide and doxorubicin.

Outline of the dissertation

The dissertation consists of an introduction (section I), literature overview (section II), materials and research methodology (section III), experimental part results and discussion (section IV), conclusions (section V), list of references (section 6) and the list of publications and conferences. The material of the dissertation is presented in 133 pages, including 76 figures and 10 tables.

Approbation of the research results

The results of this thesis are presented in four (4) publications corresponding to the list of the Web of Science database by Thomson Reuters; one (1) publication published in the journal referred to in international databases and presented at ten (10) international conferences (3 invited presentations) and 2 seminars.

Practical significance of the dissertation. Part of the results obtained during the preparation of the dissertation were used in the successfully implemented project "Nanoscopic investigation of structural transformations of proteins at the nano-bio-interfaces" (NanoProt, 2013-2015).

2 REVIEW OF THE LITERATURE

2.1 Nanotechnology in medicine

The medical application of nanotechnology (nanomedicine) (Andrew, 1999) is the medical applications of nanomaterials/nanoparticles and biological devices, to nanoelectronic biosensors and biological machines. Current problems for nanomedicine involve understanding the issues related to toxicity and the environmental impact of nanoparticles. Carbon based nanoparticles are promising due their blood biocompatibility with pyrolytic carbon heart valves, with good adherence of endothelial cells and minimal adherence and activation of platelets (Haubold, 1983). The dense and metastable form of amorphous carbon- diamond-like carbon is desirable for biomedical applications due its extreme hardness, low coefficient of friction, chemical inertness and good corrosion and wear resistance (Sheeja, Tay, Nung, 2004). The biocompatibility of diamond-like carbon was proven for orthopaedic and cardiovascular applications, also no inflammatory response from macrophage cells *in vitro* (Linder, Pinkowski and Aepfelbacher, 2002) and no cytotoxic effects on fibroblasts or osteoblast cells have been observed. Among the graphene derivatives, graphene oxide has been widely explored for *in vitro* and *in vivo* drug delivery and imaging, (Pan, Sahoo and Li, 2012; Hong et al., 2012) and its good biocompatibility was supported by some studies: (Yang et al., 2012; Sasidharan et al., 2012). Current carbon-based biomaterials demonstrate excellent biocompatibility and it is hoped that the unique properties of graphene/graphene oxide can be safely and effectively exploited in biomedicine.

Although the biocompatibility of GO is inconclusive (Snitka, 2015), the different experimental conditions and GO characteristics, such as GO size, dose, exposure methods and surface properties, may be the reasons for the incompatibility (Yang et al., 2012; Chang et al., 2011). Therefore, more studies are needed to understand the conditions of the safe use of graphene related nanoparticles.

2.2 Carbon-based materials

Carbon is the fourth most abundant element in the universe and is the *Materia prima* for all life (Neto et al., 2009; Suess and Urey, 1956). This gives carbon a central role in organic chemistry as well as being an important element in inorganic and organic chemistry, materials science and biomedicine. The carbon atom, with its six electrons, is tetravalent, having four of the electrons available for chemical bonding. Because of the flexibility of its bonding, carbon has several different allotropes with a large variety of physical properties. The main forms of elemental carbon are diamond and graphite. Under ambient conditions graphite is the stable phase, while under the application of high pressure and high temperature a transformation to the diamond structure occurs (Dresselhaus, Eklund, 1996; Hagg et al., 1988; Steinbeck et al. 1985) (see Fig. 2.1.).
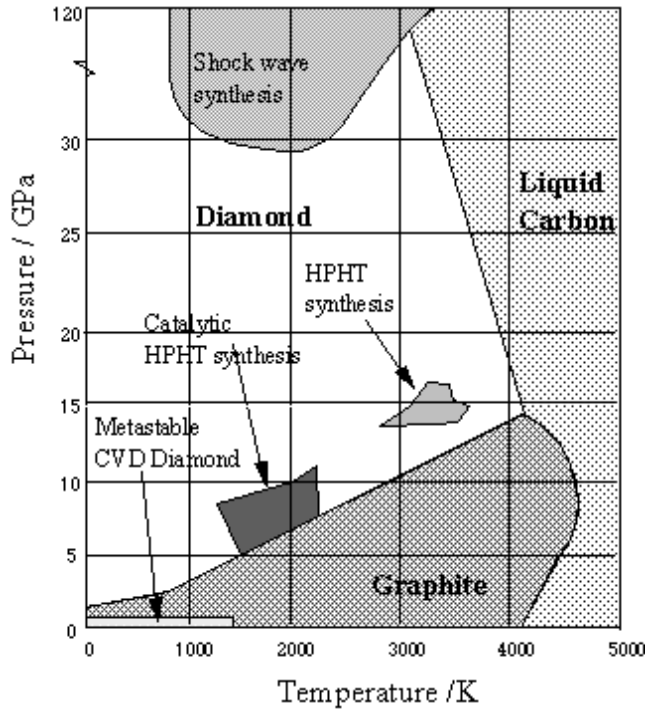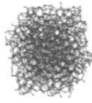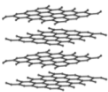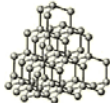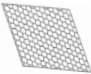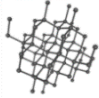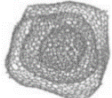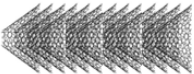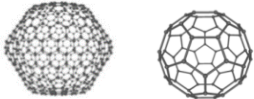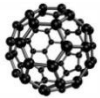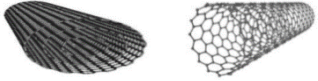
Fig. 2.1. The phase diagram for diamond and graphite (Bundy, 1979)

Moreover, graphite is a soft material due to its layered structure, while diamond is one of the hardest materials observed. The properties of carbon vary depending on the degree of crystallinity as well as ratio between sp^2 and sp^3 carbon atoms in the material. Recently, research on nanoscale objects and nanostructured materials has been expanded. Nanomaterials of carbon, and especially graphitic nanomaterials, have cause huge interest in the last decade because of the discovery of several new nanoscale graphitic materials with unique properties (Iljima et al., 1991; Novoselov et al., 2004; Sano et al., 2001).

Different types of carbon nanomaterials, including fullerenes, graphene and carbon nanotubes, have many technological advantages such as easy modification by functional groups, high carrier capacity, incorporating both hydrophilic and hydrophobic substances, and high chemical stability, and the possibility of being used for many applications is becoming more popular. A wide variety of carbon-based materials are available, such as nanoparticles, nanodiamonds, fullerenes, nanotubes, etc. (Table 2.1), which have been used in analytical applications (Săndulescu et al., 2015). The sp^2-bonded carbon atoms configuration is responsible for the development of strong van der Waals forces that significantly prevent the solubility and dispersion of carbon-based nanoparticles. To avoid these problems, different methods have been proposed (Zhao, Chen and Xie, 2006; Wooten and Gorksi, 2010; Bose, Khare and Moldenaers, 2010), such as the addition of polar groups (oxygen, hydroxyl, phenyl, etc.). The stability, mechanical and electrical properties could also be affected by the surface defects of carbon nanostructures (Soetedjo, Mora and Garcia, 2010; Masheter et al., 2007).

18

Table 2.1. Carbon-based materials

The main forms of carbon:		
Amorphous carbon	Graphite	Diamond
The carbon nanomaterials:		
Graphene	Nanodiamonds	Nano-onions
Nano-peapods	Nanofibres	Nanorings
Fullerenes C540 | C60	Fullerites	Carbon nanotubes MWCNT | SWCNT

2.2.1 Graphene

The stacks of graphene, the basic building blocks of graphite, are held together by weak van der Waal forces. Graphene is a material that proposes great prospects for the future of engineering and analytical chemistry, consisting of one-atom-thick sheets that provide a specific surface area (of 2,630 m^2/g). Graphene based architectures were initially foreseen as an abnormal case keeping in mind their different nature in respect of biomolecules or cellular substructures. Graphene has a high mechanical strength, elasticity and high thermal conductivity (Pumera et al., 2010; Geim and Novoselov 2007; Neto et al., 2009), but also, like other carbon-based materials, presents a disadvantage: its poor dispersion in aqueous medium. Indeed, the stable dispersions of graphene sheets have been achieved using alkylamines and hydrophilic carboxyl groups, amphiphilic polymers or other dispersing agents (Bustos-Ramirez et al., 2013). Also, graphene can be used as an active element in many applications either pristine and/or functionalised by a wide range of molecules (Huang et al., 2011; Bai, Li and Shi, 2011). The functionalisation of graphene is important to controllably coordinate its properties using both covalent

and non-covalent approaches (Georgakilas et al., 2012; Sreeprasad and Berry, 2013; Huang et al. 2012). The functionalisation of graphene is one of the ways for improving its dispersion. Therefore, graphene oxide, a graphite derivative with hydroxyl, epoxy and carboxyl groups covalently attached to its layers, shows a better dispersibility in some solvents than graphene.

There is a wide variety of methods for graphene fabrication. The first method, published in 2004 (Novoselov et al., 2004), is the mechanical exfoliation of small patches of highly ordered pyrolytic graphite. Afterwards, other fabrication methods have been developed: unzipping MWCNT to form graphene ribbons (Bai and Huang, 2010); substrate-independent methods using micro-moulding inside a capillary (He et al., 2010) and spray deposition of graphene oxide-hydrazine dispersions (Pham et al., 2010).

The possible industrial applications of graphene are very wide. It is known that graphene could be used in bendable LCD screens, bendable watches and smartphones, and sensors in textile; graphene could replace carbon black to strengthen rubbers and tyres; graphene reinforcement in polymers and polymer composites to optimise the mechanical properties (stiffness, strength) and thermal conductivity, etc.

2.2.2 Graphene functionalisation

Since 2004 a major focus of experimental research has been concentrated on the development of new synthetic routes (see Fig. 2.2, the rate of growth in the number of studies carried out on graphene functionalisation in the world) enabling an effective production and functionalisation of well-defined graphene sheets.
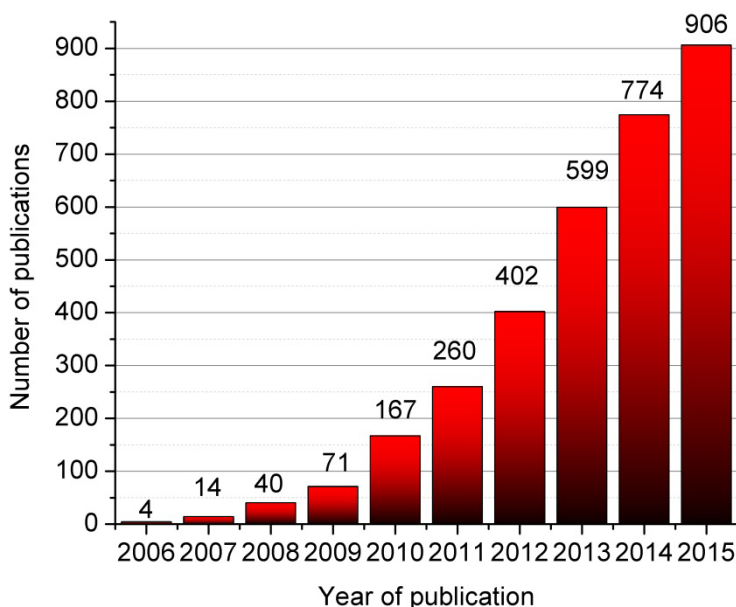
Fig. 2.2. Annual number of graphene functionalisation-related publications. Statistics obtained according to the Web of Science data

Graphene sheets can be chemically modified using either the covalent or non-covalent method.

A covalent bond is a region of relatively high electron density between nuclei which arises at least partly from the sharing of electrons and gives rise to an attractive force and characteristic internuclear distance. For many molecules, the sharing of electrons allows each atom to attain the equivalent of a full outer shell, corresponding to a stable electronic configuration. Covalent bonding includes many kinds of interactions, including σ-bonding, π-bonding, metal-to-metal bonding, agostic interactions, bent bonds and three-centre two-electron bonds (Huang et al., 2012; Smith and March, 2007; Miessler and Tarr, 2004).

A non-covalent interaction differs from a covalent bond in that it does not involve the sharing of electrons, but rather involves more dispersed variations of electromagnetic interactions between molecules or within a molecule (Anslyn, Dougherty, 2006). The chemical energy released in the formation of non-covalent interactions is typically on the order of 1-5 kcal/mol (1,000–5,000 calories per 6.02x 10^{23} molecules) (Lodish et al., 2000). Non-covalent interactions can be generally classified into four categories, electrostatic, π-effects, *van der Waals* forces and hydrophobic effects (Table 2.2. Chemical bonds).

Table 2.2. Chemical bonds and interactions

Intramolecular ("strong")	Covalent bond	By symmetry	Sigma (σ); Pi (π); Delta (δ); Phi (φ)
		By multiplicity	1 (single); 2 (double); 3 (triple); 4 (quadruple); 5 (quintuple); 6 (sextuple)
		Miscellaneous	Agostic bond; Bent bond; Dipolar bond; Pi backbond; Charge-shift bond; Hapticity; Conjugation; Hyperconjugation; Antibonding.
		Resonant bonding	Electron-deficient (3c–2e 4c–2e); Hyper-Coordination (3c–4e); Aromaticity.
	Metallic bonding		Metal aromaticity
	Ionic bonding		Polar covalent bonds
Intermolecular ("weak")	*Van der Waals* forces		Force between two permanent dipoles (Keesom force) Force between a permanent dipole and a corresponding induced dipole (Debye force) Force between two instantaneously induced dipoles (London dispersion force). Dispersion forces.

Intermolecular ("weak")	Hydrophobic effects	The segregation and apparent repulsion between water and nonpolar substances
	Hydrogen bond	Low-barrier; Resonance-assisted Symmetric; Dihydrogen bonds C–H···O interaction
	Electrostatic	Stationary or slow-moving electric charges with no acceleration
	π-effects	Metal-π Interactions (cation-π or neutral interactions); Polar-π interactions; Aromatic-aromatic interactions (π stacking); π donor-acceptor interactions; Anion-π interactions; Cation-π interactions; C-H-π interactions.

Graphene or graphene oxide covalently attached usually occurs through oxygen linkages (oxygenated functional groups) (Liu, et al., 2008) or through structural π-π networks, non-covalently by π-π stacking (Table 2.3) (Lonkar, Deshmukh and Abdala, 2015; Zhang et al., 2010).

Table 2.3. Graphene functionalisation

Covalent modification of graphene		
Covalent Attachment of Organic Functionalities to Pristine Graphene		
Free radical addition to the sp^2 carbon atoms of graphene	Covalent modification of graphene oxide (GO)	Functionalisation of partially reduced graphene
Covalent modification of graphene using dienophiles	a) Amidation	
	b) Esterification	
	c) Silanisation	
	d) Other GO functionalisation's	
Non-covalent modification of graphene		
Polynuclear aromatic rings	Surfactants and ionic liquids	Biomolecules and macromolecules	Attachment of nanoparticles

Graphene/graphene oxide functionalisation with porphyrins chosen due to a very promising approach because of a fusion of unique properties of both counterparts can generate advanced nanocomposites for broad applications in nanomedicine and biotechnology. Depending on the chosen porphyrins the graphene/graphene oxide can be functionalised by using different types of modifications: covalent (amidation, esterification, radical addition to the sp^2 carbon atoms and other functionalisation) and non-covalent (through *Van der Waals* forces, electrostatic, π interactions, hydrophobic effect, etc.) (Georgakilas, 2012).

Subsequently, whereas it was revealed that graphene oxide nanoparticles have a higher toxicity for cancer cells than healthy ones, the GO functionalisation with doxorubicin, the drug used in cancer chemotherapy, was performed. The combination of GO and DOX may help reduce the concentration and the side-effects of each and increases the effectiveness of anticancer drug.

2.2.3 Graphene oxide

Graphene oxide is a two-dimensional carbon layer with oxygen-containing functional groups (epoxy, hydroxyl and carboxyl) on the basal plane and at the edges (Fig. 2.3). Those characteristics let graphene oxide change the shape, size and relative fraction of the sp^2-hybridised domains and make it a very promising material for the biomedical system (Shen et al., 2012; Zhang et al., 2011; Zhang, Zhang and Xu, 2012).
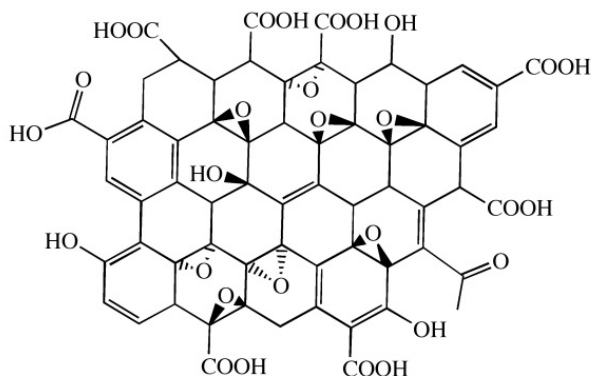
Fig. 2.3. Structure of graphene oxide molecule (Hamilton, 2009)

One of the most popular methods to obtain graphene oxide is Hummers' method (Offeman and Hummers, 1958). Briefly, the graphite powder is affected with a mixture of H_3PO_4 and concentrated H_2SO_4 acids, and then $KMnO_4$ (Fig. 2.4). After completing the oxidation of graphite, the reaction mixture is quenched by H_2O_2. The colour of the mixture changes from dark brown to bright yellow, indicating the formation of GO.
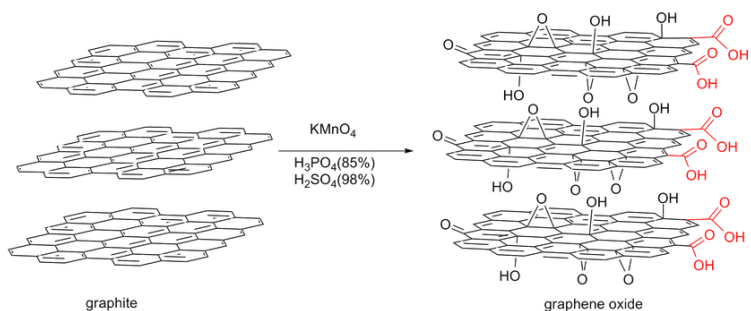
Fig. 2.4. The synthesis of GO by Hummers' method (Zuo et al., 2013)

Other methods include the oxidation of graphene; various Hummers' method modifications, for example, excluding the $NaNO_3$, increasing the amount of $KMnO_4$ and performing the reaction in a 9:1 mixture of H_2SO_4/H_3PO_4 (this method provides a greater amount of hydrophilic oxidised graphene) (Marcano et al., 2010), the synthesis of GO by sonication-assisted oxidation of graphite in a solution of potassium permanganate and concentrated sulfuric acid followed by reduction with ascorbic acid (Abdolhosseinzadeh, Asgharzadeh and Kim, 2015); using a Tang-Lau synthesis method in which the sole source is glucose, this process is safer, simpler and more environmentally friendly. Another important advantage of the Tang-Lau method is the control of thickness, ranging from monolayer to multilayers by adjusting the growth parameters (Tang et al. 2012).

The possible applications of GO are also very wide; laboratory reagent, catalyst, carrier, biological drug, filter medium, adsorbent, gas-barrier material, preservative, electrostatic shielding film, polymeric composite, transparent electrode material (Fig. 2.5).
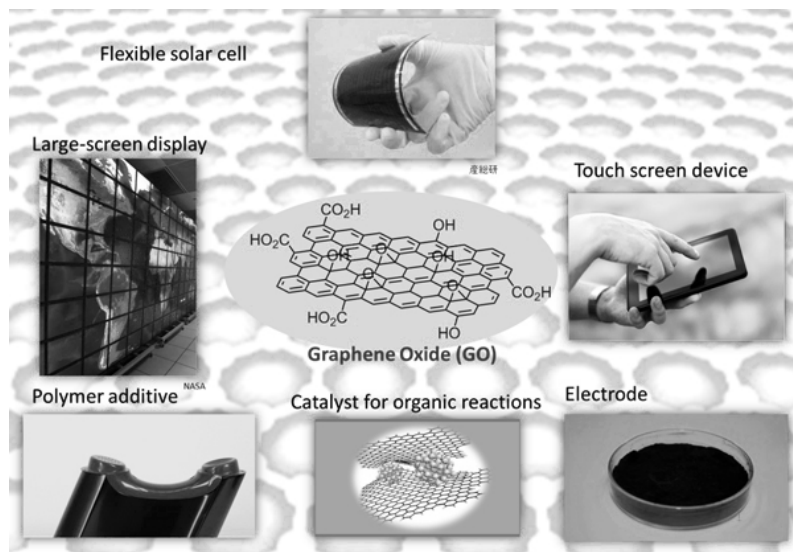
Fig. 2.5. Promising applications of graphene oxide (Yuta, 2013)

2.2.4 Biomedical applications of graphene/graphene oxide

Beyond the wide possible applications of graphene in fields such as nanoelectronics (Xuan et al., 2008), composite materials (Yang et al., 2010; Fan et al., 2010; Bai et al., 2010; Sun, Wu, 2011; Fang et al., 2010), energy technology (Liu et al. 2010; Stoller et al., 2008; Wang et al. 2009), sensors (Lu et al. 2009) and catalysis (Qu et al., 2010), the biomedical application of graphene is a relative new area with significant potential. The first study on graphene for biomedical applications was the report on the use of graphene oxide as an efficient nanocarrier for drug delivery by Liu et al. in 2008 (Liu et al., 2008). Since then, a lot of interesting work has been carried out to explore the use of graphene and his derivatives for widespread biomedical applications, such as (Shen et al., 2012):

- drug delivery,

- gene delivery,

- biological sensing,

- biological imaging,

- GO-based antibacterial materials,

- GO-based biocompatible scaffold for cell culture.

It was found that graphene and especially its oxidised modification, graphene oxide, can be highly optimised for their specific functions *in vivo* and possess features that are often desired in drug delivery carriers (Allen and Cullis, 2004). The first step to use graphene oxide as a drug delivery carrier is a functionalisation of GO with a functional molecule, particle, etc. In particular, GO was effectively functionalised with anticancer drugs like doxorubicin (Zhang, 2010; Yang et al., 2008; Yang et al., 2011; Zhang et al., 2013). Porphyrins, as well, were successfully linked with GO via both p–p stacking and covalent bonding between amino and carboxyl groups (Ye et al., 2012; Liu et al., 2009). In particular, for a drug delivery system GO branched by polyethylene glycol represents a set of features like good solubility and stability in physiological solutions, also the unique ability of the graphene structure to attach and deliver aromatic, water insoluble drugs (Yang, Xu, 2013).

The most important examples of GO surface modifications are with precursors such as polyethylene glycol, folic acid, chitosan, polyethyleneimine, polyacrylic acid, amphiphilic copolymers, sulfonic acid and amino group, dextran, gelatine, nanoparticles, etc. (Feng, Liu, 2011). There is a rising interest for the GO-polymers drug carrier systems for transferring a water-insoluble anticancer drug like doxorubicin. Wenjun Miao and others reported the safety, tumour accumulation and potential of polyethylene glycol-grafted graphene oxide (pGO) as a multimodal nanocarrier of photosensitisers and synergistic anticancer agents such as Doxorubicin (Miao et al., 2013). Liang Yan and colleagues used a polyethyleneimine-modified graphene oxide as a nanocarrier of an aromatic drug; the active formulation did not exhibit toxicity on the human endothelial cells and

showed a high potency of killing cancer cells *in vitro* (Yan et al., 2013). In another study, a GO-based multifunctional hybrid functionalised by magnetic/fluorescent SiO_2 microsphere via an amidation process has been developed for the loading and delivery of drugs. This application of the developed GO-based magnetic fluorescent hybrids for HepG2 cells demonstrated a good therapeutic effect (Gao et al., 2013).

While drug delivery also involves membranes, attention should be paid to nanoparticle interactions with the membrane. The goal of an ideal drug delivery system is to deliver a drug to a specific site, in a specific time and release pattern. Also, there are many other requirements such drug permeability, good release properties, etc. (Simo, Cifuentes and Gallardo, 2003; Stamatialis et al. 2008). It was found that the lipid monolayer functionalised graphene nanomaterials exhibited excellent performance as a carrier for loading the anticancer drug, doxorubicin, with a high loading capacity of 70% and the loaded drug can be released under pH control (Liu et al., 2015). However, the interaction of GO nanoparticles with membranes is still inconclusive. In experimental conditions the membrane characteristics cause diverse uptake pathways of nanoparticles into cells, the cell response, etc. Therefore, more studies to understand the mechanism and possible response of different types of membranes/cells are needed.

2.2.5 Graphene oxide functionalisation with porphyrins

Porphyrins are heterocyclic macrocycles composed of four modified pyrrole subunits interconnected at their *α*-carbon atoms via methine bridges (=CH−). Porphyrin macrocycles are highly conjugated planar systems, and, correspondingly, demonstrate a high-level of both light absorption and emission, which can be efficiently modulated by peripheral substitutes. Many porphyrins are naturally occurring; one of the best-known porphyrins is heme (iron-containing porphyrin), a cofactor of the protein haemoglobin. Heme-containing proteins (haemoproteins) are found extensively in nature. Myoglobin and haemoglobin are two O_2-binding proteins that contain iron porphyrins.

Porphyrins are the conjugate acids of ligands that bind metals to form complexes. The metal ion usually has a charge of 2^+ or 3^+. A porphyrin without a metal-ion in its cavity is a free base (Fig. 2.6).

A schematic equation for these syntheses is shown:

H_2 porphyrin + $[ML_n]^{2+}$ → M (porphyrinate) L_{n-4} + 4 L + 2 H^+ (2.1)

where: M = metal ion, L = a ligand
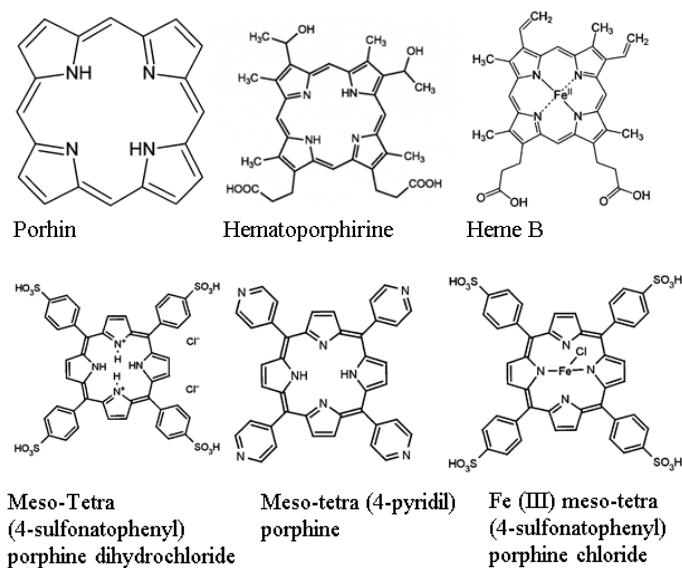
Fig. 2.6. The structure of porphyrins (Ikawa, 2008)

In non-photosynthetic eukaryotes, the committed step for porphyrin biosynthesis is the formation of δ-aminolevulinic acid by the reaction of the amino acid glycine with succinyl-CoA from the citric acid cycle. In plants, it is produced from glutamic acid via glutamyl-tRNA and glutamate-1-semialdehyde (also known as C5 or the Beale pathway).

One of the most common laboratory syntheses for porphyrins is based on work by Rothemund (Rothemund, 1935; Rothemund, 1936). This synthesis is a condensation and oxidation starting with an aldehyde and pyrrole (Fig. 2.7).
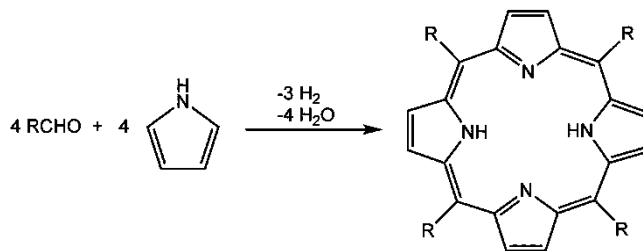
Fig. 2.7. The porphyrin synthesis by Rothemund method (Rothemund, 1935)

Other techniques described by Adler et al. (1967) and Falvo et al. (1999) are more modern and are used commonly in university teaching labs. The disadvantage of these methods, that in solution-phase synthesis, acidic conditions are essential. Indeed, there are also green chemistry variants (no additional acids are required) performed with microwave irradiation using reactants adsorbed on acidic silica gel (Pettit et al. 1992) or at a high temperature in the gas phase (Drain et al., 1997).

It was precisely those optical properties of porphyrins that stimulated the use of porphyrin as photosensitisers (PHS) in Photo Dynamic Therapy (PDT) and Fluorescence Diagnosis (FD) (Dong et al., 2010). Both PDT and FD are based on

the administration of photosensitisers that preferentially accumulate in cancerous tissues, followed by exposure of the tumour area to visible light of the proper wavelength, and results in an energised form which, upon decay, results in cytotoxicity. Excited photosensitiser molecules are then deactivated through two main processes: emission of fluorescence from the lowest excited singlet state of the photosensitiser (principle of FD) or generation of reactive oxygen species via the lowest triplet state of the photosensitiser (principle of PDT). Many PHS used clinically in PDT such as Photofrin®, Visudine® and Foscan® are based on the porphyrin structure (Banfi et al., 2012).

However, porphyrins are usually unstable during light exposure and their photo-degradation is mediated by singlet oxygen (Inhoffen et al., 1969; Krieg and Whitten, 1984; Moan and Kessel, 1988; Rotomskis, Streckyte and Bagdonas, 1997). Recent studies show that the use of nanocarriers significantly improve the photo-physical properties of porphyrins in respect of their free form in aqueous solutions, porphyrin based PHS encapsulated in various nanocarriers (liposomes, micelles, nanoparticles) demonstrate stronger absorption, and a high-level of singlet oxygen generation without damage from PHS, etc. (Xie et al., 2014). However, up to now the available information on the effect of GO on the optical properties of porphyrins is quite limited, in particular on ones of natural origin like hematoporphyrin (HP), an endogenous porphyrin formed by the acid hydrolysis of haemoglobin (Luzgina et al., 1977) that has been used as an antidepressant and antipsychotic as well as in phototherapy of cancer since the 1920s (Strecker, Palmer and Braceland, 1934; Rassmussen-Taxdal and Ward, 1955; Dolmans, Fukumura and Jain, 2003). At the same time, HP~GO aggregate can also be used in new drugs for PDT/FD if HP~GO based formulations demonstrate high luminescence intensity and increased protection against singlet oxygen damage. The present study is directly within this concept.

The optical properties of hematoporphyrin strongly depend on its aggregation state, position of the bands, their intensity and luminescence efficiency, and singlet oxygen production rate drastically decreased under the aggregation of HP (Kotkowiak, Łukasiewicz and Dudkowiak, 2013). The main approach to increase the efficiency of HP as a PDP/FD specific drug is to prevent the formation of aggregates using i) oligomerisation, (ii) changing the equilibrium to the monomeric forms (encapsulation) or (iii) by inducing formation of monomer friendly organised architectures. The first approach i) was successfully realised by S. Schwartz in 1960 for the detection of tumours by treating hematoporphyrin with concentrated sulfuric acid (Schwartz, Absolon and Vermund, 1955; Lipson, Baldes and Olsen, 1961). The more effective bioactive products of this reaction are porphyrin oligomers containing 2 to 8 pyrrole rings connected by ester bonds. The possibility of the oligomerisation process is the result of the structural features of hematoporphyrin. Indeed, HP is an iron-free derivative of heme with 4 methyl groups, 2 hydroxyethyl groups (secondary alcohols) and 2 propionic acid (carboxylic) groups attached to the pyrrole rings. As dihydroxy and dicarboxylic acid, derivative HP can be involved in the Fischer/Fischer–Speier esterification reaction in the presence of an acid catalyst.

Sulphuric acid in this case is a catalyst in esterification reactions, which has been well known for many years (Marchetti, Errazu, 2008; Deng et al., 2001).

The actual challenge is to extend the use of the "oligomerisation approach" in new hematoporphyrin through its combination with nanostructured carriers. In line with that, the main focus of the activity within this area is on developing a less-costly and more efficient approach to enhance the photodynamic efficiency of HP through the self-assembling of GO and hematoporphyrin in functional architectures.

2.2.6 Graphene oxide functionalisation with doxorubicin

Doxorubicin (also known as Adriamycin) is a drug used in cancer chemotherapy. Doxorubicin is a glycoside antibiotic, it consists of the tetracyclic quinoid aglycone adriamycinone (14-hydroxydaunomycinone) linked to the amino-sugar daunosamine (Fig. 2.8).
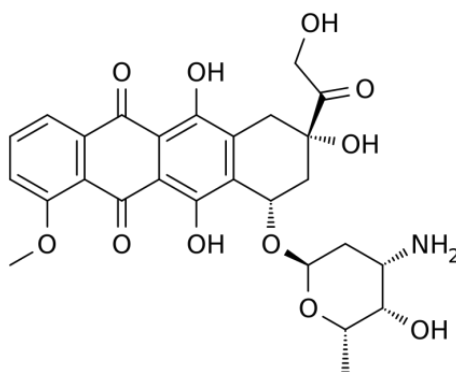
Fig. 2.8. Structure of doxorubicin (Tacar, Sriamornsak and Dass, 2013)

It is derived by aerobic fermentation from a bacterial species, *Streptomyces peucetius* var. *caesius,* or by chemical synthesis from Daunomycin. It is an anthracycline antitumor medicine and works by intercalating DNA and inhibition of macromolecular biosynthesis (Tacar, Riamornsak and Dass, 2013). It is commonly used in the treatment of a wide range of cancers and is often used in combination chemotherapy as a component of various chemotherapy treatments.

The adverse effects of doxorubicin include hair loss, suppression of the body's bone marrow to produce new blood cells, nausea and vomiting, skin reactions and many others (Rossi, 2013). Although the most dangerous side-effect of doxorubicin is cardiomyopathy, leading to congestive heart failure. The rate of cardiomyopathy is dependent on its cumulative dose. The incidence of cardiomyopathy is about 4% when the dose of doxorubicin is 500-550 mg/m² and 36% when the dose exceeds 600 mg/m² (Chatterjee et al., 2010). Doxorubicin is available as the hydrochloride salt (Andriamycin), in liposome-encapsulated forms as Doxil (pegylated form), Myocet (nonpegylated form) and Caelyx, all these forms must be given by intravenous injection (Brayfield et al., 2014).

Recently, many studies of the combination of GO with doxorubicin have been performed due to the possible synergetic effect of these materials. It was reported

that Graphene oxide has an anticancer action and can be used as a pH-sensitive drug-carrier for other drugs (Cheng et al., 2015; Zhou, Zhou and Xing, 2014). Meanwhile, the adverse effects of doxorubicin could be reduced, because lower doses could be used. One of the main benefits of using a GO hybrid is the controlled release of loaded material (Balcioglu, Rana and Yigit, 2013; Ardeshirzadeh et al., 2015). In the near future these hybrids could serve as a promising platform for theranostics due to the anticancer drug loading capacity and the possibility to add a contrast agent.

2.3 Lipid membranes

All living cells are surrounded by a membrane that physically separates the interior components of the cell from its environment. It acts as a protective barrier that is selectively-permeable to ions and certain organic molecules, controlling the movement of substances in and out of the cell. Cell membranes consist of numerous biological molecules that are involved in a variety of cellular processes such as cell adhesion, ion conductivity and cell signalling. These molecules diffuse more or less freely in a high fluidity system, known as the liquid mosaic model (Singer and Nicolson, 1972).

The main structure of a cell membrane is made up of proteins that are partially embedded in a bilayer of phospholipids. Phospholipids are a type of lipid molecule. Lipids are organic compounds that consist of a 'tail' of long fatty acid hydrocarbon chains and a carboxyl 'head'. In the case of phospholipids, the 'head' contains a negatively-charged phosphate group making it highly polar and hydrophilic (Fig. 2.9). Conversely, the 'tail' is very hydrophobic. Therefore, when placed in water, phospholipids spontaneously arrange to point their 'tails' inwards towards each other and their 'heads' outwards towards the water, forming a membrane. In cellular membranes, this takes the shape of a bilayer; however, lipids can group together to form a variety of structures depending on their concentration, chemical structure and experimental conditions:

- Monolayer – a single layer film of lipids at an air-water interface formed by compression in a Langmuir-Blodgett trough;

- Micelle – a colloid of lipids in an aqueous suspension that is hydrophilic on the outside and hydrophobic on the inside;

- Bilayer – the natural, energetically-favoured form that lipids take in an aqueous environment;

- Liposome, or vesicle – the spherical form of a bilayer with an aqueous core.
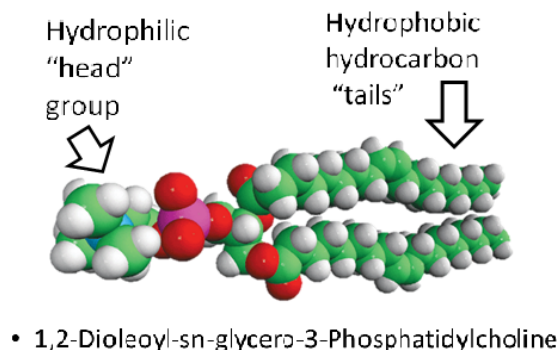
Fig. 2.9. Structure of phospholipid molecule (modified by Pogodin, Baulin, 2010)

Forces such as *van der Waals* and electrostatics, hydrogen bonds and non-covalent interactions contribute to the formation of a lipid bilayer. However, hydrophobic interactions are the major driving force in this process.

Depending on the absence or presence respectively of a carbon-carbon double bond within their 'tail', phospholipids can be saturated or unsaturated. The difference in saturation can cause variations in the thermodynamic properties of lipids that are otherwise structurally and chemically identical; unsaturated phospholipids tend to have a much lower phase transition temperature than saturated phospholipids. This is due to the disorder that arises from the presence of a carbon-carbon double bond in the molecule; the repulsion of electrons within the bond causes the hydrogen atoms to move outwards and produces a kink in the lipid 'tail'. The level of this disorder, and consequently the temperature at which an unsaturated phospholipid changes phase, depends on the number and position of these carbon-carbon double bonds (Koynova and Caffrey, 1998). This property is significant when saturated and unsaturated phospholipids are combined in a bilayer structure. The phospholipids, at a wide range of temperatures, are in different phases that separate out across the membrane and then cluster together to form regions known as microdomains. Microdomains are regions of tightly-packed saturated lipids in an ordered gel state that protrude from the fluidity of the loose unsaturated "kinked" lipids in a disordered liquid crystalline state. The regions vary in size and height depending on the type and concentration of the lipids and the ambient temperature of the membrane (Elliott et al., 2005).

2.3.1 Bilayer lipid membrane synthesis

There are two main lipid membrane synthesis methods:

- Lipid vesicle fusion
- Langmuir-Blodgett technique

By the lipid vesicle fusion method, thin lipid films are hydrated to form stacks of liquid crystalline bilayers that become fluid and swell. These bilayers detach

through agitation and self-close to form large, multilamellar vesicles that are reduced in size and fused to a solid support.

The Langmuir-Blodgett technique is a slightly less common way to produce lipid membranes. This method uses a rectangular Teflon bath equipped with moveable barriers that compress a monolayer of amphiphilic molecules on an air-water interface and transfer it onto a solid support (see Fig. 2.10).
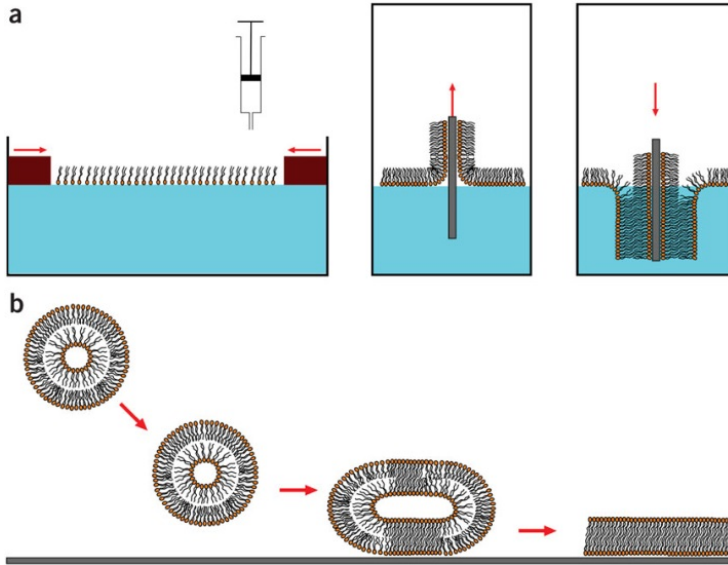
Fig. 2.10. Scheme of methods used for preparing BLMs for atomic force microscopy analysis: (a) Langmuir–Blodgett technique and (b) fusion of lipid vesicles (Mingeot-Leclercq et al. 2008)

Very important parameters for supporting the lipid membranes are the contact angle and wetting properties of the surface. Wettability studies usually involve the measurement of contact angles, which indicates the degree of wetting when a solid and liquid interact. Small contact angles correspond to high wettability, while large contact angles correspond to low wettability (Fig. 2.11). The equilibrium contact angle is given by Young's equation,

$$\gamma_{LV}\, Cos\,\theta_e = \gamma_{SV} - \gamma_{SL} \ (2.2)$$

where γ_{SL}, γ_{SV} and γ_{LV} are solid-liquid, solid-vapour and liquid-vapour interfacial tensions which measure the free energy (per unit area), θ_e is the equilibrium contact angle (Adamson, et al. 1997).
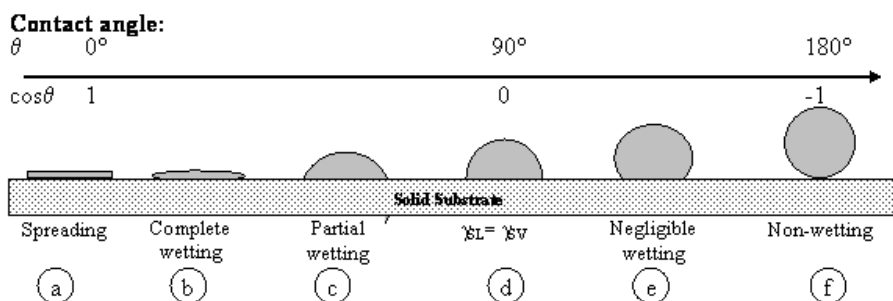
Fig. 2.11. Liquid drop on a solid surface. The condition $\theta < 90°$ indicates that the solid is wet by the liquid, and $\theta > 90°$ indicates non-wetting, with the limits $\theta = 0$ and $\theta = 180°$ defining complete wetting and complete non-wetting, respectively (Derrick et al., 2007)

The fusion of vesicles at a surface to form a supported bilayer can occur only on surfaces that are sufficiently hydrophilic, the static contact angle should be < 10 degrees. On the other hand, vesicles that settle on the surface tend to remain vesicular. When vesicles adsorb to strongly hydrophilic surfaces, they spread to maximise contact with the surface while causing increasing surface tension on the vesicle wall, and eventually rupture to form the supported bilayer. The other way is to form lipid monolayers by using ligands, mostly alkanethiols, which can be easily tailored (e.g., using different terminal groups and chain lengths) to change the hydrophobicity. Using hydrophobic self-assembled monolayers (SAM), due to the interaction between the hydrophobic chains with the modified substrate, a lipid monolayer can be formed (Fig. 2.12).
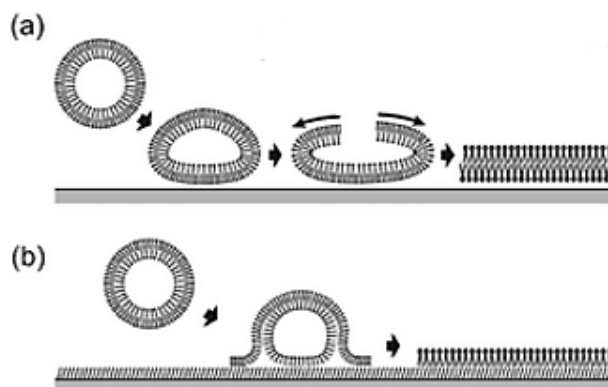
Fig. 2.12. Bilayer membrane formation on: a) hydrophilic surfaces. b) alkyl-SAM terminated surfaces (Tero, Watanebe and Urisu, 2006)

2.3.2 The analysis methods of lipid membranes

The bilayer lipid membranes (LM) are increasingly accepted as experimental models commonly employed for both fundamental and applied studies (Sweetenham, 2010; Vemula and Fedorova, 2015). The most common methods used to characterise LMs are fluorescence-based techniques, such as confocal

microscopy, fluorescence correlation spectroscopy (FCS), Förster resonance energy transfer (FRET), total internal reflection fluorescence (TIRF) or two-photon microscopy (Sezgin, and Schwille, 2011). However, some of these methods require labelling, they also provide limited data about the structure of LMs. Vibrational spectroscopies, such as infrared (IR) or Raman are eligible analytical tools for the investigations of LMs because of their ability to provide information about the structure of the LM as well as its chemical composition (Baeten, 2010; Lewis and McElhaney, 2013). Indeed, IR analysis of the samples prepared in aqueous medium is complicated due to the strong and temperature dependent absorption of water, while Raman spectroscopy allows this problem to be avoided. This aspect is important with regard to biological samples, including lipid membranes, requiring the maintaining of native conditions. However, the analysis of lipid membranes by Raman spectroscopy is complicated due to its low sensitivity and spatial resolution (Sweetenham and Notingher, 2010). This problem can be facilitated by the usage of Surface enhanced Raman scattering (SERS) spectroscopy enabling the enhancement of the Raman signal of lipid membranes. In recent years, a number of reports have been published showing the successful application of SERS for the investigation of lipid-protein interactions (Petersen and Nielsen, 2009; Suga et al., 2015; Kühler, Weber and Lohmüller, 2014; Kundu, Levin and Halas, 2009; Ren et al., 2011; Li et al., 2014). It has been shown that in cases when gold nanoparticles (NP) are used, the formation of LM is complicated. The modification of SERS substrates should be done because Au NPs are hydrophilic and immiscible in organic solvents or lipid systems (McClements, 2014), and the contact angles of the surface are often inappropriate to form the lipid membrane. In order, to create a lipid monolayer around Au NPs, they must be modified with ligands, mostly alkanethiols, to increase the hydrophobicity and the dispersibility of Au NP within the lipid phases. The other way is to use thiol-modified lipids for the formation of bilayer LM on gold nanoparticles (Castellana, Gamez and Russell, 2011) or to modify gold nanoparticle surfaces with halide ions (Kah et al., 2012; Orendorff et al., 2009).

It is known that the ability to form a bilayer on the surface can be explained by differences in the hydrophilicity of the two substrates (Cha, Guo and Zhu, 2006). The fusion of vesicles at a surface to form a supported bilayer can occur only on surfaces that are sufficiently hydrophilic. On the other hand, vesicles that settle on the surface tend to remain vesicular. When vesicles adsorb to strongly hydrophilic surfaces, they spread to maximise contact with the surface while causing increasing surface tension on the vesicle wall, and eventually rupture to form the supported bilayer. The ability of adsorbed vesicles to spread on a surface can be estimated by the static contact angle made by a droplet of water on the surface, it should be < 10 degrees. The other way is to form lipid monolayers by using ligands, mostly alkanethiols, which can be easily tailored (e.g., using different terminal groups and chain lengths) to increase the hydrophobicity. Using a hydrophobic SAM, due to the interaction between the hydrophobic chains with the modified substrate, a monolayer is obtained (Marques, De Almeida and Viana, 2014).

2.3.3 Lipid membrane interaction with nanoparticles

Lipid membranes are essential components of any living cell and lipid membranes are simplified planar models of cell membranes, commonly employed for fundamental and applied studies. LM as a model system are of great importance for improving our understanding of cell interaction with the environment, various disease mechanism and membrane properties for drug screening purposes. An important area of nanomedicine research is the interaction of nanoparticles with cell and possible toxicity (Heikkila et al., 2014; He et al., 2015; Karlsson et al., 2013; Adjei, Sharma and Labhasetwar, 2014; Lu et al., 2014). Apart from LMs mechanical function as a cell wall, the lipid membrane performs the function of a transfer mechanism for molecules diffusing through the membrane. As this process could distort the membrane structure, characterisation tools are needed that enable us to study the structure and ordering of the membrane. The influence of NPs on the membrane materials are known to be more environmentally and biologically friendly than inorganic materials and it is one of the most common elements in our ecosystem. Especially, graphite is a naturally occurring material and it can be expected that graphene, a single layer of graphite, will be safe and useful for biological purposes. Carbon nanotubes and graphene oxide have attracted attention as promising carbon nanomaterials in different applications (Chabot et al., 2014; Hakimi and Alimard, 2012; Dreyer, Todd and Bielawski, 2014). In biomedical applications and nanomedicine, GO have been utilised over existing drug delivery vectors due to their ability to cross cell membranes easily and their high surface area, which provides multiple attachment sites for drug targeting (Chung, Won and Zelenay, 2013; Krishna et al., 2013).

2.3.3.1 Lipid membrane interaction with graphene/graphene oxide

Cell interaction with graphene microsheets can either undergo a near-orthogonal cutting or a parallel attachment mode with cell membranes. Recently, the theoretical analysis to characterise the deformed membrane microstructure and investigate how these two interaction modes are influenced by the splay, tilt, compression, tension, bending and adhesion energies of the membrane was performed by Yi and Gao (2015). This analysis indicates that, driven by the membrane splay and tension energies, a two-dimensional microsheet such as graphene would adopt a near-perpendicular configuration in the transmembrane penetration mode; the membrane bending and tension energies would lead to parallel attachment in the absence of cross membrane penetration (Fig. 2.13).
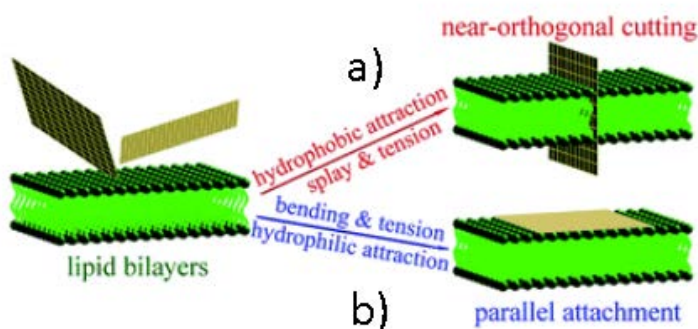
Fig. 2.13. Modes of interaction between cell membranes and graphene microsheets: a) Near-perpendicular penetration of graphene microsheets into the membrane b) Parallel attachment and spreading of graphene microsheets onto the membrane (Yi and Gao, 2015)

These interaction modes may have broad bio-medical implications in applications. The membrane penetration by 2D nanomaterials, such as a graphene oxide (GO); reduced graphene oxide (rGO) and other related material microsheet, whose surfaces are hydrophobic or can exhibit other specific adhesive interactions with the lipid tails. In this case, the length scale of the concerned local membrane deformation is comparable with the bilayer thickness and the elastic energy of a monolayer. The elastic energy principally results from the deformation of the hydrocarbon chains (Lipowsky and Sachmann, 1995). Another important mode of the interaction is the parallel attachment of micro-sized 2D nanomaterials on cell membranes. For the transmembrane-penetration mode, the membrane thickness and scales of local membrane deformation are comparable, and the penetration is driven by the (hydrophobic) attraction between lipid tails (interior of the bilayer) and nanomaterial surface. Conversely, the parallel attachment mode is mostly facilitated by the hydrophilic or highly specific attraction between the bilayer surface and nanomaterial surface. Consequently, the cell membrane can be simply modelled as a smooth and structureless surface with consideration of the bending and tension energies.

It was noticed that bending and membrane tension energies serve as the main driving force for the parallel configuration of transmembrane (membrane attaching) 2D nanomaterials. On the other hand, the orientation of one-dimensional nanomaterials wrapped by a cell membrane is tension-dependent, the nanomaterials displaying a parallel configuration at a small (large) tension (Yi, Shi and Gao, 2014). The orientations of inserted molecules in a lipid bilayer and one-dimensional transmembrane nanomaterials have implied a near-perpendicular transmembrane configuration.

The interactions between graphene nanosheets and cell membrane show different effects. The pristine graphene can readily penetrate into the bilayer and has no effect on the integrity of membrane (Fig. 2.14).
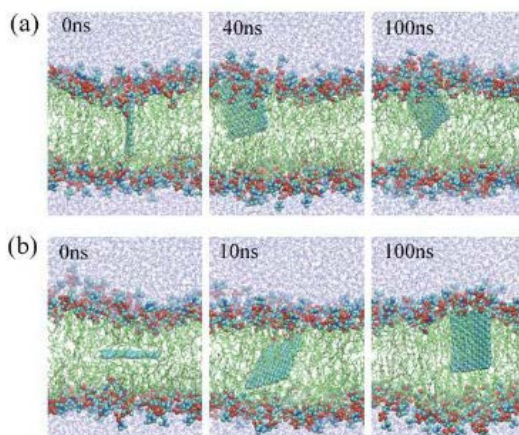
Fig. 2.14. The trajectories of pristine graphene located vertically a) or lay flat b) in the centre of the membrane with snapshots at each tilt angle (Modified by Chen et al., 2016)

Pristine graphene can easily penetrate into the membrane and could only remain vertical with slight fluctuations. The fast insertion of pristine graphene into the lipid bilayer is driven by the hydrophobic and strong dispersion interactions between graphene and lipids. The interaction of bigger graphene sheets with the bilayer can slightly deform the membrane without any significant damage.

On the other hand, when GO is embedded in the membrane, several lipids are pulled out of the membrane to the surface of the GO, resulting in the pore formation, and water molecules flowing into the membrane. The difference between pristine graphene and graphene oxide in the membrane originates from GO's oxygen-contained groups, which enhance the adsorption of the lipids on the GO surface. Indeed, the main interactions between GO and the membrane are determined by the strong dispersion interactions between its hydrophobic domains and the lipid tails of the bilayer (Chen et al., 2016).
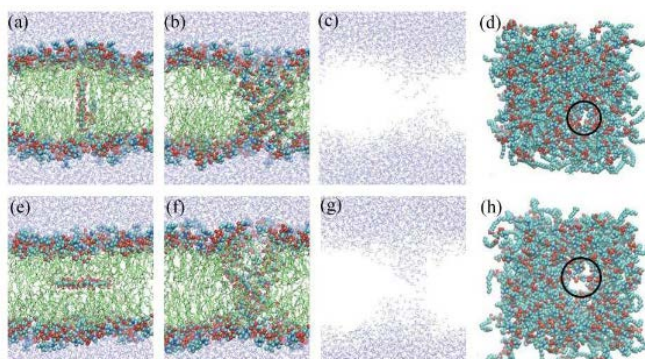
Fig. 2.15. The trajectories of graphene oxide when: a)-d) GO lay flat initially at the membrane centre; e)-h) GO was positioned vertically at the membrane centre. b), f) are the final configurations of simulations. c), g) are the side views of water distributions. d), h) are the top views of bilayers, where black circles specify the water pores. (Modified by Chen et al., 2016)

Different from the graphene fast insertion, GO remain at the interface between the head groups and water. The difficulty for GO to enter the membrane is due to the fact that oxygen contained groups render GO much more hydrophilic (Chen et al., 2016). Though, GO can still enter the membrane by cell's endocytosis due to its nanosize.

2.4   Impact of nanoparticles on cells viability

Human lungs, skin and the gastro-intestinal tract are in constant contact with the environment. These three ways are the most likely points of entry for nanoparticles. Injections and implants are possible routes of exposure to engineered nanomaterials. Nanoparticles, due their small size, can translocate from these entry portals into the circulatory and lymphatic systems, body tissues and organs. Some nanoparticles can produce irreversible damage to cells by oxidative stress and organelle injury. It is important to understand why and how nanoparticles are able to enter cells and interact with various cells and their components like nucleus, mitochondria, etc. (Buzea, Pacheco and Robbie, 2007). Nanoparticle toxicity depends on chemical composition, shape, particle ageing, uniformity, size and agglomeration state (see Fig. 2.16). It was shown that the surface charge and aggregation state of nanomaterials critically influence their *in vitro* cytotoxicity. The surface charge of nanoparticles plays an especially important role in cell-nanoparticle interactions because cell membranes themselves are charged. It is also very important to understand that nanoparticles can be toxic, non-toxic, or even appear to have beneficial health effects. Examples of positive effects are that nanoparticles could be used as antioxidants, fullerene derivatives (Bosi et al., 2003), and nanoparticles made of compounds holding oxygen vacancies (Cerium oxide and Yttrium oxide) (Schubert et al., 2006) have demonstrated neuroprotective properties and antiapoptotic activity, and as anti-microbial agents several types of nanoparticle (silver (Prabhu and Poulose, 2012), titanium dioxide (Jesline et al., 2015), fullerenes (Tegos et al., 2005), zinc oxide (Tayel et al., 2011) and magnesium oxide (Tang and Lv, 2014) have an antimicrobial effect.
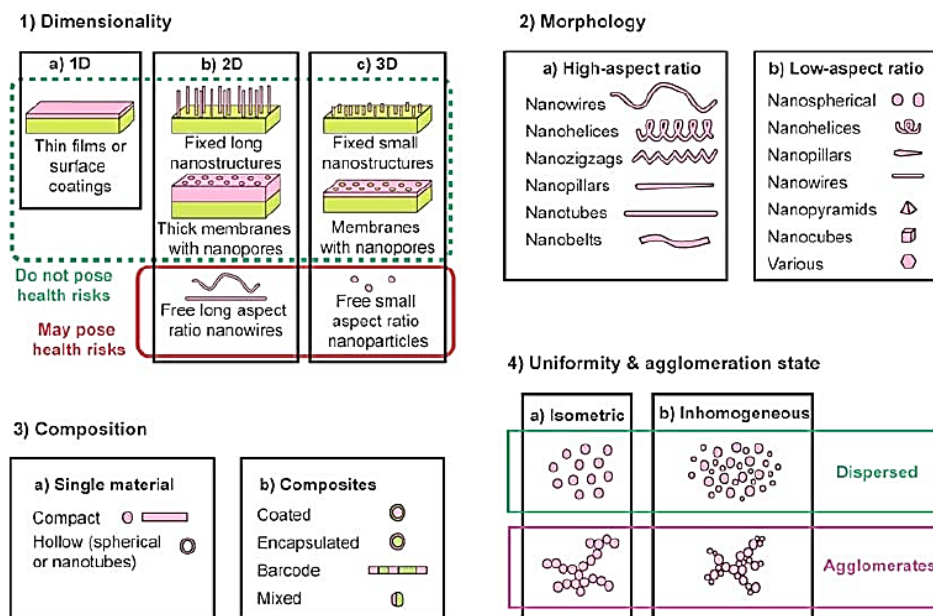
Fig. 2.16. Classification of nanomaterials from the point of view of nanostructure dimensions, morphology, composition, uniformity and agglomeration state (Buzea et al., 2007)

2.4.1 Nanoparticle and protein corona

The surface of nanomaterials is covered by protein corona upon their entrance to the biological medium. The biological medium modifies the surface of nanomaterials, and therefore further cellular responses depend on the composition of the corona. The corona variations could be according to the physicochemical properties of the nanomaterials (e.g., size, shape, surface charge, surface functional groups, and hydrophilicity/hydrophobicity). The protein corona gives a new biological identity which is what is seen by cells. The biological identity determines the physiological response including agglomeration, cellular uptake, circulation lifetime, signalling, kinetics, transport, accumulation and toxicity (Rahman et al., 2013).

There are two types of protein corona: "hard" and "soft". Proteins that adsorb with a high affinity form are known as "hard" corona, consisting of tightly bound proteins that do not readily desorb. Proteins that adsorb with low affinity form the "soft" corona, consisting of loosely bound proteins.

Blood plasma contains around 1,000 different proteins with 12 order of magnitude differences in the concentration of these proteins (Monopoli et al., 2011) and lipids. Therefore, upon injection of nanoparticles into the blood, there is a competition between different biological molecules to adsorb on the surface of the nanoparticles (Fig. 2.17). In the initial stage, the most abundant proteins are

adsorbed on the surface; however, over time they will be replaced by higher affinity proteins (Vroman's effect) (Vroman et al., 1980).

The thickness of protein corona can vary due to many parameters such as protein particle size, concentration and surface properties of particles. Most plasma proteins present a diameter of 3–15 nm. A model for the protein corona has been proposed by Simberg et al (Simberg et al., 2009); it consists of "primary binders" that recognise the nanomaterial surface directly and "secondary binders" that associate with the primary binders via protein-protein interactions. Such a multi-layered structure is significant for the physiological response as the secondary binders may alter the activity of the primary binders or "mask" them, preventing their interaction with the surrounding environment.
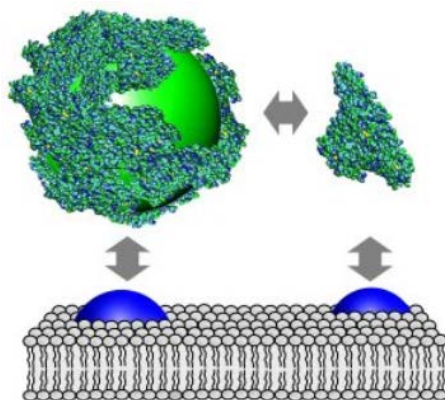
Fig. 2.17. The scheme of protein corona formation. Proteins (blue-green) enclose a nanoparticle (green) that can bind to the cell membrane, e.g. to receptors (blue), like the free protein. (Rocker et al., 2009)

The protein corona potentially transforms the biological identity of the particle and adds an additional level of complexity for the bio–nano responses. In the last year, studies have investigated the impact of the protein corona on nanoparticles such as amorphous silica nanoparticles (Docter et al., 2014; Lesniak et al., 2012), graphene oxide, iron-platinum and cadmiun selenide/zinc sulphide nanoparticles (Rocker et al., 2009), iron (Jansch et al., 2012), gold (Dobrovolskaia et al., 2009), silver (Shannahan et al., 2014), bare cadmium sulphide nanoparticles (Lynch, Dawson, 2008), polystyrene and carboxyl-modified polystyrene particles (Lundqvist et al., 2008). In general, the protein corona significantly affects cell vitality; automated high-throughput microscopy revealed that cell death was almost completely prevented upon treatment in the presence of serum or human plasma proteins.

Recent studies have shown that protein BSA coating can mitigate the cytotoxicity of graphene oxide by reducing its cell membrane penetration. Protein corona decreases cellular uptake of GO. The adsorbed BSA weakened the interaction between the phospholipids and graphene surface due to a reduction of the available surface area significantly reducing the lipid bilayer damage (Duan et al., 2015, Fig. 2.18).
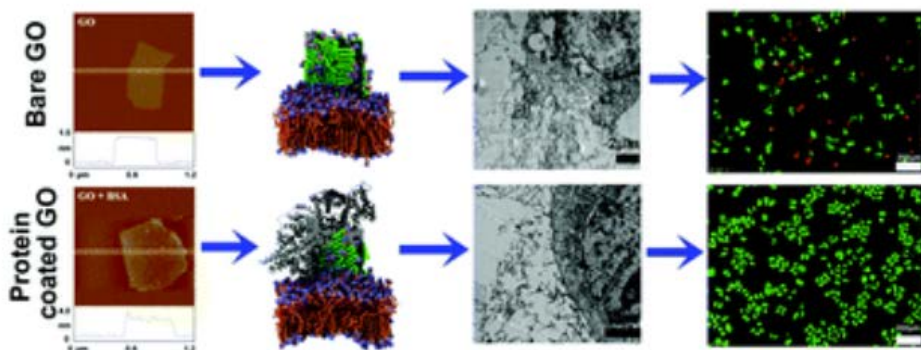
Fig. 2.18. The scheme of how the protein corona formed in serum medium affects GO nanoparticles biological response (Duan et al., 2015)

2.4.2 Impact of graphene on cells viability

The most widely used nanomaterials are silver, carbon-based nanomaterials, silicon/silica, gold, zinc, titanium and iron. Carbon-based nanomaterials included, but are not limited to carbon nanotubes, fullerenes and graphene. In the last few years a lot of research studies were performed to determine the potential short and long-term toxicity of this new nanomaterial - graphene. A number of groups have devoted time and effort to explore the *in vitro* cytotoxic effects of graphene. It was reported that graphene prepared by the chemical vapour deposition technique increased the activation of caspase 3 (apoptosis marker), release of lactate dehydrogenase and generation of reactive oxygen species (ROS), in neural pheochromocytoma-derived PC12 cells (Zhang et al., 2010). Also, it was demonstrated that GO would induce significant cytotoxicity of human fibroblast cells at a GO concentration above 50 mg/l (Wang et al., 2011). Other scientific group uncovered that as-prepared GO only slightly decreased A549 cells proliferation rates without inducing apoptosis or cell death at an exposure concentration up to 85 mg/l. By contrast, reduced GO (rGO) after treatment by hydrazine hydrate exhibited a remarkable cytotoxicity to the same cell line (Hu et al., 2010). Though, GO after the biocompatible coating (for example, PEGylation) exhibited negligible *in vitro* toxicity to many cell lines (Raji, HCT-116, U87MG, MDA-MB-435, OVCAR-3, MCF-7) even at high concentrations up to 100 mg/l (Liu et al., 2008; Sun et al., 2008).

The impact of carbon nanotubes and graphene on immune cells is still at a very early stage of investigation (Oreccioni et al., 2014). The authors suggest that GO does not enter the A549 cell and has no obvious cytotoxicity (Chang et al., 2011). Indeed, GO can cause a dose-dependent oxidative stress in the cell and induce a slight loss of cell viability at high concentration. These effects are dose and size related, and should be considered in the development of bio-applications of GO. In conclusion, GO is a relatively safe material at a cellular level, which is confirmed by the favourable cell growth on GO film. The *in vivo* bio-distribution of graphene is also highly dependent on its surface chemistry. Also, how the size of nano and

different types of cell lines affects the *in vivo* behaviour of graphene requires further investigation. A lot more systematic exploration is demanded in order to fully understand the *in vivo* long-term fate and toxicology of graphene at different doses in various animal models before any clinical application of this novel nanomaterial (Feng, Liu, 2011).

3 MATERIALS AND RESEARCH METHODOLOGY

3.1 Materials

All reagents used in the experiments were chemically or analytically pure commercial reagents (see Table 3.1).

Table 3.1. List of reagents used

Reagent	Manufacturer	Formula
Graphene oxide. Highly concentrated graphene oxide dispersion in water; 500 mg/l.	Graphene Supermarket, USA	$C_xO_yH_z$
The high-quality CVD graphene films with coverage of about 95% of Si/SiO$_2$ substrates	Graphene Laboratories Inc., USA	C_x
Meso-tetra (4-sulfonatophenyl) porphine dihydrochloride (TPPS$_4$) Mass: 1007.92; purity: >95%	Frontier Scientific Inc., USA	$C_{44}H_{32}N_4O_{12}S_4Cl_2$
Fe(III) meso-tetra (4-sulfonatophenyl) porphine chloride (FeTPPS$_4$) Mass: 1024.27; purity: >95%	Frontier Scientific Inc., USA	$C_{44}H_{28}FeN_4O_{12}S_4Cl$
Hematoporphyrin IX dihydrochloride (HP). Mass: 671.61; purity: >95%	Frontier Scientific Inc.	$C_{34}H_{40}Cl_2N_4O_6$
Meso-tetra (4-pyridyl) porphine (TPyP) Mass: 618.70; purity: >97%	Frontier Scientific Inc., USA	$C_{40}H_{26}N_8$
Doxorubicin hydrochloride (DOX), 98.0-102.0%	Sigma Aldrich, Germany	$C_{27}H_{29}NO_{11} \cdot HCl$
Hydrochloric acid, 36.5-38.0%	Sigma Aldrich, Germany	HCl
Sodium hydroxide, ≥97.0%	Sigma Aldrich, Germany	$NaOH$
Deionised water. Refractive index- n20/D 1.34(lit.); conductivity- ≤4.3 µS/cm; density- 1.000 g/ml at 3.98°C.	Sigma Aldrich, Germany	H_2O
Sulfuric acid, 95-98%	Carl Roth, Germany	H_2SO_4
Phosphate buffered saline (PBS), powder, pH 7.4	Sigma Aldrich, Germany	9.0% NaCl; pH 6.8±0.1 (25°C)

Reagent	Manufacturer	Formula
Tris(hydroxymethyl)aminomethane (Tris), ≥99.8%	Sigma Aldrich, Germany	$NH_2C(CH_2OH)_3$
Ethylenediaminetetraacetic acid (EDTA), ≥98.0%	Sigma Aldrich, Germany	$(HO_2CCH_2)_2NCH_2$ $CH_2N(CH_2CO_2H)_2$
Sodium chloride, ≥99.0%	Sigma Aldrich, Germany	$NaCl$
Calcium chloride, ≥99.9%	Sigma Aldrich, Germany	$CaCl_2$
Calcium carbonate, ≥99.0%	Sigma Aldrich, Germany	$CaCO_3$
Sodium azide, ≥99.5%	Sigma Aldrich, Germany	NaN_3
2-propanol, 99.5%	Sigma Aldrich, Germany	$(CH_3)_2CHOH$
1,2-dioleoyl-*sn*-glycero-3-phospho-L-serine (DOPS), ~95%	Sigma Aldrich, Germany	$C_9H_{11}NO_5$
1,2-dioleoyl-*sn*-glycero-3-phosphocholine (DOPC), ≥99%	Sigma Aldrich, Germany	$C_{44}H_{84}NO_8P$
1,2-dioleoyl-*sn*-glycero-3-phosphoethanolamine (DOPE), ATTO 647 labelled DOPE	ATTO-TECH, USA	$C_{41}H_{78}NO_8P$
Hydrofluoric acid, 48%	Sigma Aldrich, Germany	HF
Ethanol, 96%	Sigma Aldrich, Germany	C_2H_5OH
Silver nitrate, ≥99.0%	Sigma Aldrich, Germany	$AgNO_3$
Hydrogen tetrachloroaurate (III), ≥99.9%	Sigma Aldrich, Germany	$HAuCl_4 \cdot 3H_2O$
Zinc oxide nanopowder, ~20 nm	Nanogate AG, Germany	ZnO
Titanium dioxide nanopowder, ~35 nm	NaBond, China	TiO_2
Dulbecco`s modified Eagle medium (DMEM). Contain 1000 mg/l of glucose, L-glutamine, phenol red, sodium pyruvate and sodium	Sigma Aldrich, Germany	

Reagent	Manufacturer	Formula
bicarbonate, powder, suitable for cell culture		
Foetal bovine serum (FBS), sterile-filtered, haemoglobin, ≤20 mg/dl, impurities ≤10 EU/ml endotoxin, suitable for cell culture	Sigma-Aldrich, Germany	
L-glutamine solution, sterile-filtered, concentration 200 mM, suitable for cell culture	Sigma-Aldrich, Germany	$H_2NCOCH_2CH_2CH(NH_2)CO_2H$
Penicillin-streptomycin, solution stabilised, with 10,000 units penicillin and 10 mg streptomycin/ml, sterile-filtered, suitable for cell culture	Sigma-Aldrich, Germany	
Trypsin-EDTA solution, 0.25%, sterile-filtered, suitable for cell culture, 2.5 g porcine trypsin and 0.2 g EDTA • 4Na per litre of Hanks' Balanced Salt Solution with phenol red	Sigma-Aldrich, Germany	
Albumin from bovine serum (BSA), lyophilised powder, suitable for cell culture, ≥96% (agarose gel electrophoresis)	Sigma Aldrich, Germany	
Gram's crystal violet solution, contains 2.3% certified crystal violet, 0.1% ammonium oxalate and 20% ethyl alcohol	Fluka Chemie, Switzerland	

The experiments with cells were carried out *in vitro* with Chinese hamster ovary (CHO) and mouse hepatoma MH-22A (MH-22A) cell lines.

The preparation and estimation of CHO and MH-22A cell viability were performed at Vytautas Magnus University (Kaunas). The experiments with SAF and FCS spectroscopies were performed at the University of Zurich (Switzerland). All the other experiments were performed at Kaunas University of Technology (Kaunas).

3.2 Methods

3.2.1 Preparation of graphene oxide

The graphene oxide (GO) dispersion was prepared by diluting dispersion, with a concentration of 500 mg/l with deionised water. Before using it for the

experiments, the GO dispersion was sonicated for 1 hour in an ultrasonication bath (Branson 2510, USA). For the Raman scattering and AFM measurements a drop of dispersion was dropped onto glass or another substrate and it was left to dry for 1 h.

3.2.2 The functionalisation of graphene with meso-tetra (4-sulfonatophenyl) porphyrins

Coverage of the purchased high-quality CVD graphene film on Si/SiO2 substrates was 95%. The thickness of the SiO_2 layer was 285 nm. The metal-free and Fe (III) meso-tetra (4-sulfonatophenyl) porphyrin solutions (TPPS$_4$ and FeTPPS$_4$, respectively) (10^{-5} M concentration) were prepared by dissolving in deionised water of TPPS$_4$ and FeTPPS$_4$ porphine chloride powders. The reversible protonation/deprotonation process of metal-free TPPS$_4$ is performed by adding HCl or NaOH into the stock solution and controlled by both pH measurements (pH-150 M, Gomel Plant of Measuring Devices) and direct UV-Vis characterisation. Before the adsorption of porphyrins on graphene, the solutions were filtered through 200-nm pore membrane filters, then precipitated onto the substrates by the drop-and-dry method (5 µl per a droplet) and rinsed for 5 min with deionised water.

3.2.3 The functionalisation of graphene oxide with hematoporphyrin

The GO stock dispersion was prepared by diluting 510 µl GO (500 mg/l) in 500 µl deionized water. For the preparation of acidic solutions, a few µl of concentrated sulfuric acid (SA) were added to the stock dispersion of GO to reach a final pH value of c.a. 2.0. The hematoporphyrin solution was prepared by diluting 500 µl HP (10^{-5} M concentration) in 500 µl deionized water. For acidic solutions of HP, conc. sulfuric acid was added to reach the pH value of the final solution of c.a. 2.6. The reversible esterification reaction is performed by adding SA or NaOH into the solution and controlled by pH measurements at room temperature and direct UV-Vis characterisation. For the Raman scattering and FT-IR measurements a drop of dispersion was placed on the glass substrate; in the case of Raman scattering it was left to dry for 1 h.

3.2.3.1 Measurements concept and data processing algorithms

Initial measurements were focused on the properties and aggregation state of single HP and GO itself under sulfuric acid treatment. Then, the interaction between hematoporphyrin and graphene oxide was measured at neutral pH. Finally, hematoporphyrin, graphene oxide and sulfuric acid interactions were investigated. In the last case, the reversibility of the reaction between hematoporphyrin and graphene oxide was controlled by UV-Vis measurements using H_2SO_4 and NaOH water solutions for pH changing.

Measurements for different GO-HP ratios were performed in line with the following procedure: 1:10 diluted initial solutions of HP (10^{-5} M) were mixed with the same volume, but different concentrations of GO (500 mg/l) water solutions - 1:2, 1:5, 1:10, 1:12.75, 1:20 (by volume). Fluorescence measurements were undertaken using a USB2000 fibre optic spectrometer, excited by blue laser (473

nm). The same measurements were also repeated for samples with the addition of 1 µl of conc. H_2SO_4 (pH 2). The total emission was calculated in the following way:

$$I^*(t) = \sum_{\lambda=600\,nm}^{\lambda=700\,nm} I(t) \ (3.1)$$

where I (t) is the intensity of average and background corrected luminescence response.

The HP/GO ratio γ (surface/surface) within aggregates was estimated using the following procedure. The total surface area occupied by the HP molecules and GO flakes are designated as S_{HP} and S_{GO}, respectively. Hence, the HP/GO ratio γ might be described by the following expression:

$$\gamma = \frac{S_{HP}}{S_{GO}} \ (3.2)$$

S_{HP} and S_{GO} are the total surface areas occupied by the HP molecules and GO flakes, respectively. S_{GO} might be easily estimated using a value of graphene oxide specific surface area δ specified by the producer (c.a. 833 m^2/g) contrary to the same value of graphene in 2,630 m^2/g (Zhu et al., 2010). If xGO (gram) is the total mass of GO in solution, the surface area covered with GO is expressed by the formula:

$$S_{GO} = \delta \cdot x_{GO} \ (3.3)$$

Considering that the polar surface area of HP s is c.a. 172 $\mathring{A}^2$ and x_{HP} (gram) is the total mass of hematoporphyrin in solution, the total surface occupied by the HP molecules in solution could be expressed as:

$$S_{HP} = \frac{x_{HP}}{(mw_{HP}/N_A)} \cdot s \ (3.4)$$

where mw_{HP} (gram) = 598.69 g and $N_A = 6.0221 \bullet 10^{23}$ are the molecular weight of HP and Avogadro number respectively. When S_{HP} and S_{GO} are expressed from (3.2) and (3.3) equation (3.4) becomes:

$$\gamma = \frac{S_{HP}}{S_{GO}} = \frac{x_{HP}}{x_{GO}} \cdot \frac{s \cdot N_A}{\delta \cdot mw_{HP}} \approx 2 \cdot \frac{x_{HP}}{x_{GO}} \ (3.5)$$

It is reasonable to stress that the value of γ (surface/surface) is slightly underestimated owing to the overestimation of s and underestimation of δ.

The analysis of concentration dependences was performed in the framework of the competition model using the Morgan-Mercer-Flodin equation or the logistic curve for data in the steady-state regime (Snopok, Boltovets and Rowell, 2006):

$$I^* \sim \frac{1}{1+(\frac{\gamma}{\gamma_0})^p} \ (3.6)$$

$\gamma \sim 1/x_{GO}$ and $\gamma_0 \sim 1/x_{HP}$, where X_{HP} is the initial amount of the competitor (HP) in the solution and xGO is proportional to the total value of adsorbed capacity of GO. Power p represents the order of the reaction in the competitor (HP), an effective value indicating the mechanism of the processes occurring in the system. To approximate the curves and linear dependence, the nonlinear regression analysis procedures of OriginPro 8.5 were used.

3.2.4 The functionalisation of graphene oxide with meso-tetra (4-pyridyl) porphine

Meso-tetra (4-pyridyl) porphine was dissolved in deionised water at room temperature under acidic aqueous medium (HCl was added to reach pH 2 at the concentration 5×10^{-4} M), obtaining a greenish colloid. Graphene oxide dispersion, with a concentration of 500 mg/l was diluted with deionised water. A suspension of aggregates was prepared by a simple π-π stacking approach. The pH was adjusted using HCl solution to reach 1.5 to 2.3 pH and 1% $CaCO_3$ to reach a pH from 5.4 to 9.1. In a typical experiment, GO was suspended in anionic meso-tetra (4-sulfonatophenyl) porphine dihydrochloride aqueous solution. Measurements of the absorption and fluorescence spectra were carried out after mixing 5×10^{-4} M porphyrin with different concentrations of graphene oxide at room temperature within 1 min. For the Raman scattering and AFM measurements a drop of solution was placed on the glass/gold substrate and left to dry for 1 h.

3.2.5 The functionalisation of graphene oxide with doxorubicin

Doxorubicin (DOX) was dissolved in deionised water to obtaining a concentration of 0.05 μg/ml. Sonicated graphene oxide dispersion (500 mg/l) was diluted with deionised water to obtaining a concentration of 6.25 μg/ml and mixed with doxorubicin.

For the experiments with an additionally heated mixture, the prepared suspension was placed in an ultrasonication bath for additional 1 hour with heating (~40ºC) to catalyse a covalent bonding between the GO carboxyl and DOX amino groups.

3.2.6 Substrate preparation

For the AFM, SEM and Raman measurements substrates were immersed in the Piranha solution for 24 h and after that rinsed a few times with deionised water.

As support for the lipid bilayers, glass coverslips were used. The pieces (ca. 2.5×4 cm) were cleaned in ethanol and sonicated for 15 min at 20°C in an ultrasonic bath and stored in ethanol. Before use, substrates were rinsed several times with deionised water, dried with nitrogen gas, affected with low pressure plasma (Electronic Diener) for 10 minutes and glued onto an aluminium sample cell.

3.2.7 Preparation of bilayer lipid membrane

Bilayer lipid membranes were prepared following a modified protocol of Richter et al (2003). The mixture of phospholipids: DOPS, DOPC and DOPE were solved in chloroform and mixed at a ratio of 35:65:0.000016. If DOPE were not used, the DOPS and DOPC ratio was 35:65. The lipid was dried overnight under vacuum to remove the solvent and then resuspended in *Tris* buffer (149 mM NaCl, 5 mM $CaCl_2$, 10 mM *Tris*) to a final concentration of 0.1 g/l. The resulting solution was extruded 27-29 times through a membrane (pore size 0.1 μm) to produce unilamellar vesicles. The vesicle solution was put directly in the measurement cell containing the glass substrate. The lipid solution was flooded with a peristaltic pump

for 10 min with a velocity of 0.250 ml/min, then the solution was left for 20 min so the vesicles could disperse on the surface, and after that it was replaced by the pure *Tris* buffer. Subsequently, this solution was exchanged again by a Ca^{2+} free *Tris* buffer (10 mM *Tris*, 133 mM NaCl) containing 5 mM EDTA in order to remove the Ca^{2+} ions and finally by PBS buffer. All buffers contained 0.05% NaN_3 and were adjusted to pH-7.4. After 3 h of rinsing with PBS, the bilayer was ready for measurements with other nanoparticles.

For the Raman measurements, bilayer lipid membranes were prepared in the following way: the mixture of phospholipids, DOPS and DOPC, were solved in chloroform and mixed at a ratio of 35:65. The lipids were dried with nitrogen gas and then resuspended in Tris buffer to a final concentration of 0.1 g/l. The resulting solution was extruded 27-29 times through a membrane (pore size 0.1 μm). The vesicle solution was put directly on the SERS substrate. The lipid solution was left for 30 min and after that it was replaced by the pure *Tris* buffer. Then, this solution was exchanged after 15 min again by a Ca^{2+} free *Tris* buffer containing 5 mM EDTA in order to remove the Ca^{2+} ions and finally, after another 15 min - by PBS buffer. After 1 h of rinsing with PBS, the bilayer lipid membranes were ready for Raman measurements.

For the analysis of the FCS data a diffusion model expanded by a second diffusion coefficient in a linear combination (D, D_a, D_b) was used.

$$G(\tau) = a * G_0 * \left(\frac{1 + 4 D_a}{\omega_0^2 \tau}\right)^{-1} + b * G_0 * \left(\frac{1 + 4 D_b}{\omega_0^2 \tau}\right)^{-1} \ (3.7)$$

with $\qquad D = a * D_a + b * D_b \ (3.8)$

where G_0 is the intercept of the FCS curve and inverse proportional to the number of the fluorescent molecules and ω_0 is the radius of the detection volume.

3.2.8 Preparation of ZnO and TiO$_2$ suspension

5 mg of ZnO/TiO$_2$ powder was sonicated for 15 min at 20°C in an ultrasonic bath along with 50 μl of 2-propanol. Next, 5 ml of PBS was added and the suspension (1 mg/ml) was sonicated for 1 h at 20°C. For the higher concentration suspension preparation (2.5 mg/ml) 12.5 mg of ZnO/TiO$_2$ powder was sonicated for 15 min at 20°C in an ultrasonic bath along with 125 μl of 2-propanol and 5 ml of PBS was added, and the suspension was sonicated for 1 h at 20°C. The ZnO or TiO$_2$ suspension was filtered with a 200 nm polyethersulfone pore membrane (Chromafil PES-20/25, Macherey-Nagel) and placed onto the glass substrate (Carl Roth, 50 x 24 mm) and then dried and measured.

3.2.9 The preparation of Ag and Au SERS substrates

The preparation of silver and gold SERS substrates was based on direct silver and gold ion reduction by elemental silicon. Silicon wafers were cut into small pieces (1.5 cm × 1.5 cm) cleaned by immersing them in pure ethanol and dried under nitrogen flow. Hydrofluoric acid was diluted with water to a final concentration of 24%.

Silver solution was prepared by diluting $AgNO_3$ with water to the final concentration of 2.0 mM. Silicon wafers were immersed in the prepared HF solution for 10 s, then immediately transferred to the $AgNO_3$ solution for 5 s, then immersed in water and finally dried under nitrogen flow.

Gold solution was prepared by diluting hydrogen tetrachloroaurate (III) with water to a final concentration of 2.5 mM. Silicon wafers were immersed in the prepared HF solution for 20 s, then immediately transferred to the hydrogen tetrachloroaurate (III) solution for 20 s, then immersed in water and finally dried under nitrogen flow.

3.2.9.1 The formation of 1-dodecanethiol binding layer on Au SERS substrate

The modification of the Au SERS substrate was performed as follows. 3 ml 1-dodecanethiol was diluted to 5 ml with ethanol. The prepared Au SERS were immersed in the solution for 2 hours. The proposed formation of the binding layer is shown in Fig. 3.1:
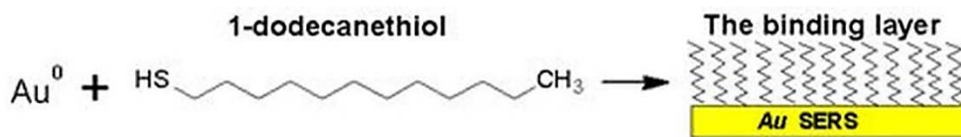
Fig. 3.1. The formation of binding layer on Au SERS substrate

3.2.10 Preparation of cell culture for experiments

The cells were cultured in 25 cm^2 tissue culture flasks in DMEM supplemented with 10% FBS, 1% L-glutamine, 90 µg/ml streptomycin and 100 U/ml penicillin (complete DMEM) in a humidified atmosphere of 95% air and 5% CO_2 at 37°C. When the cells reached confluence, they were detached from the bottom of the flask with 1.5 ml of 0.25% trypsin-0.02% EDTA solution. Then, the cell suspension was supplemented with 2.5 ml of complete DMEM, centrifuged for 2 min at 1,000 rpm (Biosan LMC-3000, Latvia) and resuspended in 1 ml of complete DMEM.

3.2.10.1 The preparation of sample and estimation of cell viability

The 10% BSA solution was prepared by diluting BSA in 0.9% NaCl. The influence of GO and GO-BSA on the viability of CHO and MH-22A cells was evaluated by a colony formation assay (Freshney, 2005). 40 mm diameter Petri dishes were filled with 2 ml of complete DMEM, which was afterwards supplemented with the corresponding investigating materials (one of the following: 10% BSA; 12.5, 25.0 or 50.0 µg/ml of GO; 12.5, 25.0 or 50.0 µg/ml of GO with 10% BSA). Also, control samples (without GO and GO-BSA treatment) of CHO and MH-22A cells with 0.9% NaCl solution were prepared. The Petri dishes were incubated for 30 min under the same conditions as described above. Approximately 300 cells per Petri dish were seeded. Then, the cells were incubated for 5 (CHO) or 8 (MH-22A) days for the formation of colonies. After incubation the cell colonies

were fixed using 70% ethanol. After fixation, the cells were stained with a Gram's crystal violet solution, air dried and counted through a binocular light microscope with 16x magnification. The viability of experimental groups was expressed as a percentage number of colonies compared to control (100%). Digital images of the colony examples were taken using a Moticam 2300 camera (Motic, Hong Kong) which was connected to the inverted ECLIPSE TS100 microscope (Nikon, Japan) with a magnification of 40x.

3.2.10.2 The preparation of cell samples for investigation by AFM and Raman spectroscopy and imaging

100 µl of the cells suspension (1×10^6 cells/ml) was seeded on the surface of a lithium niobate plate into each Petri dish filled with 2 ml of complete DMEM. The lithium niobate plates were selected because of good surface characteristics for cells growth and for the following analysis by Raman spectroscopy because of low background signal (Rodaite-Riseviciene et al., 2013). Then the cells were incubated for 24 h (CHO) or 48 h (MH-22A) to reach a confluent cell monolayer. Controls, without the treatment with GO, were performed in the case of both cell lines. GO dispersion was sonicated as described above. GO (12.5 µg/ml) was added into the Petri dishes with the cells for further incubation. After 24 h incubation the cells were washed with deionised water, fixed with 4% formaldehyde (in PBS) for 10 min at room temperature, washed again with deionised water and air dried.

3.3 Analytical techniques

In this thesis, a number of analytical techniques have been used with the aim to characterise the final products and to identify important experimental parameters. Raman spectroscopy has been used to obtain an understanding of the chemical composition, and atomic force microscopy giving the information about the morphology of the sample. Other methods applied in this work are UV-Vis, supercritical angle fluorescence and Fourier transform infrared spectroscopies, and scanning electron and light microscopies.

3.3.1 Raman spectroscopy

The Raman measurements were undertaken using the NTEGRA Spectra system (NT-MDT Inc.) in an upright configuration. The excitation wavelength was 532 nm (20-mW DPSS laser, LCM-S-111-20-NP25) with a controlling laser power in the range of 0.005–5 mW. To avoid extensive heating of the sample and beam damage, a different laser power was used for the analysis. The instrument was equipped with a $100 \times$ 0.7 NA objective, resulting in a diameter spot of 0.5 µm at the laser focus. The beam was focused on the sample, which rests on a controlled XYZ piezo stage capable of scanning samples over $130 \times 130 \times 7$ µm. The scattered light was collected by the same objective and directed through a 100-µm pinhole into a spectrometer (Solar TII, MS5004i). The signals were analysed with a TE-cooled (60°C) CCD ($1{,}024 \times 128$ pixels, DV401- BV, Andor Technology). The diffraction gratings of 600 lines/mm or 1,800 lines/mm were used, resulting in a spectral resolution of about 2.5 cm^{-1} or 0.8 cm^{-1}, respectively. Another CCD is used to collect

bright field images. A confocal Raman system was also used for measurements in a water environment.

The Raman measurements of cells were measured as follows: The search for GO in the cells was performed by the estimation of the characteristic Raman spectrum, the series of Raman spectra were recorded consistently along the Z axis across the cell, starting from outside of the cell. Over 260 spectra from 24 different cells were evaluated, and at least 11 spectra were acquired from each cell. The power of the laser at the sample was 5 mW for CHO and 0.5 mW for MH-22A, acquisition time - 5 s. To avoid overheating, a different power of laser irradiation at the cells was used. The distribution of GO inside the cells and cell fingerprint spectra were monitored by Raman imaging. Laser power was 5 mW at the cell surface, acquisition time - 1 s/pixel, image resolution - 92 x 92 pixels. Hyperspectral image collect over 8,000 spectra from each mapping picture. The GO distribution inside the cells was investigated by collected spectra evaluation and GO spectra map building on top of the confocal optical cell image.

3.3.2 Atomic force microscopy

Measurements were performed using NT-MDT Solver system (NT-MDT Inc.) in a semi-contact mode using commercial silicon cantilevers with a tip diameter of 10 nm and a force constant of 1.5 N/m. The AFM investigations for the ZnO and TiO_2 nanoparticles were done using commercial silicon cantilevers NSG11 with a force constant of 5 N/m.

The morphology of the supported lipid membranes was investigated by AFM imaging. Measurements were performed using the NT-MDT Solver system (NT-MDT Inc.) in a semi-contact mode in solution using commercial silicon cantilevers with a resonant frequency of 7-20 kHz and a spring constant of 0.08 N/m. Images were processed and analysed with NTEGRA Spectra software.

Cells morphology was investigated by AFM imaging and measurements of the cells membrane roughness. Measurements were performed for both cell lines using NT-MDT Solver system (NT-MDT Inc.) in a semi-contact mode using commercial silicon cantilevers with a tip diameter of 10 nm and force constant 1.5 N/m. Cell membrane roughness was measured on the topography images using SPIP™ software. The roughness average (SA) parameter was used for the comparison of the measured topographic results. Thirty surface areas of the cells (1000 × 1000 nm) were chosen at random from three independent experiments for CHO control cells, mouse hepatoma MH-22A control cells, CHO cells after the treatment with 12.5 µg/ml of GO and mouse hepatoma MH-22A cells after the treatment with 12.5 µg/ml of GO.

3.3.3 Supercritical angle fluorescence spectroscopy

SAF is a technique to detect and characterise fluorescent species (proteins, biomolecules, pharmaceuticals, etc.) and their behaviour very close or even adsorbed or linked to surfaces. The method is able to observe molecules at a distance of less than 100 nanometre from the surface even in the presence of high concentrations of fluorescent species. Using an aspheric lens for excitation of a sample with laser

light, fluorescence emitted by the specimen is collected above the critical angle of total internal reflection selectively and directed by parabolic optics onto a detector (Fig. 3.2). The method was invented in 1998 in the laboratories of Stefan Seeger at the University of Regensburg (Germany) and later at the University of Zurich (Switzerland) (Enderlein, Rukstuhl and Seeger, 1999). The principle on how SAF microscopy works is as follows. A fluorescent specimen does not emit fluorescence isotropically when it comes close to a surface, but approximately 70% of the fluorescence emitted is directed into the solid phase. Here, the main part enters the solid body above the critical angle. When the emitter is located just 200 nm above the surface, fluorescent light entering the solid body above the critical angle is decreased dramatically. Hence, SAF Microscopy is ideally suited to discriminating between molecules and particles at or close to surfaces and all other specimen present in the bulk (Ruckstuhl, Rankl and Seeger, 2003).
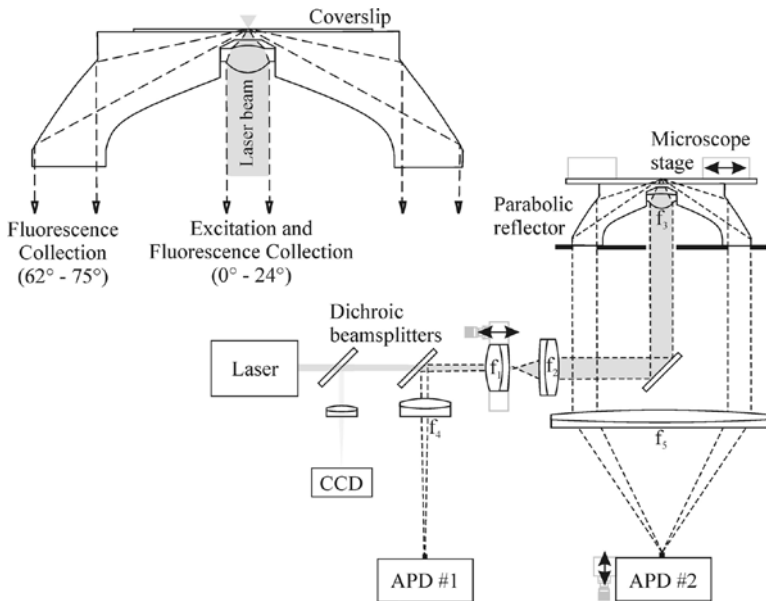
Fig. 3.2. Setup of SAF microscope (Ruckstuhl, Verdes, 2004)

Images of fluorescently labelled lipid membranes were recorded with a custom-made scanning microscope allowing the detection of fluorescence and the supercritical angle fluorescence images of an emitter simultaneously. The SAF channel detects only fluorophores in close proximity to the surface (~100-200 nm) and efficiently rejects the fluorescence from the bulk solution using parabolic lenses as the decisive optical element. All measurements were conducted by passing buffered solutions of NP's over the lipid membrane through the flow cell at a constant pump rate of 250 µl/min (0.42 mm/s) (Fig. 3.3). This flow rate is clearly slow enough to have no effect on the bilayer lipid membrane integrity. Raw scan images are presented as measured using an appropriate linear scaling for the signal intensities. Note that the background subtraction in all images is based on a fixed intensity threshold. The shown images are selected representative images from time-

lapse experiments which were conducted at varying time intervals because the applied setup (non-commercial) does not contain the option of a software controlled time-lapse measurement.

Fluorescence correlation spectroscopy (FCS) is a method that was introduced and established as a very suitable approach to characterise membranes (Bacia, 2004). FCS was employed by several authors to measure the lateral lipid mobility and to assess the impact of NP's on lipid dynamics in supported lipid membranes (Garcia-Saez, Carrer and Schwille, 2010; Garcia-Saez and Schwille, 2008).
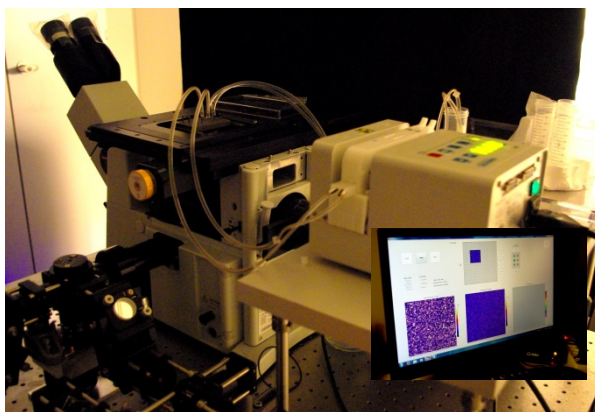
Fig. 3.3. Supported lipid bilayer formation on SAF microscopy

A hardware correlator translates the photon arrival pulses into intensity fluctuations and calculates the correlation real-time. The correlation curves were acquired and fitted to analytical expressions. For an averaged correlation measurement, a separate correlation measurement of 100 seconds duration was taken, and corresponding standard deviations for every point of the experimental curves were calculated from multiple experiments.

The diffusion coefficient of the lipids in the supported lipid bilayer was determined from the experimentally obtained correlation time and the known waist of the confocal observation volume.

3.3.4 UV-Vis spectroscopy and emission spectra measurements

The principle of ultraviolet-visible absorption is that molecules containing π-electrons or non-bonding electrons (n-electrons) can absorb the energy in the form of ultraviolet or visible light to excite these electrons to higher anti-bonding molecular orbitals (Mehta, 2011). The more easily excited the electrons (i.e. lower energy gap between the HOMO and the LUMO), the longer the wavelength of light it can absorb.

The absorption and emission spectra measurements were undertaken using a USB2000 fibre optic spectrometer (Ocean Optics). The fluorescence was excited by a 500 mW DPSSL laser (473 nm, LRS-476-TM-50-5, Laserglow Technologies).

3.3.5 Fourier transform infrared spectroscopy

Fourier transform infrared spectroscopy (FTIR) (Griffiths, James, 2007) is a technique, which is used to obtain an infrared spectrum of absorption or emission of a solid, liquid or gas. An FTIR spectrometer simultaneously collects high spectral resolution data over a wide spectral range.

The measurements of samples in a water environment with the FTIR spectra were performed by FTIR spectrometer Spectrum 100 (Perkin Elmer). The artefact level of this system is <0.005%T; a precision of ca 0.008 cm^{-1}. Spectral range 700-4,000 cm^{-1}.

3.3.6 Scanning electron microscope

A scanning electron microscope (SEM) produces images of a sample by scanning it with a focused beam of electrons. The electrons interact with atoms in the sample, producing various signals that contain information about the sample's surface topography and composition.

The morphology and composition of the aggregates were examined using a SEM/Focused Ion Beam (FIB) workstation Helios Nanolab 650 with an energy dispersive X-ray (EDX) spectrometer INCA Energy 350 X-Max 20.

3.3.7 Light microscopy

Digital images of the colony examples were taken using a Moticam 2300 camera (Motic, Hong Kong) which is connected to the inverted ECLIPSE TS100 microscope (Nikon, Japan) with 40x or 125x magnification.

3.4   Statistical analysis of experimental data

The processing of the experimental data was performed by Microsoft Excel 2010, OriginLab Corporation OriginPro 8.5, SPIP, NOVA 1.1.0.1840, MATLAB 7.12.0, GIMP2, CrystalSleuth and ImageJ.

The molecules were drawn using HyperChem 5.02 software and molecular mechanics optimisation was done by Newton- Raphson algorithm.

Statistical analysis was performed by Student's t-test. T-Test calculation for two independent means is used for comparing the averages of two separate groups. The null hypothesis (H$_0$: u$_1$ - u$_2$ = 0, where u$_1$ is the mean of first group and u$_2$ the mean of the second) tends to be that there is no difference between the means of the two populations; or, more formally, that the difference is zero (for example, that there is no difference between the average values of two groups). The calculations of statistics were performed using the following equation:

$$t = \frac{\overline{x}_1 - \overline{x}_2}{\int \left(\frac{(N_1 - 1)s_1^2 + (N_2 - 1)s_2^2}{N_1 + N_2 - 2} \right)\left(\frac{1}{N_1} + \frac{1}{N_2} \right)} (3.9)$$

Then the *p*-value, a function of the observed sample results (relative to a statistical model), which measures how extreme the observation is, was evaluated (*p<0.05, **p<0.01, ***p<0.005).

4 RESULTS AND DISCUSSION

4.1 The functionalisation of graphene/graphene oxide with organic molecules and characterisation

4.1.1 Characterisation of graphene oxide

The preparation of GO solution in neutral pH was carried out according to the procedure described in section 3.2.1. The UV-Vis measurements were performed in order to determine the formation of stable graphene dispersions. As shown in Fig. 4.1, the absorption peak of the GO dispersion at 230 nm and a weak shoulder at ~302 nm suggests that the electronic conjugation within the electronic conjugation level of graphene is chemically controllable, offering possibilities to tailor the properties of graphene sheets. Graphene sheets with different reduction levels can also form stable dispersions with other materials. In addition, GO is also expected to exhibit unique optical properties as evidenced by the recent demonstration of photoluminescence. This luminescence was found to occur from the near-UV-to-blue visible to near-infrared (IR) wavelength range (Loh et al., 2010). This property could be useful for biosensing, fluorescence tags and optoelectronics applications.
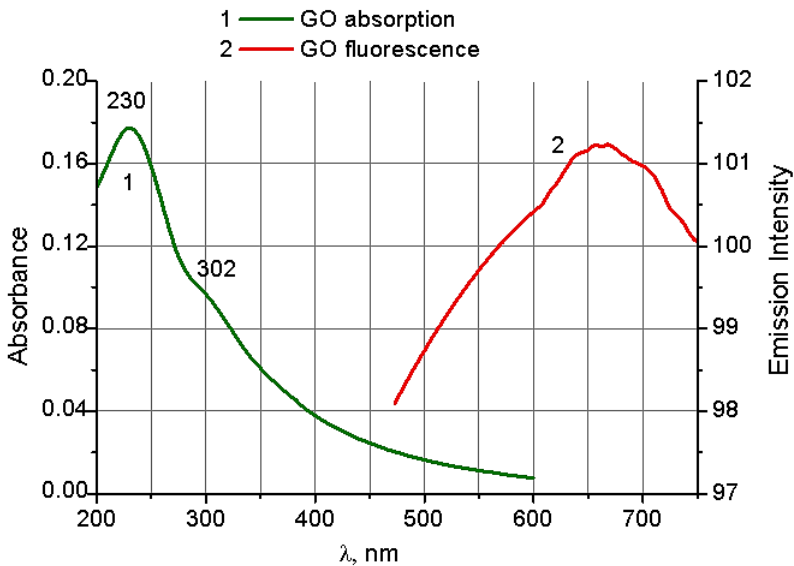
Fig. 4.1. Absorption and emission spectra of GO

The illumination of GO samples was performed with blue laser (473 nm), so no near-UV-to-blue visible fluorescence was noticed, indeed, the low intensity luminescence within the range of 600-700 nm was induced. The shift in the fluorescence peaks of the suspension may be attributed to the differences of the surrounding medium. Pan et al. (2010) have demonstrated that the blue fluorescence of graphene is pH-dependent. The fluorescence is strong enough to be observable by the naked eye at high pH levels, while it is nearly quenched in low pH levels. The

56

explanation is that protonation of the emissive zigzag sites at acidic pH conditions quenches the fluorescence and deprotonation in alkaline conditions, recovers it.

4.1.1.1 GO characterisation with AFM

In order to explore the GO structure in more depth, microscopic techniques such as atomic force microscopy have been employed for the investigation of its structural features. AFM directly gives the apparent thickness of the single-layer GO (around 1 nm, fig. 4.2) as well as the number of layers.
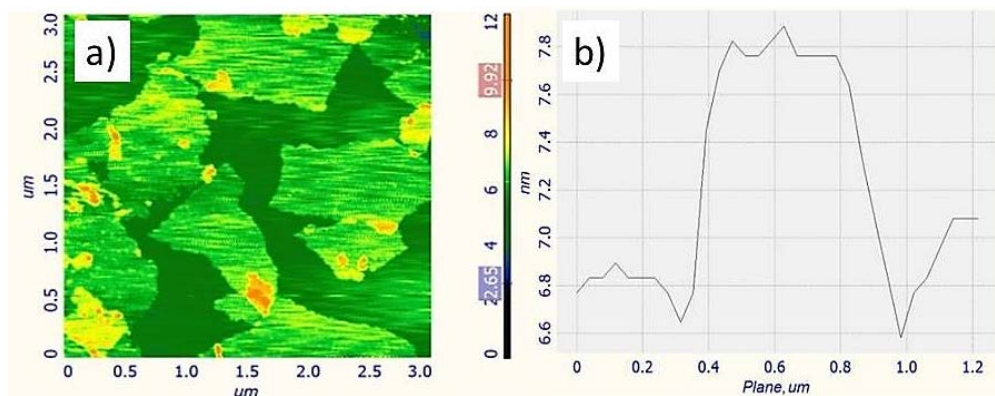
Fig. 4.2. GO characterisation by AFM. a) Height image of GO flakes b) cross section of a GO flake

To prove the impact of sonification for GO solution, the following experiment was performed. The different samples of a) GO sample without sonification b) GO after 30 min sonification and c) after 1 hour sonification were prepared by putting the solution of GO in a sonification bath for the corresponding time, then samples were dropped onto the mica surface and kept for 5 min, after that spin coating was performed. Samples were tested with AFM and the influence of the sonification time was evaluated from the obtained pictures (Fig. 4.3).
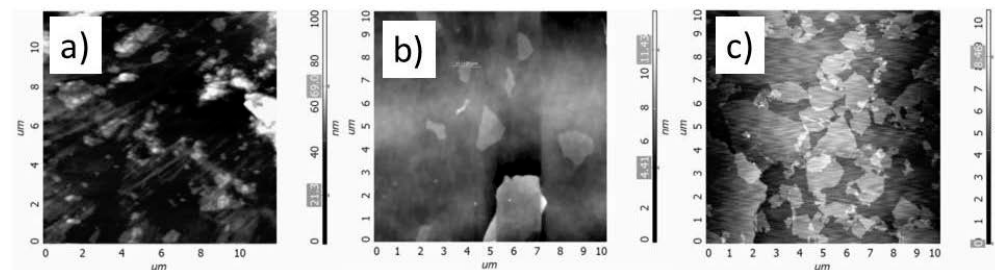
Fig. 4.3. GO characterisation with AFM. a) Without sonification, b) after 30 min sonification, c) GO after 1 hour sonification

From the obtained AFM pictures after 1 hour sonification the small flakes of GO (0.3-0.7 μm) are dominant. After 30 min sonification, the middle size flakes (0.9-1.2 μm) are dominant. Without sonification, the big size flakes (1.2 μm and more) are dominant. According to the manufacturer data sheet (Graphene

Supermarket) the size of flake is: 0.3-0.7 microns and a thickness of 1 atomic layer - at least 80%. So, before all experiments with GO solution, the sonification for at least 1 hour is needed to recover of characteristics provided by producer.

4.1.1.2   GO characterisation with Raman spectroscopy

Raman spectroscopy can be used for both quantitative and qualitative investigations. For example, the amount of layers (single layer, bilayer, etc.) of graphene and the effect of substrates on the graphene characteristics, etc. can be determined by Raman spectroscopy. The Raman spectrum of graphene oxide shows the main features of the carbon materials, D ~1,334 cm^{-1}, G ~1,559 cm^{-1}, 2G ~3,200 cm^{-1} and 2D (often also referred to as G) bands ~2,668 cm^{-1} (using an excitation wavelength of 532 nm). The G band is due to bond-stretching in rings and chains (Pimenta et al., 2007). The D band is caused by the breathing modes of sp^2-atoms in rings. The D-band appears when structural disorder, e.g. impurities and edges, breaks the translational symmetry. The D band intensity can be correlated to the edges and other defects in the graphene sheet (Kudin et al., 2008). Thus, the G and D bands provide useful information on in-plane vibrations and defects, respectively. For graphite the D/G ratio has been related to the in-plane grain-size (Cancado et al., 2006). This ratio gives a means to analyse the disorder in the graphene system. The 2D band gives information on the stacking order and has recently been used as a simple and efficient way to identify single layer graphene sheets. Raman spectroscopy was applied to graphene single layers, bilayers, etc. by different researchers (Ferrari et al., 2006; Balandin et al., 2008). For single-layer graphene the relative intensity between the G and 2D band reverses as compared to multilayer flakes (Ni et al., 2008). Moreover, other nanomaterials can also be characterised using Raman spectroscopy.
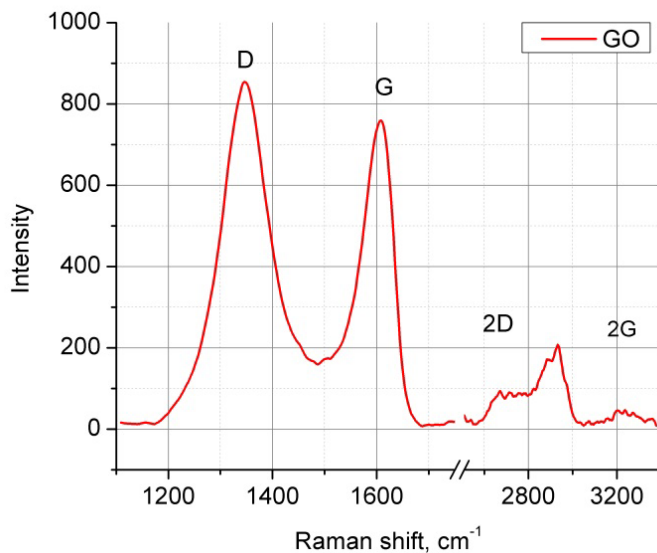
Fig. 4.4. The typical Raman spectra of GO (λ_{ex}- 532 nm)

The typical Raman scattering spectra of the measured GO films presented in Fig. 4.4. The typical band regions of the in-phase vibration of the GO lattice (G and 2G band) are at ~1,600/3,200 cm^{-1} and the disorder band regions caused by the GO edges (D and 2D band) are at ~ 1,334/2,668 cm^{-1}.

4.1.2 Graphene functionalisation with meso-tetra (4-sulfonatophenyl) porphines

A non-covalent interaction of iron and metal-free meso-tetra (4-sulfonatophenyl) porphines (FeTPPS$_4$ and TPPS$_4$) with single-layer graphene was investigated. The central metal atom of porphyrin macrocycle (iron) plays an important role in the integrity of FeTPPS$_4$ on graphene surfaces. The interaction of metal-free TPPS$_4$ with graphene leads to the deprotonation of TPPS$_4$ molecules and not significant Raman enhancement values. The Raman enhancement factors were evaluated as a ratio of background subtracted Raman spectra of the corresponding films on graphene and glass multiplied by factor of 3 which is caused by the difference in the film thicknesses on glass (25 ± 5 nm) and graphene (8 ± 2 nm). For TPPS$_4$ film (pH = 4) the enhancement factor of 4 is obtained for all peaks due to a strict conformity of the spectra (the deviation is ± 0.3). On the contrary, the Raman signals of FeTPPS on graphene are reduced by a factor of 1.5. Deprotonated TPPS$_4$ solutions after the adsorption on the graphene surface demonstrates the appearance of new Raman bands (774, 1,181, 1,653 cm^{-1}) and enhanced Raman signals (1,363, 1,509 cm^{-1}) (Fig. 4.10). A strong non-covalent interaction between deprotonated TPPS$_4$ and graphene is realised through pyrrole and desulphonated phenyl rings of closely located planar TPPS$_4$ molecules on the graphene surface.

4.1.2.1 UV-Vis and Raman characterisation of TPPS/FeTPPS porphyrins

The configuration of the electron cloud of an individual porphyrin molecule and its absorption spectrum are very sensitive to the surrounding media due to the number of free anions/cations presented in the solution. The used porphyrin salts after dissolving in deionised water usually had an acidity of about pH 4. The metal-free TPPS molecules in water solution at pH 4 are diprotonated (Goncalves et al., 2005). The deprotonation process of TPPS molecules in aqueous solution (10^{-5} M) was performed by adding NaOH and checked by UV-Vis spectroscopy. The FeTPPS absorption spectrum does not change in the acidity range of 4.0-6.0. The corresponding UV-Vis spectra of as-prepared diprotonated (pH 4), deprotonated (pH 6) TPPS solutions and FeTPPS at pH 4 are shown in Fig. 4.5.
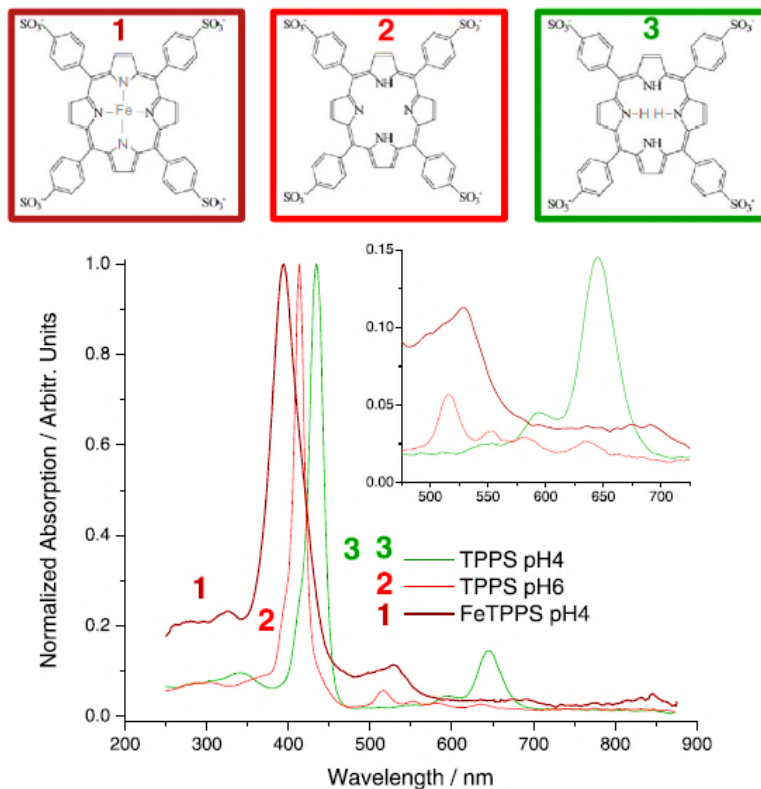
Fig. 4.5. Normalised absorption spectra of diprotonated TPPS (pH 4, green), non-protonated TPPS (pH 6, red) and FeTPPS (pH 4, brown) aqueous solutions (10^{-5} M) (λ_{ex}- 532 nm)

The absorption spectrum of non-protonated TPPS aqueous solution (pH 6) consists of an intense Soret band at 413 nm, caused by the excitation of the porphyrin macrocycle, and four weak Q bands centred at 516, 553, 583 and 635 nm. With a protonation (pH 4) a Soret band is red-shifted to 435 nm, and only three bands are observed in the region of the Q bands: an intense band at 645 nm and weaker bands at 597 and 550 nm. The acidity of porphyrin solutions was controlled and kept at pH 4 or 6 to avoid any possible formation of TPPS *J* and *H*-aggregates and non-stable monoprotonated states in the range of pH 5.0–5.5 (Kelbauskas et al.,2003; Rotomskis et al. 2004; Mchale, 2012). As typical for metalloporphyrins (Horvath et al.*,* 2006), a Soret band of FeTPPS is blue-shifted to 394 nm and a wide band appears centred at 530 nm (Goncalves et al.*,* 2008; Gandini, Yushmanov and Tabak*,* 2001).

The influence of pH and a central metal atom to the configurations of TPPS and FeTPPS molecules in aqueous solutions are proposed in Fig. 4.6.

TPPS4 pH-4   TPPS4 pH-6   FeTPPS4 pH-4
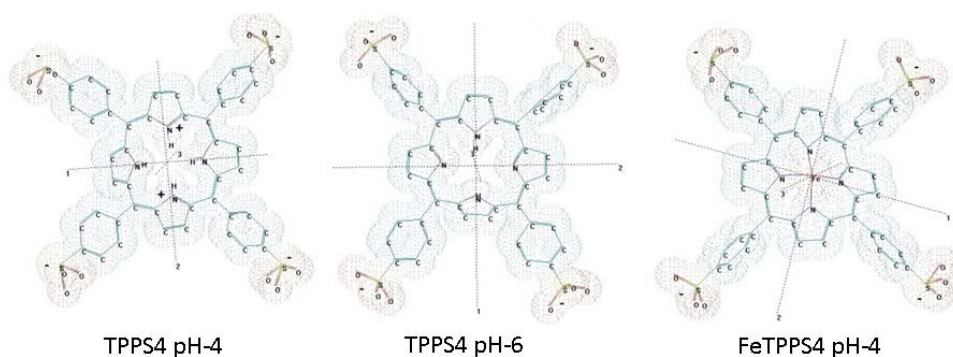
Fig. 4.6. The proposed molecular configurations of TPPS and FeTPPS at different pH are drawn using HyperChem 5.02 software

The measured Raman spectra of TPPS and FeTPPS films deposited on the glass substrates from aqueous solution are shown in Fig. 4.7. The TPPS (pH 4) mode at 1,477 cm^{-1} can be assigned to the in-plane motion of the phenyl ring (Friedsen et al., 2009). This mode disappears in the free base as a result of the almost perpendicular orientation of the phenyl rings. These configuration changes also lead to a downshift of the out-of-plane motion of the porphyrin core to 311 cm^{-1}, downshift of totally symmetric pyrrole breathing vibrations from 987 and 1,017 cm^{-1} to 964 and 1,002 cm^{-1}; upshift of phenyl deformation vibrations to 718 cm^{-1} and an upshift of C_b-C_b stretch from 1,539 to 1,548 cm^{-1} after deprotonation is in line with the 'rule of protonation' for stretching vibrations (Akins, Zhu and Guo, 1996). These configuration changes also lead to the significant enhancement of pyrrole modes at 810, 1,330 and 1,363 cm^{-1}, C_b-H bending deformations at 1,089 and 1,144 cm^{-1} and a C_m-phenyl stretching mode at 1,239 cm^{-1} (see Table 4.1).
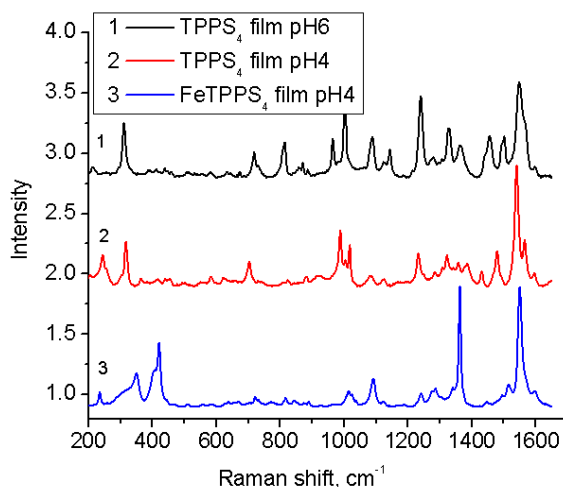
Fig. 4.7. Normalised Raman spectra of diprotonated TPPS (pH 4), non-protonated TPPS (pH 6) and FeTPPS (pH 4) films formed onto the glass substrates (λ_{ex}- 532 nm)

Table 4.1. The assignment of Raman bands of TPPS

The mode explanation	TPPS (pH 4)	Changes in TPPS (pH 6)
Out-of-plane motion of the porphyrin core	316 cm^{-1}	Downshift to 311 cm^{-1}
Phenyl deformation vibrations	704 cm^{-1}	Upshift to 718 cm^{-1}
Symmetric pyrrole breathing vibrations	987 and 1,017 cm^{-1}	Downshift to 964 and 1,002cm^{-1}
Pyrrole modes	810, 1,330 and 1,363 cm^{-1}	Enhanced peaks
C_b-H bending deformations	1,089 and 1,144 cm^{-1}	Enhanced peaks
C_m-phenyl stretching mode	1,239 cm^{-1}	Enhanced peak
Phenyl ring motion	1,477 cm^{-1}	Disappears
C_b-C_b stretch	1,539 cm^{-1}	Upshift to 1,548 cm^{-1}

Because the Raman spectra of FeTPPS spectrum is not being changed in the acidity range of pH 4–6 so only the single spectrum of FeTPPS film (pH 4) is shown. In the case of FeTPPS film, an iron atom could be a cause of another feature in the difference spectrum centred at 420 and 1,362 cm^{-1}, corresponding to the observed increase of Fe-O-Fe stretching vibrations. The disappearance of the mode at 1,477 cm^{-1} indicates a rotation of the phenyl rings and on a less protonated state of FeTPPS when the film is formed. The broad peak at 314 cm^{-1} is relative to the motion of the porphyrin core, and allows the assumption that FeTPPS molecules are strongly deformed after the formation of film.

4.1.2.2 Characterisation of porphyrin films on CVD graphene

To investigate the graphene impact on porphyrins, the measurements with Raman spectroscopy were performed. The Raman spectrum of a non-protonated TPPS after an interaction with graphene strongly correlated with the one of the film formed on glass substrate (Fig. 4.8 and Fig. 4.9). Whereas in the case of purchased CVD graphene, which was on a Si surface, during measurements an intensive Si band on 521 cm^{-1} and second, non-so intensive band around 1,000 cm^{-1} was visible (Fig. 4.8).
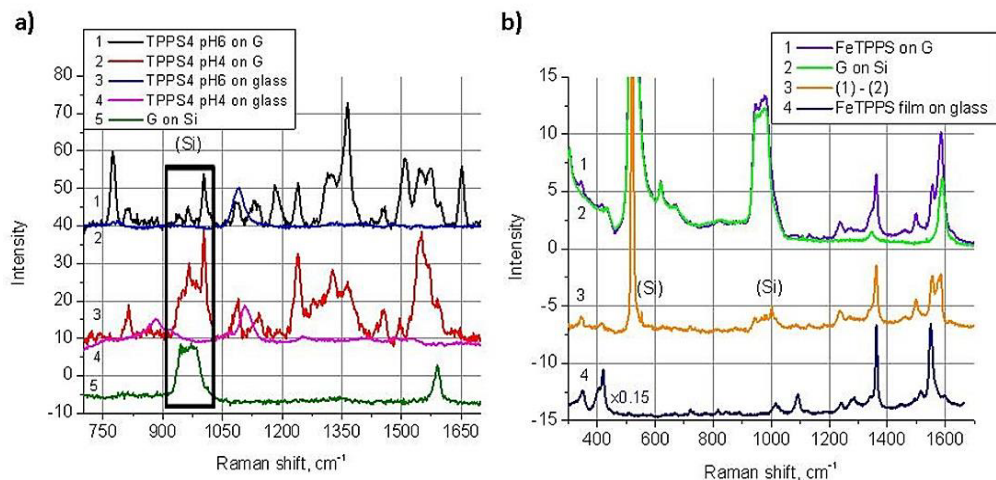
Fig. 4.8. The normalised Raman spectra of a) TPPS and b) FeTPPS on glass and graphene surface (λ_{ex}- 532 nm)

While non-protonated TPPS is adsorbed on graphene, its Raman spectrum differs from the non-protonated film on glass. There is a redistribution in the peak intensities, a significant enhancement of peaks (1,363, 1,509 cm^{-1}), and even an appearance of new peaks (774, 1,181, 1,653 cm^{-1}) (Fig. 4.8). The sensitive to the protonation v_2 C_b-C_b stretching mode at 1,548 cm^{-1} is not shifted, but v_{11} C_b-C_b stretching mode at 1,510 cm^{-1} is upshifted and enhanced. Another enhanced band at 1,365 cm^{-1} can be assigned to pyrrole vibrations which also involve the C_b atom. The mechanism of Raman enhancement on graphene is usually explained by the charge-transfer phenomenon (Huang et al., 2012) by analogy with the chemical enhancement mechanism in 'classic' SERS, when an electronic coupling between molecules and metal substrate occurs. The peak at 1,184 cm^{-1} can be a Raman fingerprint of symmetric phenyl vibrations of desulphonated TPPS, TPP (Saini, 2006), and should be considered with a rising peak at 1,575 cm^{-1} assigned to phenyl C=C stretch. It was shown in that the *p*-sulphonation of TPP phenyl groups causes a weakening of the peak at 1,575 cm^{-1}, and it disappears for TPPS and *vice versa*, it's strengthening could be evidence of the desulphonation of phenyl rings of non-protonated TPPS. Two other bands, arising at 780 and 1,650 cm^{-1}, can be assigned to significantly enhanced pyrrole vibrations (Griffiths and Chalmers, 2002; Blom et al., 1986).

After interaction of FeTPPS macrocycle with graphene, there were no changes in the peaks, which are related to the vibrations of an iron atom- 417 and 1,364 cm^{-1}. The C_b-C_b stretching vibration of FeTPPS on the glass surface at 1,550 cm^{-1} is more upshifted, implying a less protonated condition of FeTPPS molecule on graphene. The relative increase of the C_m- phenyl (1,236 cm^{-1}) and C_b-C_b (1,499 cm^{-1}) stretching vibrations together with a significant decrease of the vibrations involving an iron atom (417 and 889 cm^{-1}) correspond to the strong deformation of FeTPPS core after an interaction with graphene and a structural disorder of the film. In the case of both TPPS and FeTPPS a weak Raman signal at 1,477 cm^{-1} indicates that the

phenyl rings are perpendicular to the porphyrin core as shown in Fig. 4.11 (Buchner, 2010).
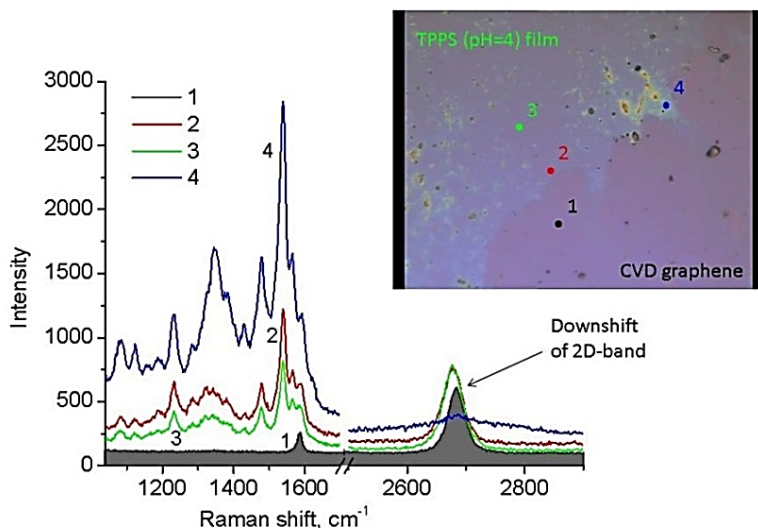
Fig. 4.9. The Raman spectra of TPPS film on CVD graphene in different places (λ_{ex}- 532 nm)

The measured thicknesses of uniform films of the different porphyrin solutions adsorbed on chemical vapour deposition (CVD) graphene were typically less than 10 nm (see Fig. 4.10).
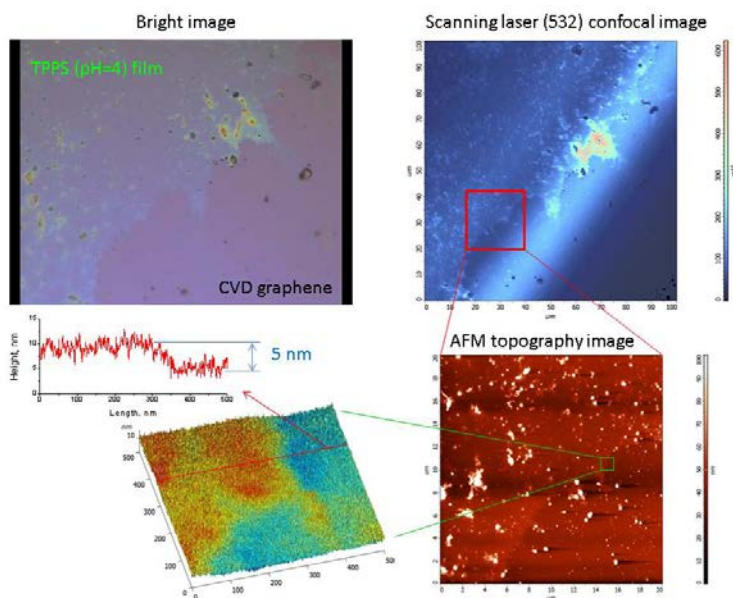
Fig. 4.10. The bright, confocal and AFM images of TPPS film formed on CVD graphene

4.1.2.3   Conclusions

The protonation of porphyrin macrocycle or the existence of a central metal atom for the TPPS family plays an important role in the molecular conformation and orientation when interacting with single-layer graphene (see Fig. 4.11). The interaction of diprotonated metal-free TPPS with graphene leads to the deprotonation process of the porphyrin macrocycle. The downshifts of G and 2D Raman peaks of graphene after an interaction directly imply a charge transfer from TPPS molecules to graphene resulting in the electron doping of graphene, but the Raman enhancement factors are relatively low. The existence of a central metal atom in the porphyrin macrocycle (iron) is important in the integrity of the FeTPPS molecule during an interaction, but results in the decreased Raman signals in spite of the observed charge transfer effect. Initially deprotonated TPPS undergoes the atomic changes after an interaction with graphene, which leads to the appearance of new Raman bands and at least one order of magnitude higher enhancement factor for some pyrrole modes. The proposed explanation of enhancement is that a strong interaction is realised through the pyrrole and planar desulphonated phenyl rings of a closely located TPPS molecule on a single-layer graphene surface. A variety in the central metal atom of porphyrin macrocycle or its protonation opens wide opportunities for the fabrication of novel composite graphene-porphyrin nanomaterials with predetermined properties.
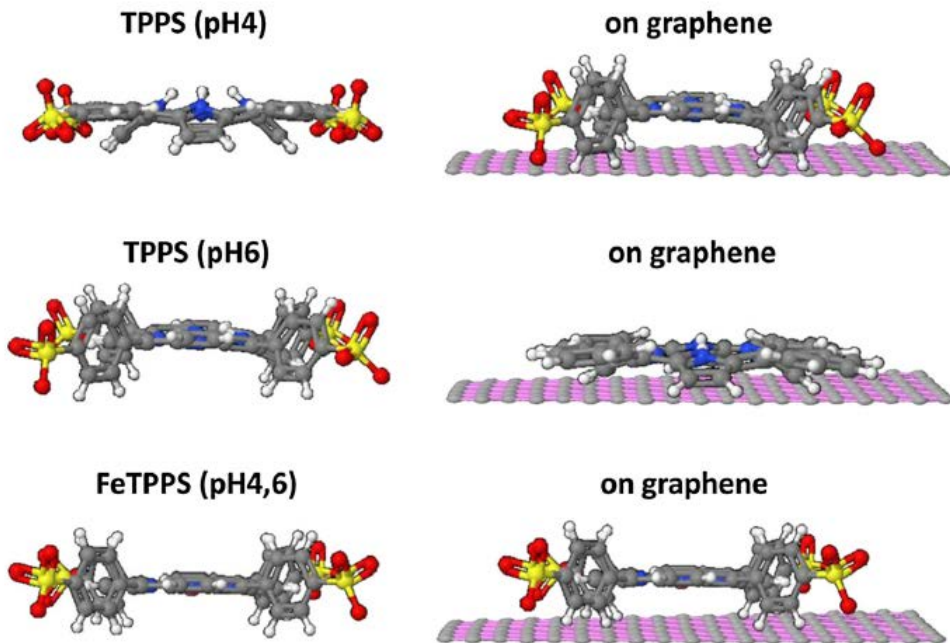
Fig. 4.11. The configurations of TPPS and FeTPPS molecules in aqueous solutions and when adsorbed onto graphene (right)

4.1.3 Graphene oxide functionalisation with hematoporphyrin

A covalent interaction of hematoporphyrin (HP) with functionalised graphene-graphene oxide was investigated. A combination of optical techniques, as UV-Vis absorption, luminescence properties and Raman scattering, can be efficiently used to detect an interfacial structure of hematoporphyrin/graphene oxide (HP/GO) nanoensembles. The stable in aqueous media at neutral pH HP/GO nanocomposites were obtained as a result of the esterification reaction catalysed by sulfuric acid (SA). The nanocomposite with stronger absorption and emission represents a layered structure composed of hematoporphyrin oligomers adsorbed on the surface of GO in a monolayer through covalent, electrostatic and *p*-stacking interactions. The formation of such hybrid structures, where graphene oxide plays a role of a non-toxic sheet-like nanocarrier, opens the way to create a functional nanocomposite with a high-level of selective emission and efficient photosensitising ability using unique graphene properties.

4.1.3.1   Characterisation of hematoporphyrin

The configuration of an electron cloud of hematoporphyrin and its absorption spectrum also depends on the surrounding media. The HP after dissolving in deionised water had an acidity of about pH 7. Under neutral conditions (pH~7), carboxyl groups of hematoporphyrin are mainly deprotonated and become negatively charged; oppositely charged carboxyl croups and amino groups stimulate aggregation of hematoporphyrin molecules (Marchetti and Errazu, 2008) (Fig. 4.12). The pH changing process of HP molecules in aqueous solution was performed by adding H_2SO_4 or NaOH and controlling by UV-Vis spectroscopy.
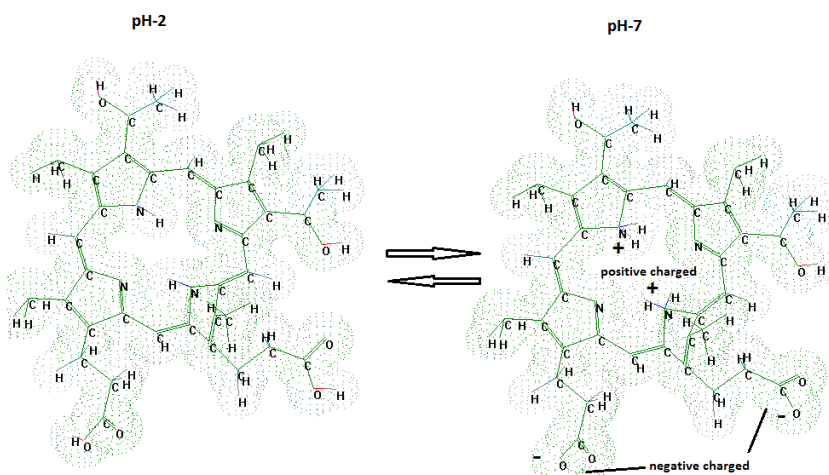
Fig. 4.12. The changes of hematoporphyrin under acidic and neutral pH level

Absorption and emission spectra of hematoporphyrin are presented in Fig. 4.13. The data in Table 4.2 showed that treatment with sulfuric acid essentially changes both the absorption and emission spectra of HP. The specific features of a strong Soret band (position, narrow half-width, strong vibronic coupling, etc.)

indicates that at pH~2 a monomer form of HP dominates in the solution. The hypochromic (blue) shift, wide and less intensive absorption bands indicate the aggregation of HP in the aqueous solution at neutral pH~7. The emission spectra of HP at pH~7 show typical fluorescence peaks on 616 nm and 676 nm; after adding sulfuric acid we observed the change of the spectrum with a main peak at 655 nm.

Table 4.2. Absorption and emission range/peaks

	Absorption range, nm	Main absorption peaks, nm	Emission range, nm	Main emission peaks, nm	Interpretation
pH~2	220-585	381, 399, 550	585-750	623, 652, 671	Monomer form
pH~7		367, 390		616, 674	Aggregate form

The observed features are in good agreement with the model that sulfuric acid reduces aggregation of HP and shifts the equilibrium to the monomer form. Under neutral conditions (pH~7), carboxyl groups are mainly deprotonated (the *pKa* of carboxyl groups are mainly in the range 4-5), and become negatively charged; oppositely charged carboxyl groups and amino groups stimulate the aggregation of hematoporphyrin molecules. Sulfuric acid changes the pH below *pKa* disturbing electrostatic interactions and leads to the disaggregation of HP aggregate.
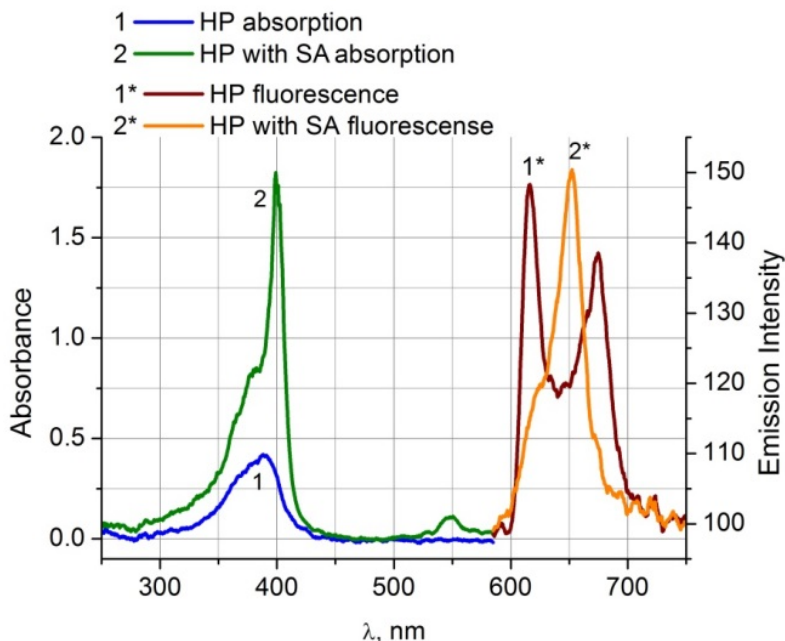
Fig. 4.13. Absorption and emission spectra of hematoporphyrin with and without sulfuric acid, respectively

The influence of acidity on the optical spectra of HP is a good example of the processes where intermolecular coupling driven by long-range electronic interactions induce reciprocal polarisation of molecules or charge transfer between the molecules within aggregate (Fig. 4.14). Observed absorption and emission changes are due to the disaggregation of HP's clusters (with main fraction of face-to-face dimers) as a result of the change in the distribution of charge within the HP molecule. Indeed, with the decreasing pH tendency to charge both the central ring (*pKa* 4.9) and the peripheral substituent's (*pKa* of carboxyl groups are mainly in the range 4-5) increases result (for pH less than c.a. 4) in positively and negatively charged central and peripheral parts of HP correspondingly.
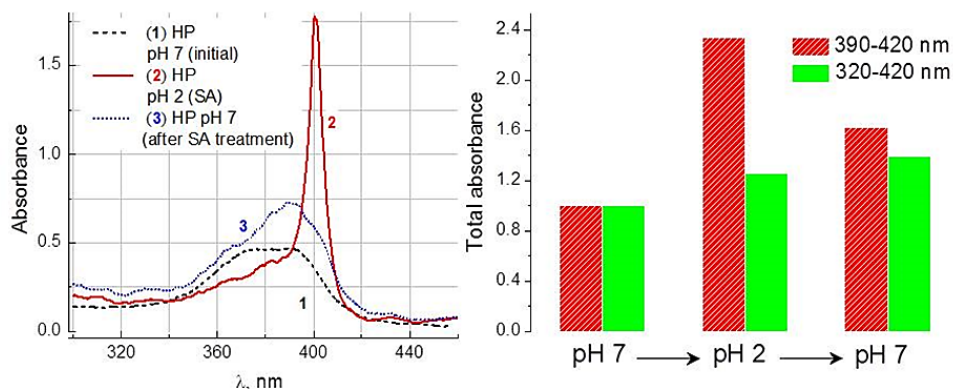
Fig. 4.14. The influence of acidity on the absorption spectra of HP; under pH 7 - after adding SA pH 2 - after adding NaOH into the previous solution to reach pH 7

Consequently, at acidic pH (c.a. 2) HP exist in solution preferably in the monomolecular form owing to electrostatic repulsion. The process is completely reversible within the pH range from 2 to 7; the data obtained for this process with hydrochloric and nitric acid supports this model (Fig. 4.15). However, in the case of SA achieving reversibility is possible only at much higher pH values in the alkaline area (approx. pH 10). This feature is due to the esterification reaction catalysed by SA, resulting in the formation of linkages between separate molecules HP. More information can be found in the literature (Dougherty, Potter and Weishaupt, 1989).
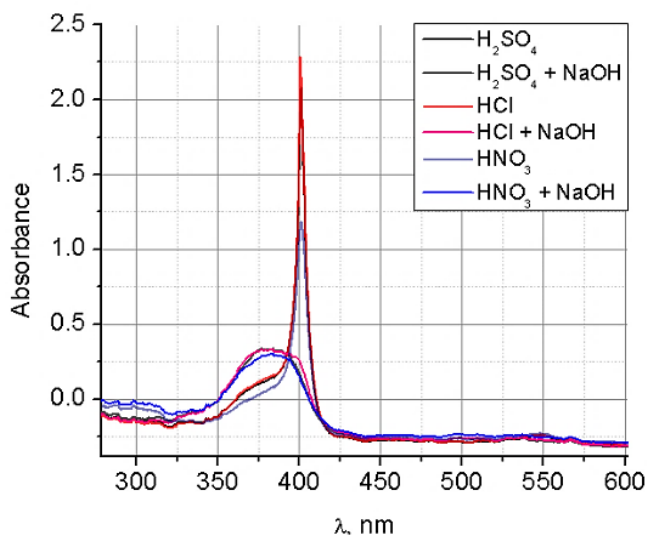
Fig. 4.15. HP absorption spectra changes after adding different types of acids

4.1.3.2 Graphene oxide absorption and emission changes under sulfuric acid treatment

The absorption spectrum of GO solution in water ranging from 200 to 800 nm shows a main peak at ~230 nm and a weak shoulder peak at ~302 nm (Shang et al., 2012). Typical GO absorption spectra in deionized water are presented in Fig. 4.16. The addition of SA had no significant influence on GO absorption spectra. Excitation with a blue laser (473 nm) shows low luminescence within the range of 600-700 nm. Owing to the low absorption and emission efficiency as well as structureless spectra of GO within the visible region, only small changes in optical spectra were observed when SA was added to the GO solution.
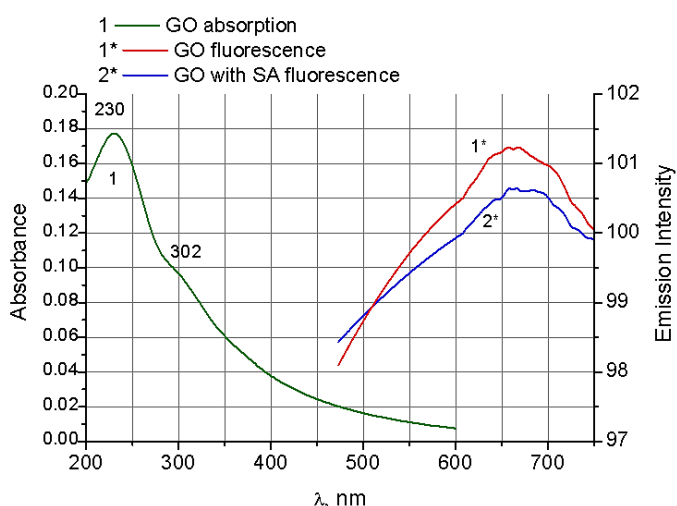
Fig. 4.16. Absorption spectra of GO and emission spectra of GO with and without SA

Within one hour after adding SA some visible macroscopic aggregation within GO solutions may be seen with the naked eye. Typical Raman scattering spectra of the GO films treated with and without SA are presented in Fig. 4.17 within the regions of the in-phase vibration of the GO lattice (G/2G band) at c.a. 1,600/3,200 cm^{-1} and the disorder band caused by the GO edges (D/2D band) at approximately 1,334/2,668 cm^{-1}. The decreasing of D/G ratio at low pH as well as G band shift to the high energy indicates the decreasing of the defects and formation of more ordered structure (Kudin et al., 2008).
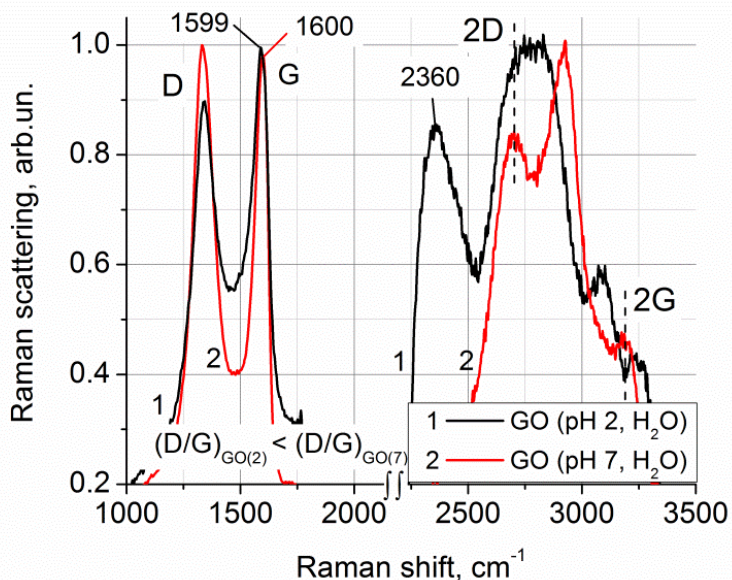
Fig. 4.17. The typical Raman spectra of GO treated with SA (λ_{ex}- 532 nm)

4.1.3.3   The interaction between GO and HP

The interaction between GO and HP were analysed by UV-Vis and Raman spectroscopy, FTIR. In Fig. 4.18 typical absorption and emission spectra of HP mixed with GO at neutral pH is presented. After addition of GO, the Soret band of HP undergoes a bathochromic shift from 381 to 388 nm; strong quenching of fluorescence and formation of macroscopic aggregates in solutions were also observed. All those features can be explained by the formation of HP~GO aggregates.
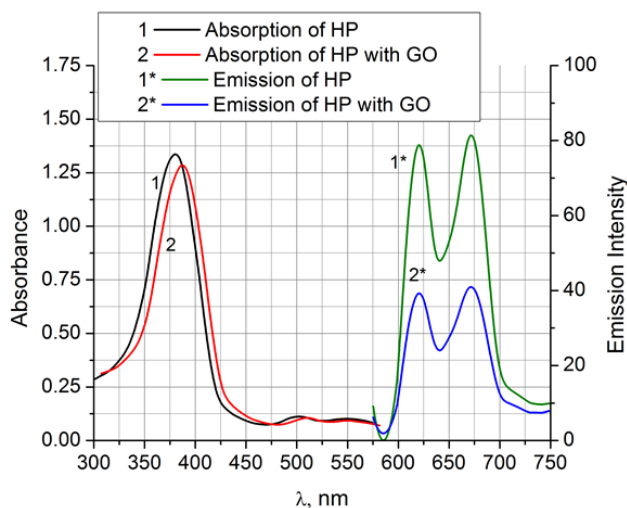
Fig. 4.18. Absorption and emission spectra of HP at neutral pH with and without GO, respectively

Weak HP peaks on 1,343 and 1,595 cm^{-1} could be observed. The Substituted phenyl ring of HP shows at 1,595 cm^{-1} (Gao et al., 2013). The band at 1,343 cm^{-1} can be detected in the region of the oxidation state marker band. Graphene oxide has a couple of Raman-active bands visible in the spectra (Fig. 4.19), the in-phase vibration of the graphene oxide lattice (G band) at 1,596 cm^{-1} as well as the disorder band caused by the graphene oxide edges (D band) at approximately 1,334 cm^{-1}. The hydroxyl groups yield a series of bands around 1,300-1,370 cm^{-1}. The observed decrease in amplitude could be caused by the decreasing number of free hydroxyl groups, and the shift to 1,342 cm^{-1} could be caused by the appearance of a different type of groups ester links. The G band shifts from 1,596 to 1,594 cm^{-1} could also be partially responsible for the higher G band frequencies if significant unmodified graphene oxide areas remain. The addition of epoxy and hydroxyl groups is a broadening of the G band (Kudin et al., 2008). Raman spectra of GO coupled to the porphyrin fragment show spectral features which can also be recognised in the spectrum such as the band at 1,342 cm^{-1} attributed to the porphyrin fragment. The experiments by Silvia Giordani et al. (2009) show that after connection with porphyrin in the spectrum the porphyrin fragments can be recognised. Also, the noticeable aggregates can be observed only in solution with GO and HP treated with SA. The possible explanation is that sulfuric acid was a catalyst for the connection between GO and HP:

$$\text{HP-COOH} + \text{GO-OH} \xleftarrow{\text{conc. } H_2SO_4} \text{HP-COO-GO} + H_2O \quad (4.1)$$
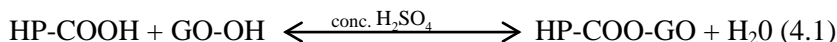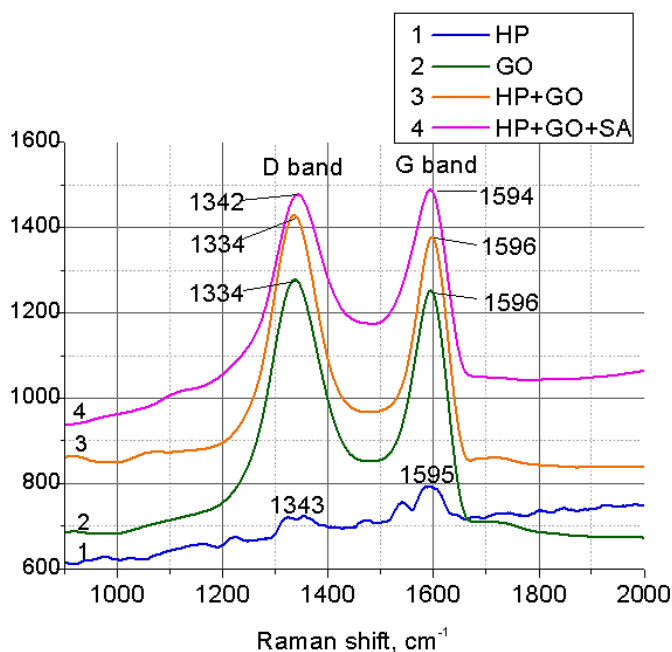
Fig. 4.19. Raman spectra of GO, HP and GO with HP with and without SA (λ_{ex}- 532 nm)

To clarify the nature of GO~HP interactions and to indicate the reduction of oxygen-containing groups of GO, FTIR spectroscopy was used. FTIR spectra of the samples are presented in Fig. 4.20. Results show that under SA treatment the intensity of the bands specific for both carboxyl and hydroxyl groups are considerably decreased (Su et al.*,* 2012). Fig. 4.20 shows the characteristic bands of GO and HP around 892 cm^{-1} (C-H deformation vibration of GO plane surface), 1,066 cm^{-1} for C-O (ν (alkoxy)), 1,066 cm^{-1} for C-O (ν(epoxy)) 1,394 cm^{-1} for O-H (ν (carboxyl)) and C-N vibrations (from HP), also because of the methylene group (from HP), 1,634 cm^{-1} for C=O (carboxyl), c.a. 3,200-3,300 cm^{-1} for O-H of intercalated water and c.a. 3,668 cm^{-1} for OH (from GO and HP) also NH (from HP) vibrations. After the interaction with HP, the absorption bands of both C=O and O-H are considerably decreased. The results imply that most of the oxygen-containing groups of GO were decreased by the interaction with HP. So, the FTIR spectroscopy indicate the reduction of oxygen-containing groups of GO and is in good agreement with the assumption of GO~HP bonding as the result of the esterification reaction catalysed by SA.
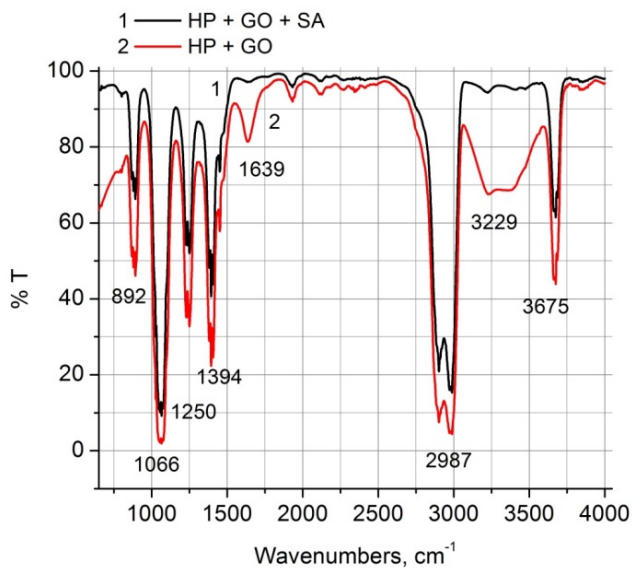
Fig. 4.20. FTIR spectra of mixture of GO and HP treated with SA and without SA

To evaluate the spatial organisation and stoichiometry of GO~HP aggregates, optical measurements with serially increased concentrations of GO in the mixture (Fig. 4.22) were performed. Total emission intensity of the HP/GO mixture depends on the GO~HP nanocomposite fraction where GO quench HP emissions. Analysis of the data presented in Fig. 4.22 shows that at the neutral pH full quenching of the HP emission was achieved at HP/GO (surface/surface) ratio ~c.a. 4; it corresponds to the situation when both sides of the GO flake were covered by a bilayer of HP molecules.

At acidic pH, reached by SA full quenching reached at HP/GO ration c.a. 2 that corresponds to the situation when each side of a GO flake is covered by a monolayer of HP molecules (Fig. 4.21).
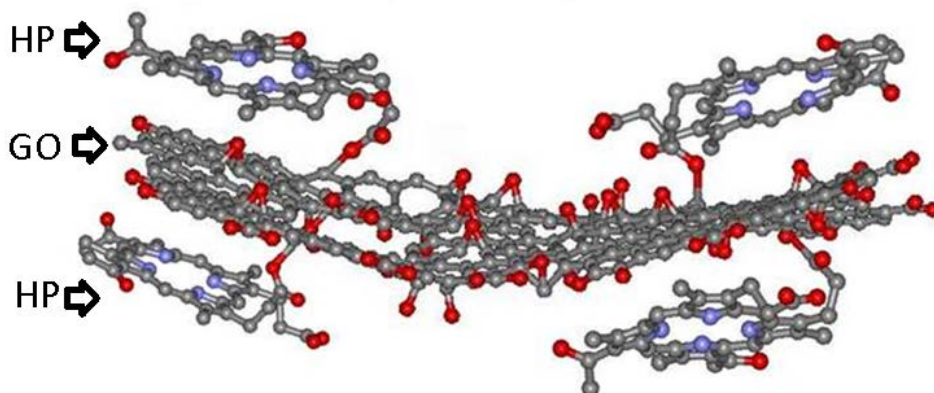
Fig. 4.21. Possible structural composition of graphene oxide flake covered by HP molecules

Nonlinear regression analysis of the experimental data (using logistic curve functions (3.6)) was performed and presented in Fig. 4.22 to support conclusion that at acidic pH a GO flake is covered by a monolayer of HP molecules. Assuming that the limiting surface area of HP molecules immobilised on GO is similar for both pH levels, the obtained difference in γ_0 (21.4 and 9.1 at pH 7 and 2, correspondingly) may be explained by "increasing the concentration" of competitor (HP) at pH 2. So, taking into account that the HP/GO ratio calculated in the surface/surface values, the two times smaller value of γ_0 at pH 2 may be explained by dissociation of HP dimers and differences in the composition of GO~HP aggregates at pH 2 and 7.
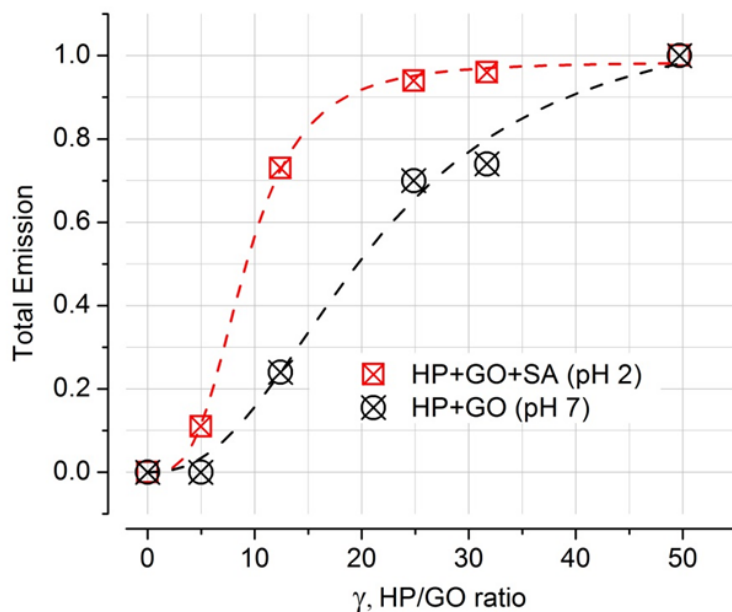
Fig. 4.22. GO induced quenching of HP emission versus HP/GO ratio γ at neutral and acidic pH

The calculated values of power p (function (3.6) which represents the order of the reaction in the competitor (HP) also depend on the pH. The larger the parameter p, the greater the degree to which the parallel processes of binding of the analyte (HP) with multidentate carrier (GO) occur. Keeping in mind that HP may either be adsorbed (without emission quenched by GO) or free moving with specific emission in solution, power p is the effective order of the interfacial reaction with respect to the HP at the surface of GO. The obtained increased p at low pH (3.4 versus 2.3 for pH 2 and 7, correspondingly) is in agreement with the model assuming dissociation of HP's dimers at low pH and increasing the number of parallel binding of the HP molecules by different centres on the GO surface.

To clarify the formation of GO~HP composites, the SEM measurement was performed. The SEM picture of the sample is presented in Fig. 4.23. Results show that under SA treatment the two types of composites could be formed: the GO flake

covered with porphyrins mainly in corners (Fig. 4.23, a) and the GO flake fully covered with porphyrin molecules (Fig. 4.23, b).
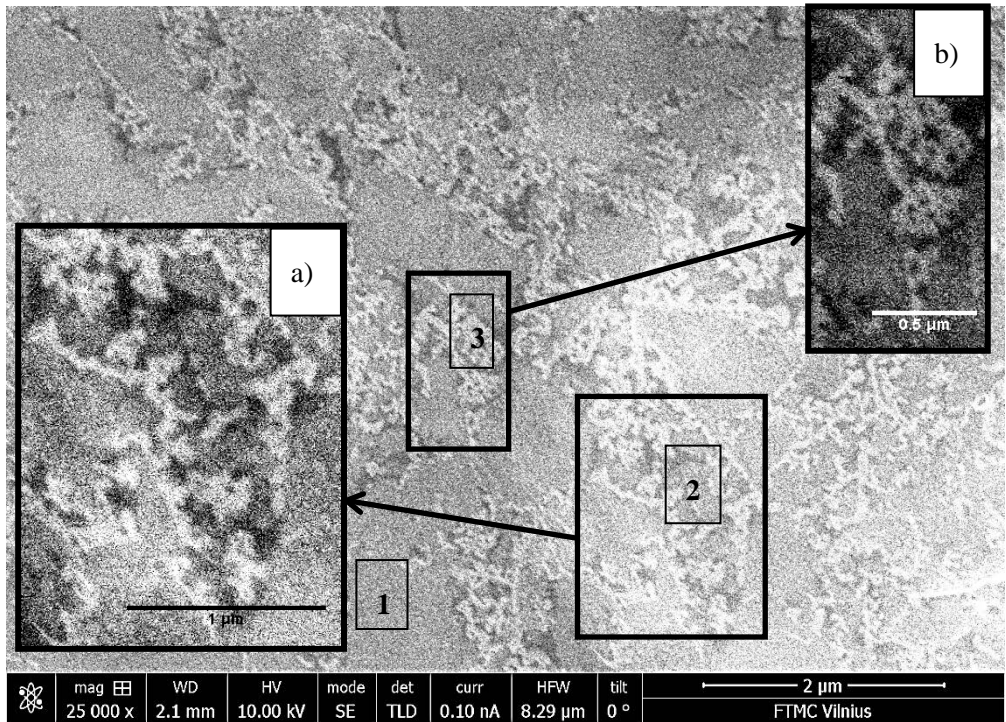
Fig. 4.23. SEM picture of composites based GO and HP under the SA treatment

The energy dispersive X-Ray spectroscopy (EDX) analysis (Fig. 4.23) confirmed the suggestions showing that spectrum 1 indicates the Si surface, whereas spectrum 2 indicates the carbon-based layer and the second layer (spectrum 3) is from porphyrin (see Table 4.3). So, the EDX results suggest that the obtained few layer structures was formed from "base" graphene oxide and "top" formed from porphyrins.

Table 4.3. EDX analysis of composites based GO and HP under the SA treatment

Results in atomic %	C	N	O	Na	Si	S
Spectrum 1	5.83	1.16	2.39	0.08	90.19	0.35
Spectrum 2	15.09	1.84	5.14	0.09	76.77	1.07
Spectrum 3	27.67	10.48	45.09	2.56	3.01	11.19

On the basis of the experimental observations of typical absorption, emission, FTIR and Raman scattering spectra, a plausible interpretation could be proposed for the driven forces of the induced reactions, final products and processes of their formation as schematically illustrated in the scheme (Fig. 4.24).
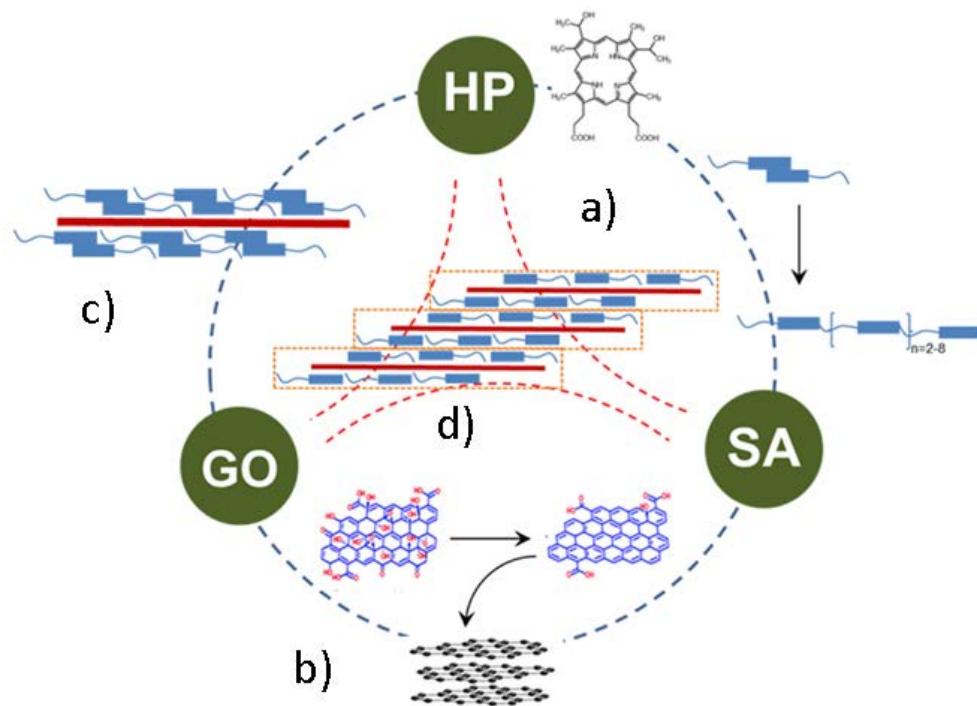
Fig. 4.24. The schematic diagram of the core processes illustrating the diversity of the supramolecular architectures formed by HP and GO at neutral pH and under SA treatment a) as the results of esterification reaction catalysed by SA single HP molecules form oligomers b) GO under SA treatment decreases the number of internal defects located on the perimeter of the flakes; reduced GO acquire the ability to form more ordered structures, which are similar to the nanostructured graphite c) HP molecules are captured by GO flakes, leading to the formation of GO~HP/GO complex with bilayer (pH 7) and monolayer (pH 2) of HP molecules d) adding SA into an aqueous dispersion of HP and GO supramolecular nanocomposites could also be assembled with intercalated layers of HP molecules between GO 2D sheets

The influences of acidity on the processes involving GO differs from those that occur for HP. Geometrically GO could be figured as a graphene fragment, whose edge is mainly decorated with carbonyl and carboxyl groups and base plane with epoxide and hydroxyl groups. Due to the large amount of oxygen containing defect sites on the base plane GO does not aggregate at neutral pH. Under SA treatment the number of internal defects (oxygen-containing groups) located preferably on the perimeter of the individual flakes decreases (Chen, Yan, 2010,). This endows GO flakes with amphiphilicity, where the periphery is inclined to the

hydrophilic, while the centre is hydrophobic. As a result of this modification amphiphilic flakes of partly reduced GO acquire the ability to form ordered structures with densely packed central part surrounded by hydrophilic edges directed to the aqueous environment, which are similar to the nanostructured graphite. Raman scattering measurements confirm this conclusion (Fig. 4.17). D and G bands are broadened, shifted to lower energies and the band at 2,350 cm^{-1} starts to dominate within the low-energy region of the spectrum. According to the manufacturer data sheet this band is specific for the nanocrystalline graphite produced by the same method as GO.

Upon the introduction of HP molecules into an aqueous dispersion of GO at neutral pH, HP molecules are captured by the 2D GO's flakes, leading to the formation of GO~HP complex, which is driven by the π-π staking interactions between the locally distributed poly-aromatic ring of GO nanosheets and flattened HP molecules (in the form of face-to-face dimers). It is reasonable to assume (Hambright, Smith, 1975) that in these complexes HP molecules adopt a coplanar conformation, so, even weak adhesion between two-dimensional solids may perturb their optical properties owing to their low dimensionality. Similar to GO, rigid porphyrin structures have 2D delocalised 18 π-electron conjugated electron systems that induces their inclination to stacking through π-π interactions and prospective electron-transfer ability. In line with the reported data, the non-covalent action of graphene with various organic molecules is realised through π-π stacking, electrostatic interaction and hydrogen bonding (Yang et al., 2011). Molecular dynamic simulation (Nicolai et al., 2013) of GO based nanocomposite shows that the microscopic mechanism of interactions mainly arises from the sp^2 hybridised π-conjugated structured of GO and HP, which engenders π-π interaction. It was found that as the result of the mixing of GO and HP UV-Vis spectrum of conjugate shows the characteristic red shift of the π-π Soret band from 381 nm to 388 nm. This shift implies that the energy gap between the ground and exited orbitals of HP in nanocomposite is decreasing owing to the interactions between GO and HP compared with single HP.

A strong fluorescence quenching of the HP in the presence of GO indicate that efficient charge or energy transfer occurred from the excited state of the porphyrin to GO. The efficiency of fluorescence quenching of HP in the GO~HP ensemble was investigated by using consecutive measurements with increasing concentrations of GO, suggesting that electron/energy-transfer phenomena occur within the nanoensemble. With an increase of the GO concentrations, the aggregation of HP in GO~HP is also increased, and for the HP/GO ratio in c.a. 4 (surface/surface) full fading of the luminescence intensity of GO~HP was achieved.

This finding is due to the formation of stable aggregates where HP in dimer form fully covers both sides of the GO flakes (scheme, Fig. 4.24).
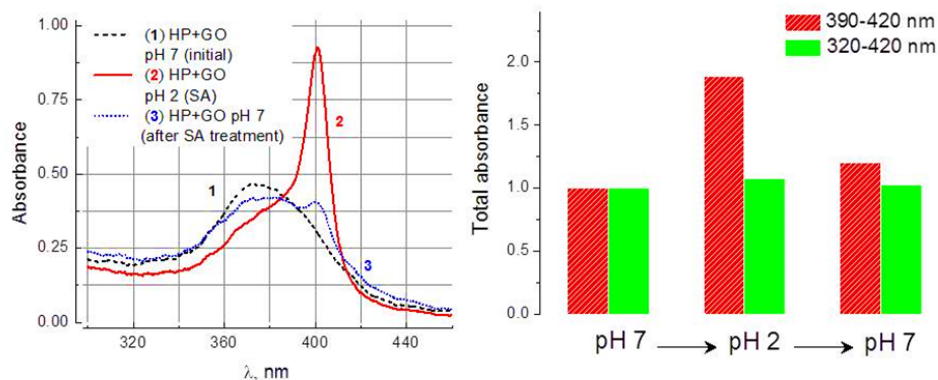
Fig. 4.25. The influence of acidity on spectra of HP with GO; under pH 7, after SA adding (pH 2) and after adding NaOH to reach pH 7

The addition of SA into an aqueous dispersion of HP and GO induces the formation of layered supramolecular nanocomposites (Fig. 4.25). Similar to measurements at normal pH consecutive measurements at acidic pH shows that, as the concentration of HP increase, HP monomers approaching the GO tend to parallel to the GO surface; the 2D GO nanosheets with decreased intra-basal defects play an important role in this kind of GO-assisted self-assembling. The formation of nanographite is not observed, the suppression of luminescence HP is much less effective in respect of the situation at normal pH, a similar level of suppression observed at approximately double the concentration of GO (or half the concentration of HP). So, it is reasonable to conclude that porphyrins adsorb on the surface of GO in a monolayer through electrostatic and π–stacking interactions with the ensuing organisation into 2D layered 3D stacks. It is interesting that there are no shifts of HP absorption bands within GO~HP complexes at low pH. Indeed, the spectral shift of the Soret band induced by GO~HP interactions under SA treatment is negligible compared to HP-GO aggregates at neutral pH (c.a.7.2). This observation can be explained by the fact that at normal pH GO induces some distortion of electronic structure of HP dimer pairs whereas at acidic pH stacking interactions between GO nanosheets compensate for the electronic influence on the intercalated monolayer of HP molecules.

The stability of the GO~HP nanocomposite formed at acidic pH under SA treatment is sufficiently high in respect to one formed at neutral pH, the nanocomposite specific spectra was stable at least 2 h after the pH change from acidic to normal values. This also shows that there are additional chemical bonds between the GO flakes and HP, and the interaction between them is not only a physical adsorption. The short discussion presented above enables us to conclude that not only do strong π-π interactions occur efficiently between GO and HP in the areas of spatial stacking, but additional chemical bonds form between GO and HP under SA treatment. The formation of such hybrid structures, where GO plays the role of a non-toxic sheet-like nanocarrier, opens the way to create functional nanocomposites with a high level of selective emission and efficient photosensitisers

(for PDT) utilising unique graphene properties as a singlet oxygen generation enhancer (Tian et al., 2011; Wojtoniszak, 2013).

4.1.3.4 Conclusions

In this work absorption, emission, FTIR and Raman scattering spectroscopy, and SEM are employed to investigate the supramolecular architectures of HP on GO with the intention to understand the nature of the GO~HP interactions under SA treatment. It was found that under SA treatment GO essentially changes the monomer-dimer equilibrium of HP molecules and captures the HP molecules on the flake's surface in the monolayer form with higher luminescence intensity. Finally, stable at neutral pH GO~HP nanocomposite were synthesised. The obtained results validated the concept of using esterification reactions for the formation of GO~HP ensembles that signified the importance of graphene as a nanoscale carrier for new functional materials with advanced properties.

4.2 Synthesis of supramolecular structures using graphene oxide

4.2.1 Graphene oxide functionalisation with doxorubicin

A covalent interaction of GO with anticancer drug doxorubicin (DOX) was investigated. The nano- and microcomposites composed of doxorubicin adsorbed on the surface of GO through covalent and non-covalent interactions such electrostatic and π-π stacking interactions. The formation of such hybrid and three-dimensional structures open the way to create a functional nano- and microcomposite, where graphene oxide plays a role of a non-toxic nanocarrier and of a substance which enhances the anticancer effect.

The functionalisation process of GO with DOX were determined by UV-Vis spectrophotometer, Raman spectroscopy and atomic force microscopy. DOX was covalently attached on carboxylated GO by the covalently linkage of the carboxyl group with the amino group, with heating and ultrasonification for one hour to accelerate the reaction (GO/DOX). The reaction is showed below:

$$R\text{-}COOH + HN(R')_2 \longleftrightarrow R\text{-}COO^- + H_2N^+(R')_2 \xrightarrow{heat} R\text{-}CO\text{-}N(R')_2 \ (4.2)$$
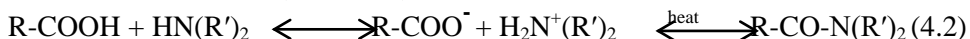
4.2.1.1 UV-Vis and Raman characterisation of GO/DOX

As shown in Fig. 4.26 the doxorubicin (20 μg/ml) has a peak of plasmon absorbance at 488 nm (Huang et al., 2013). While when the concentration of DOX was only 2 μg/ml - no peak was observed, nor in mix with the GO. The UV-Vis spectra of GO show the main peak at 252 nm due to the C=C bond in an aromatic ring, the red-shift of the absorption is due to the deoxygenation reaction, whereas the broad shoulder peak at 302 nm can be assigned to C=O. The absorption over 302 nm is expected to be caused by the conjugated fused ring plane (Zhang et al., 2014). Shaoling Wu (2013) studied absorption properties of doxorubicin onto graphene oxide: equilibrium, kinetic and thermodynamic. The thermodynamic studies indicate that the adsorption of DOX on GO is spontaneous and endothermic in nature.
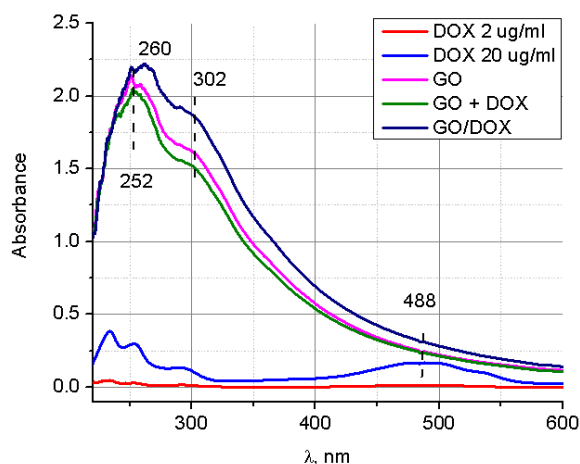
Fig. 4.26. The absorption spectra of GO, DOX, mixed GO+DOX and GO/DOX

When DOX was covalently conjugated on GO, the absorption peak of GO/DOX is shifted to 260 nm. As to the fluorescence spectra (Fig. 4.27), GO and DOX (GO+DOX) mix have the fluorescence peak on 643 nm as free DOX, though the fluorescent intensity diminished due to the quenching effect of GO. These optical results indicated that DOX had been loaded on the GO based nanocarrier as expected (Huang et al., 2013). After the heating and mixing (when DOX was covalently attached to GO) of this solution a bathochromic shift was observed, - the main peak shifted to 647 nm. The fluorescent spectrum results also indicate that a strong π-π stacking interaction exists between GO and DOX (Yang et al., 2008).
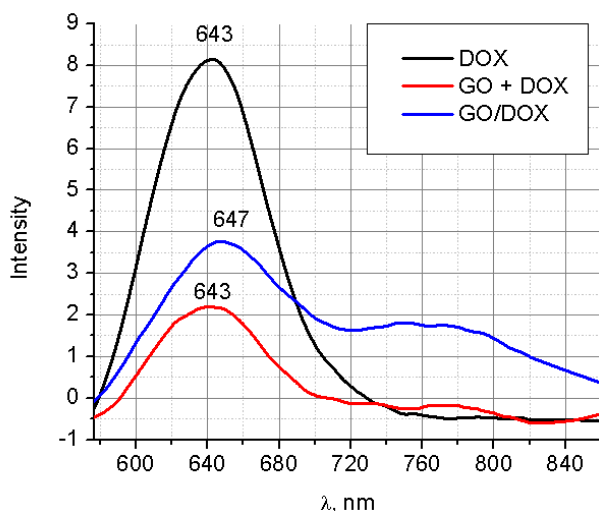
Fig. 4.27. The fluorescence spectra of DOX, mixed GO+DOX and GO/DOX

Graphene oxide has a couple of Raman-active bands on the in-phase vibration of the graphene oxide lattice (G band) as well as the disorder band caused by the graphene oxide edges (D band). The visible decrease in amplitude could be caused

by decreasing the number of free hydroxyl groups after mixing with DOX. The shift to 1,351 cm^{-1} and increasing in amplitude after covalent binding of DOX may be caused by the appearance of different type of groups, the amide linkage and increasing number of defects on graphene oxide lattice. The G band shift from 1,589 to 1,594 cm^{-1} indicates the deformation of ordered structure. The appearance of new peaks, the 1,500 cm^{-1} indicates the stretching vibration of C-N (Hannemann and Seiler, 2009) bond and two peaks 1,737 and 1,786 cm^{-1}, the stretching vibrations of the C=O bond (Fig. 4.28).
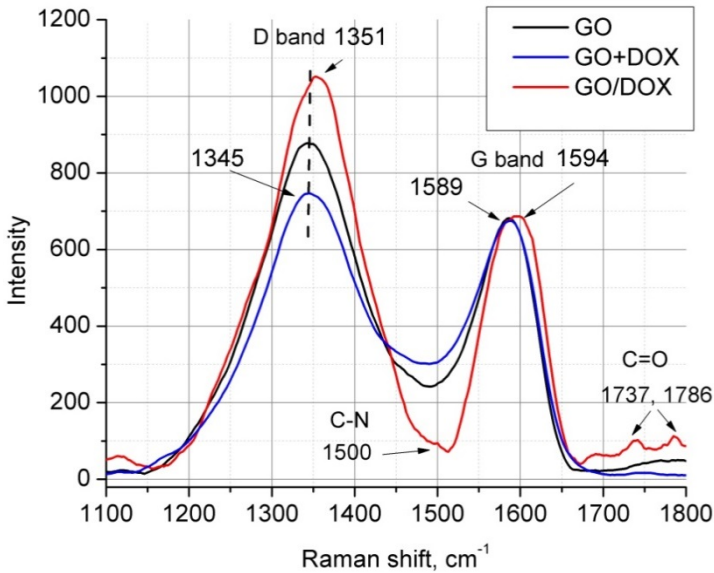
Fig. 4.28. The Raman spectra of GO, mixed GO+DOX and GO/DOX (λ_{ex}- 532 nm)

4.2.1.2   AFM and SEM characterisation of GO/DOX

To clarify the formation of GO/DOX composites AFM and SEM measurements was performed. The AFM picture showed the possible formation of GO/DOX filaments (Fig. 4.29).
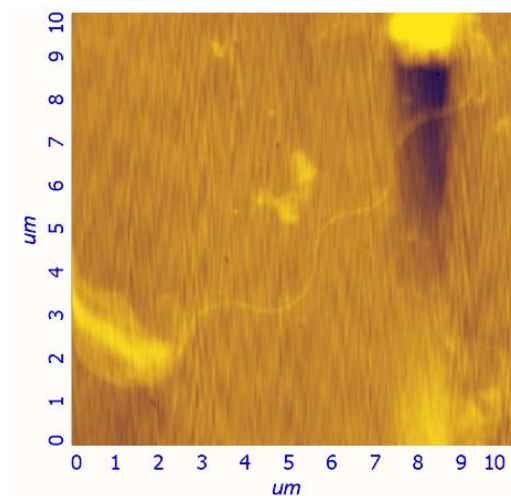
Fig. 4.29. The height picture of GO/DOX aggregate

SEM measurements confirmed the formation of different sizes of filaments. The diameter of big filaments is around 15-20 μm (Fig. 4.30, a) and the middle size filaments are around 5-10 μm (Fig. 4.30, b). The dimensions of the "new-born" are about 1 μm diameter, and 2-3 μm length (Fig. 4.30, c).
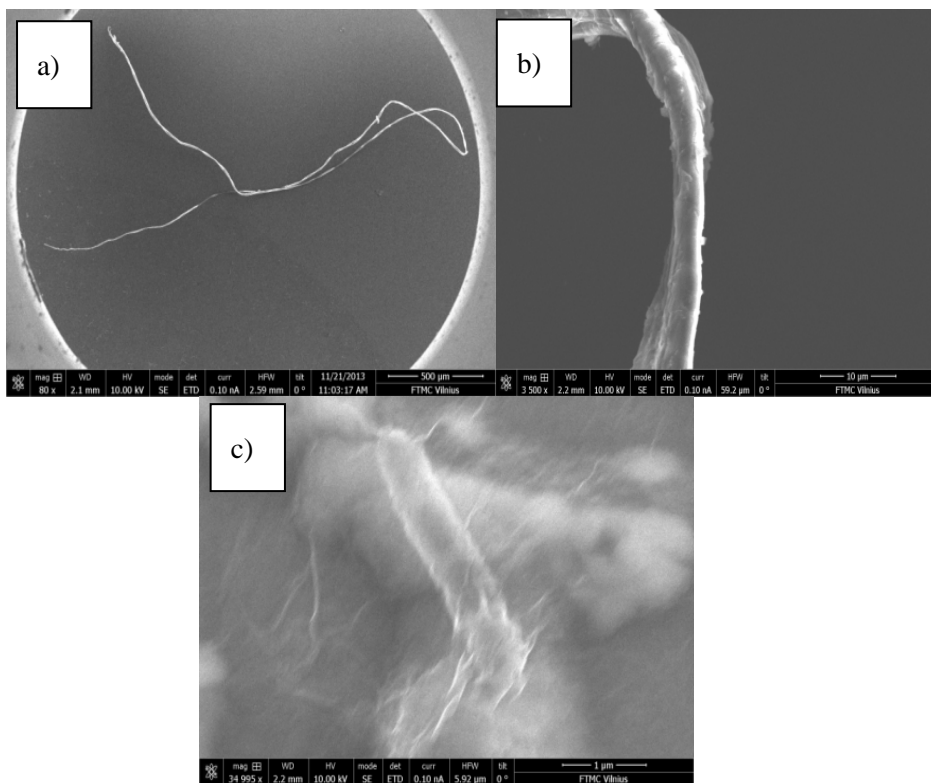
Fig. 4.30. The SEM pictures of different size of GO/DOX filaments

The possible formation of filament forms a mass, consisting of graphene oxide and doxorubicin.
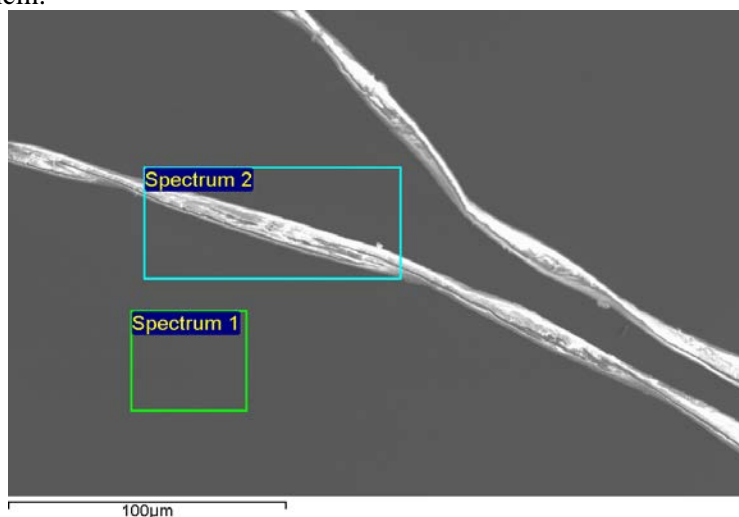
Fig. 4.31. SEM picture of composites based GO and DOX

Spectrum 1 proves the Si surface, accordingly spectrum 2 proves that the filaments were based mainly from doxorubicin (according to the Brutto formula DOX- $C_{27}H_{29}NO_{11}$), but some mismatches with amounts of oxygen (8.41 instead of 15.51) and carbon (34.92 instead of 38.07) show that another material, graphene oxide, had an influence in this formation (Fig. 4.31, Table 4.4).

Table 4.4. EDX analysis of composites based on GO and DOX

Results in atomic%	C	N	O	Si	S
Spectrum 1	5.01	0.45	1.21	93.13	0.19
Spectrum 2	34.92	1.41	8.41	55.27	0.01

4.2.1.3 Conclusion

It was found that advanced macromolecules using graphene-based material, graphene oxide and anticancer drug- doxorubicin could be formed. The obtained results validated the concept of using covalent linkage of the carboxyl group from GO with the amino group from doxorubicin. The GO/DOX mixture led to the reduction of the DOX concentration in drugs with the purpose of reducing the undesirable side-effects and could be used as a drug-drug delivery system for healing tumours and future theranostics.

4.2.2 Graphene oxide functionalisation with cationic mesa-tetra(4-pyridyl) porphine

Cationic GO/TPyP hybrid structures have been synthesised by ionic self-assembly. The different aggregated structure shape was obtained through electrostatic and π-π stacking interactions. The investigation revealed a three-dimensional fibre structures formation under acid conditions and leaf-like structures of the GO/TPyP assemblies under alkaline conditions of the solution. This new synthesised macromolecule based on graphene shows a potential use for tissue engineering applications.

4.2.2.1 UV-Vis characterisation of GO-TPyP aggregates

As shown in Fig. 4.32, the ground state absorption spectrum of TPyP exhibited a very intense Soret band (Q_{max} - 419 nm) corresponding to the S2 transition, while the weaker Q bands between 500 and 600 were assigned to a pair of vibronic progressions corresponding to S1 transition (Khenfouch et al., 2014). After adding GO and changing the pH level to pH 5.4 the position, width and intensity of the absorption spectra of GO/TPyP solution were changed. The most obvious change occurred in the Soret band region of the absorption spectrum: the intensity of the original Soret band at 419 nm decreased gradually and a new Soret band appeared at 442 nm. This red shift indicates that interactions took place between GO and TPyP. The results indicate that the functional groups on the surface and edge of graphene sheets played an important role in interactions between various molecules through supermolecular interactions such as π-π stacking, electrostatic interaction and hydrogen bonding (Fagadar-Cosma et al., 2009). The similar results have been demonstrated (Kaplan, Korin and Bettelheim, 2014) in the pH range 6-13.
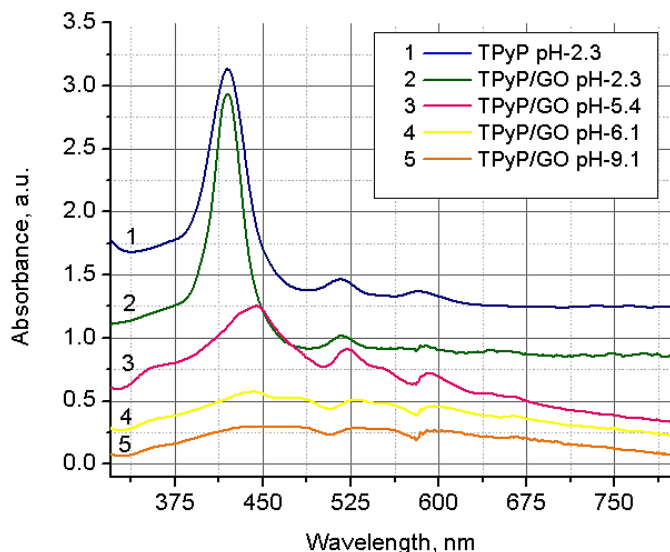
Fig. 4.32. Absorption spectra of TPyP and TPyP with GO in different pH levels

Since TPyP is positively charged owing to the presence of pyridyl groups, the GO sheets have negative ζ-potentials in both deionised water and ionic salt solutions. The oxygen amount in the GO (hydroxyl (-OH), carboxyl groups (-COOH), epoxy (C-O-C) groups) affects the surface charge and its dispersion in aqueous solutions. Although ζ-potential plays a key role in colloidal stability, it does not show the true particulate state in various environments. The GO dispersion showed an excellent colloidal stability in deionised water even after 24 h at room temperature. This is because of their high negative surface charge (electrostatic stabilisation). However, in the presence of TPyP, GO formed observable aggregates and came completely out of suspension after 1 hour incubation at room temperature. Hydrophobic and π-π interactions acted as the driving forces to promote GO self-organisation process, which was highly enhanced by ionic self-assembly with oppositely charged TPyP. The influence of pH on GO/TPyP composites aggregation was also studied by optical microscopy in the pH range 1.5–9.1 (Fig. 4.33).
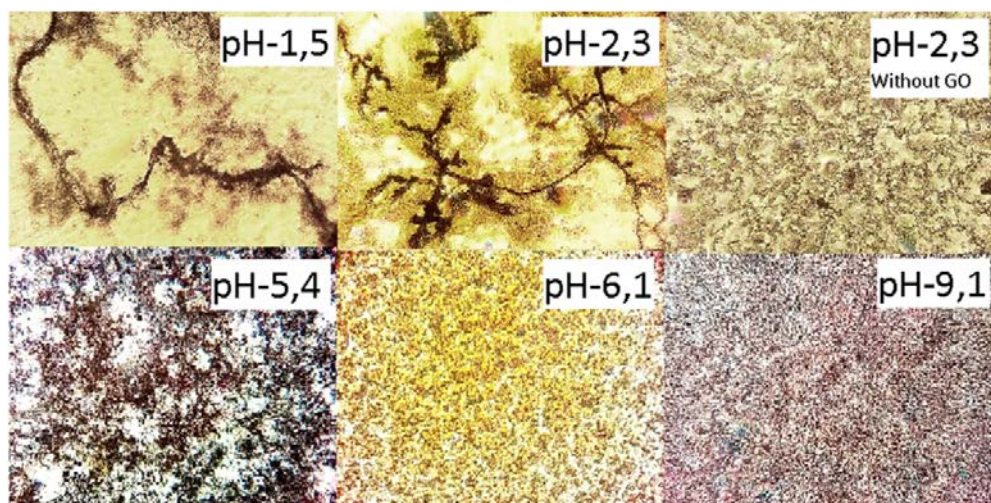
Fig. 4.33. Aggregation of pH-depended GO/TPyP products formed during 10 min on the glass surface (optical microscopy images (125x) of the drop casted GO/TPyP or TPyP solution)

After adding GO dispersion into TPyP solution, fluorescence quenching was also noticed with the increase in graphene concentration. The fluorescence quenching effect could be ascribed to the porphyrin/graphene interactions enlarging the conjugation of the porphyrin system, which is an efficient electron or energy transfer from the excited state of the cationic porphyrins to graphene and the occurrence of photo-induced electron transfer between the aromatic molecules and graphene.

4.2.2.2   SEM and AFM characterisation of GO/TPyP aggregates

The investigation of a dried solution drop by SEM revealed the formation of the mixture of GO/TPyP disordered aggregates and nanofibre network. The size and density of the nanofibres vary depending on the time, concentration of TPyP, GO and pH of the solution. The formation rate of nanofibres is growing with the increase of GO concentration. Investigation of the pH influence on the formation of fibre like structures have shown that the fibre like structure formation process occurred in the acid solutions, and a low pH solution produces a high density fibre network. The high pH solution produces the complex, branched structures of GO/TPyP aggregates. The AFM measurements have shown that the size of nanofibres is growing in time and fibres from a tenth of a nm to hundreds of nanometres in diameter were produced over 2 hours (Fig. 4.34).
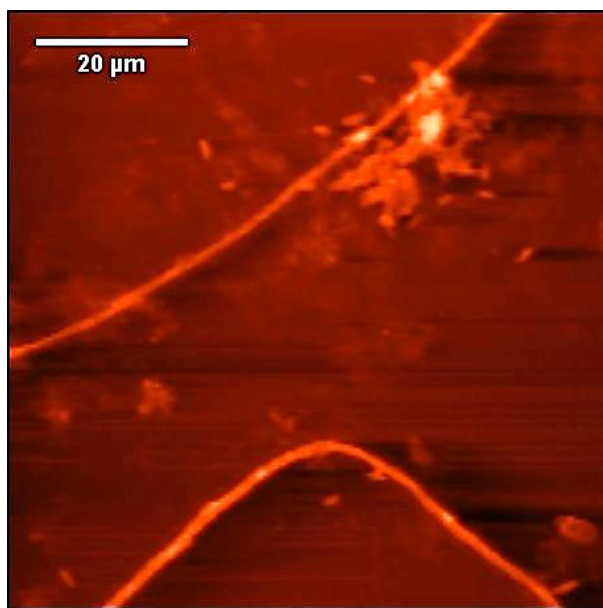
Fig. 4.34. AFM image of GO/TPyP hybrid aggregates

The SEM of GO has shown a typical crumpled and wrinkled structure. The surface became rough and the rod-like structures appeared after the formation of GO/TPyP aggregates (Fig. 4.35, a). To investigate the profile of the fibres, the focused ion beam (FIB) was used to cut the fibres during the SEM measurement. The SEM images of the fibre cross-section demonstrate that the fibres are solid flattened structures with a width up to 900 nm and the height up to 500 nm (Fig. 4.35, b and c).
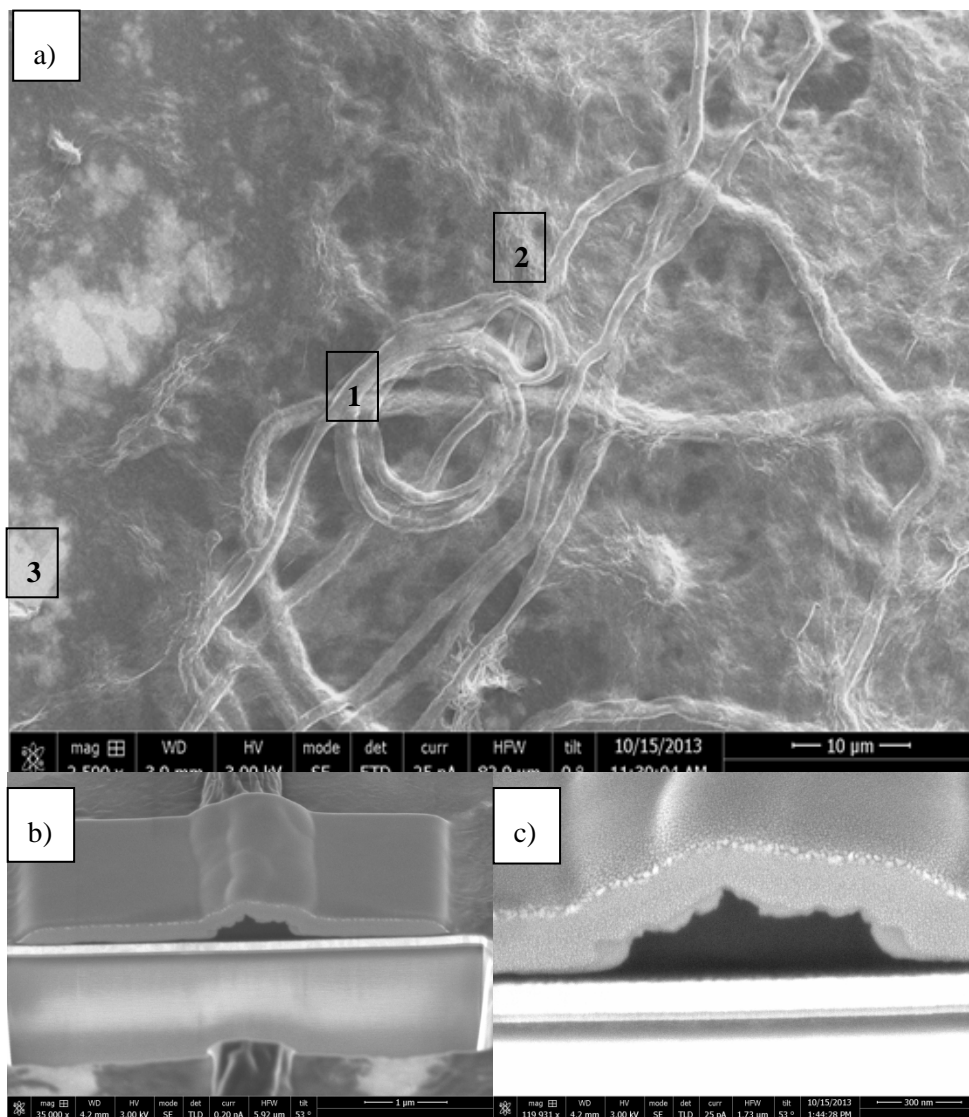
Fig. 4.35. SEM images of GO/TPyP hybrid aggregates: a) network of GO/TPyP fibres, b) and c) FIB made cross section of the fibre

EDX analysis was used to investigate the elemental composition of the nanofibres. The chemical element analysis on the fibres and the sheet-like aggregates outside a fibre area have shown that the fibre consist mainly of carbon (70.81%), nitrogen (17.58%) and oxygen. Smaller amounts of nitrogen (5.89%) with carbon and oxygen were detected near the nanofibres on the graphene oxide flakes (Table 4.5). This can be explained by the increased porphyrin role in the fibres formation. The nitrogen detected on the nanofibres indicates the presence of the TPyP and it confirms the suggested ionic mechanism of the hybrid aggregates formation.

Table 4.5. EDX analysis of composites based on GO and TPyP

Results in atomic %	C	N	O
Spectrum 1 (on fibre)	70.81	17.58	11.61
Spectrum 2 (near fibre, on aggregates)	76.56	7.24	16.2
Spectrum 2 (on the GO flake)	79.53	5.89	14.58

4.2.2.3 Raman spectroscopy characterisation of GO/TPyP aggregates

The Raman spectra of nanoaggregates and nanofibres are shown in Fig. 4.36. The GO/TPyP nanoaggregate Raman spectra D band around 1,340 cm^{-1} and G band around 1,592 cm^{-1} are the characteristic of graphene oxide. The similar results have shown Raman spectra of the nanofibre, with 1,349 cm^{-1} and 1,596 cm^{-1} bands shift. The bands 993 cm^{-1}, 1,428 cm^{-1}, 1,446 cm^{-1} and 1,547 cm^{-1} corresponds to TPyP, indicating that TPyP has bound to graphene. The larger D/G bands intensity for nanofibre structure suggests that more graphitic domains are formed and the sp^2 cluster number is increased (Ferrari, Robertson, 2000).
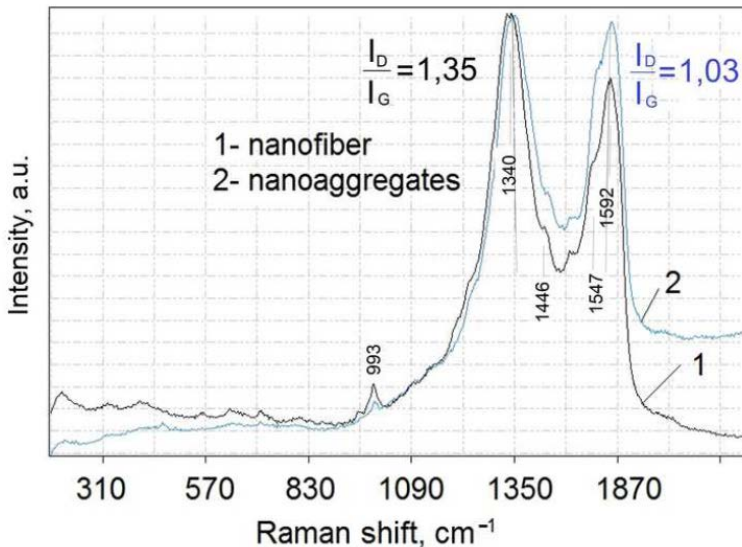
Fig. 4.36. Raman spectra of GO/TPyP nanofibre and nanoaggregate (λ_{ex}- 532 nm)

4.2.2.4 Current-voltage characteristics of the aggregates

The dependence of the conductivity on the electric field and the GO thickness provides information on electric transport perpendicular to the sheets of GO/TPyP structures. The local current-voltage characteristics were measured by setting the AFM cantilever at different positions on the GO/TPyP sheets and nanofibres.

Current-voltage characteristics of GO/TPyP layers have shown current fluctuations, probably, because the current is sensitive to contact force. The experiments have shown that in the case of thin GO/TPyP sheets (Fig 4.37, a) conductivity is higher and fits the Poole-Frenkel model, and in the case of nanofibres, consisting of many GO layers and therefore a low electric field between a layers, the Schottky emission mechanism takes place (Fig 4.37, b). The conduction mechanism is ascribed to the Schottky emission mechanism (at low electric fields) or Poole-Frenkel emission mechanism (at high electric fields) (Chang, Lin, 2001). It was shown that the conductivity of synthesised nanofibres can be increased by GO sheets reduction.
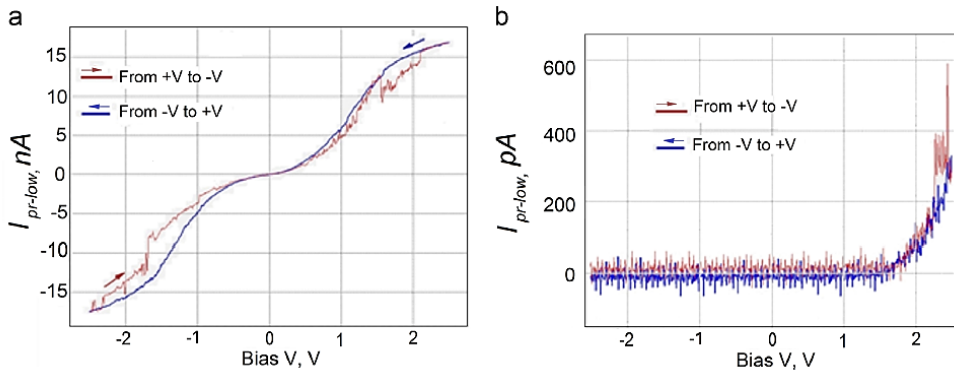
Fig 4.37. Current-voltage characteristic of GO/TPyP aggregates: a) GO sheets functionalised with TPyP molecules and b) synthesised GO/TPyP nanofibres

4.2.2.5 Conclusions

In summary, hybrid GO/TPyP nanofibre-type structures were synthesised. The characterisation of the obtained structures has shown the fibres can vary in diameter from tens to hundreds of nanometres and produce a network like structure. The UV-Vis, EDX and Raman scattering spectra investigations confirm the formation of TPyP and GO hybrids.

4.3 Nanoparticles interaction with lipid membranes, as a model for graphene-based materials interaction with bio-membranes

4.3.1 Formation and characterisation of lipid membranes

4.3.1.1 Formation of bilayer lipid membrane

The formation of bilayer lipid membranes (BLMs) was performed according to the procedure described in 3.2.7. The formation of BLM was monitored and estimated using different techniques; optical microscopy, SAF and AFM. Monitoring lipid solutions in PBS buffer the formation of vesicles was noticed (Fig. 4.38). It confirms that the formation of lipid membrane was preceded by the lipid vesicle fusion method.
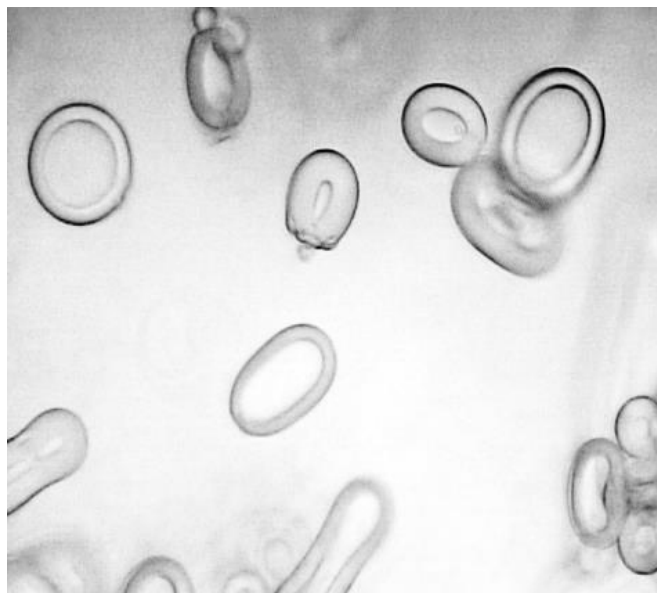
Fig. 4.38. Optical picture of lipid vesicles in PBS buffer

Lipid monitoring by AFM and SAF was performed for one hour in the same place. During this time the whole formation from the first vesicles attached to the surface until the formation of a homogeneous membrane was recorded (Fig. 4.39).
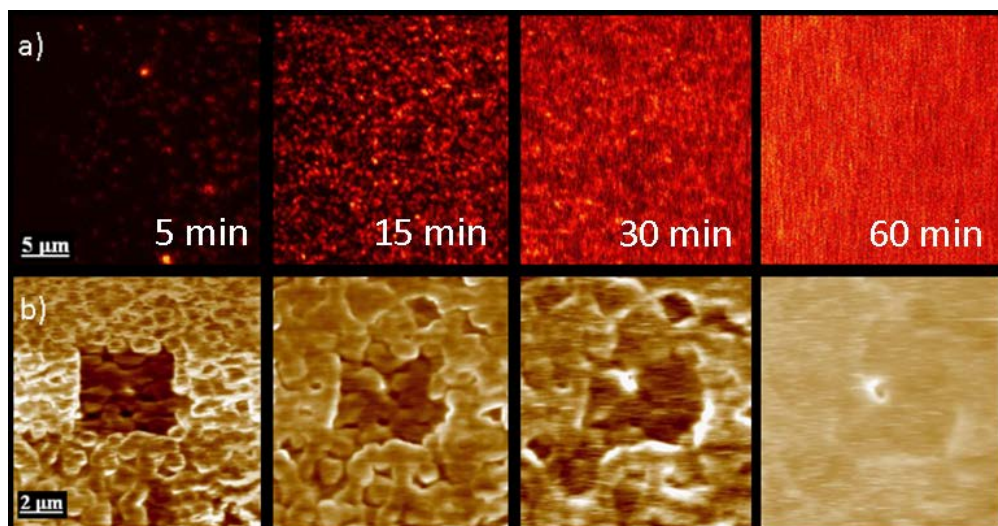
Fig. 4.39. The formation of lipid membrane by a) SAF and b) AFM

4.3.1.2 BLM characterisation with AFM and SAF

Lipid membrane measurements were performed in a water environment to ensure the natural conditions for lipids. The roughness of the membrane significantly influences the capacity and optical parameters of BLM. Therefore, the study of these characteristics provides information on the bilayer structure (Hianik and Passechnik, 1995). The lipid membrane surface roughness is influenced by the vertical lipid motion. Stable rough membranes are less funnel-like and more structured (Schneider, 1996). Membrane surface roughness, homogeneity and lipid dynamics are used to determine the quality of a BLM. Therefore, AFM was used for lipid membrane roughness measurements. The characterisation of BLM was performed on a glass surface. The surface roughness was measured with AFM (Fig. 4.40). The roughness of the glass surface, on which the lipid membrane was formed, as measured, was in the range ~5-8 nm. The AFM cross-section was used to estimate the roughness of the membrane. The roughness of lipid membrane was found to be ~ 2-4 nm. It was previously shown that stable membrane roughness could have a range of 0.5-5 nm (Schneider, 1996). Also, the fractal dimension of lipid membrane was measured - D-2.7. A fractal dimension is an index for characterising fractal patterns or sets by quantifying their complexity. A surface with fractal dimension of 2.7 fills the space orderly rather like a volume.
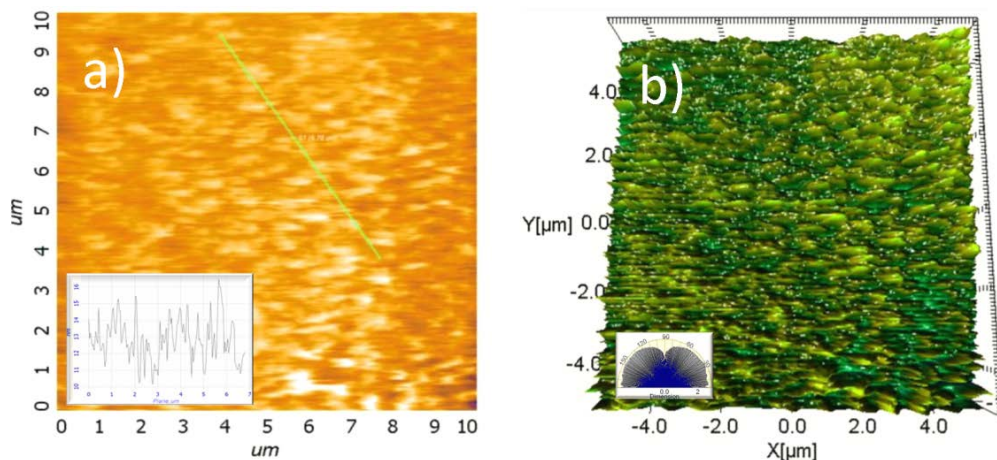
Fig. 4.40. a) 2D and b) 3D AFM images of lipid membrane surface. In the insert: a) cross section of lipid membrane surface, whereas in b) fractal dimension (D-2.7) of lipid membrane picture

Images of fluorescently labelled lipid membranes were recorded with a custom-made scanning microscope allowing the detection of fluorescence and the supercritical angle fluorescence (SAF) images of an emitter simultaneously. The SAF channel detects only fluorophores in close proximity to the surface ($\sim$100−200 nm) and efficiently rejects the fluorescence from the bulk solution using parabolic lenses as the decisive optical element. All measurements were conducted by passing buffered solutions of NP's over the lipid membrane through the flow cell at a constant pump rate of 250 μl/min (0.42 mm/s).

SAF measurements were used to estimate BLM deposition on the surface and homogeneity of BLM. FCS measurements were used (Fig. 4.41) to investigate the lipids diffusion in the membrane. The BLM investigation was performed with SAF microscopy combined with the FCS as a sensitive and efficient method to study the labelled lipids. As it is seen in SAF images, a homogeneous and non-damaged lipid membrane was formed.
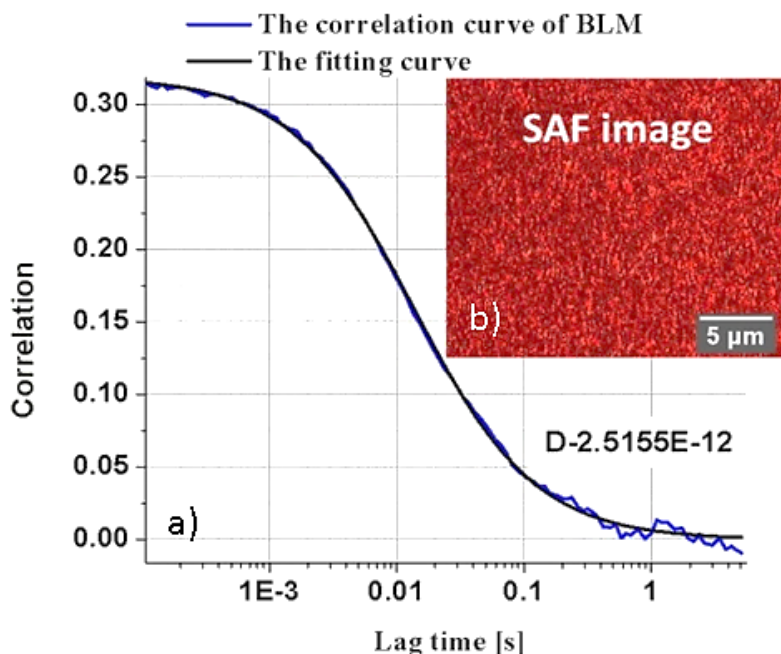
Fig. 4.41. a) The correlation curve of BLM and the diffusion coefficient determined by fluorescence correlation spectroscopy (the solid grey line represents the fitting curve for the corresponding curve) b) 2D image of lipid membrane fluorescence

Diffusion coefficient value (D) of a stable, non-damaged lipid membrane formed from DOPC: DOPS phospholipids should be in the range of 2-4 E-12 $m^2 s^{-1}$ (Štefl, Kułakowska and Hof, 2009). The obtained diffusion coefficient of mixed bilayer LMs synthesised using DOPS:DOPC lipids are 2.5155 E-12 $m^2 s^{-1}$.

4.3.1.3 BLM characterisation with Raman spectroscopy

LM was formed on optically active surfaces based on Ag or Au nanostructured film deposited by chemical reduction using HF etched silicon (the preparation of SERS substrates is described in section 3.2.9).

The scheme of lipid membrane (LM) formation on different types of SERS surfaces (unmodified Au SERS, modified Au SERS with 1-dodecanethiol and unmodified Ag SERS) is presented in Fig. 4.42
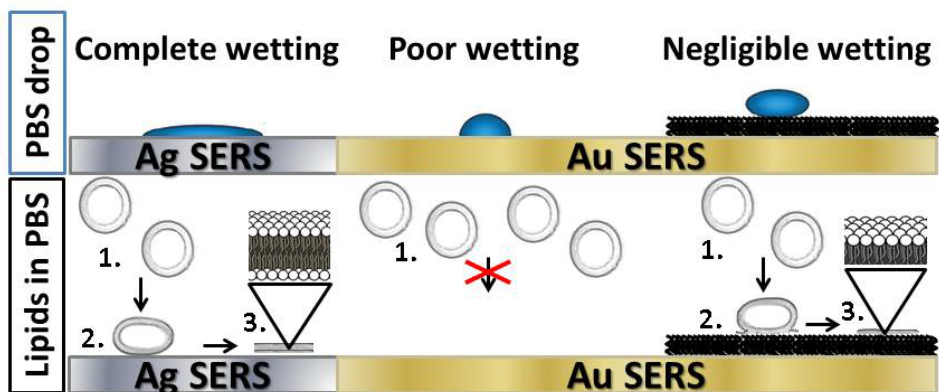
Fig. 4.42. The scheme of lipid membrane formation on different types of SERS surfaces: and unmodified Ag SERS, unmodified Au SERS and modified Au SERS with 1-dodecanethiol layer, respectively

A mixed DOPC:DOPS lipid membrane deposited on Au and Ag SERS substrates in PBS solution was investigated using Raman spectroscopy to investigate the interaction of LMs with surfaces. No Raman peaks were obtained in the cases when LMs are formed on blank silicon (data not shown) and on the unmodified Au SERS substrate (Fig. 4.43, line 3). The absence of Raman peaks of the LMs deposited on Si can be explained by the low sensitivity of Raman spectroscopy at the nanoscale. The same phenomenon is observed in Raman spectra of LMs deposited on the Au SERS substrate. However, in this case the LM was probably unable to compose on the surface because of the poor wetting of the surface (Cha, Guo and Zhu, 2006). In order to deposit LM on gold surfaces the intermediate molecules should be used to create self-assembled monolayers (SAMs) (McGillivray et al., 2007). Due to the selected SAMs, a bilayer LM or monolayer LM can be obtained (Marques et al., 2014).

The lipid membrane formed onto modified Au SERS (Fig. 4.43, 4 line) shows peaks of high intensity in both 2,840-3,040 cm^{-1} and fingerprint (<1,800 cm^{-1}) regions, such as 997 cm^{-1} (O-P-O), 1,307 cm^{-1} (CH$_2$ twist), 1,445 cm^{-1} (CH$_2$ bend), 1,608 cm^{-1}, 1,672 cm^{-1} (*cis* C=C stretching vibrations) (Gunstone, Harwood and Dijkstra, 2007). The Au SERS enhancement of the methyl deformation (lipid tail group, 1,307 cm^{-1}) and no peak aligned with the carbonyl group stretch (lipid head group, C=O, around 1,700 cm^{-1}) could be explained by the tail group being closer to the Au SERS surface than the head group. The Raman spectra of the used binding layer (1-dodecanethiol) on the silicon surface are presented for comparison (Fig. 4.43, 2 line). Finally, the presence of the phospholipid monolayers and bilayers can be observed in the 2,750-3,050 cm^{-1} regions. In particular, the presence of an intense band at 2,960 cm^{-1} (assigned to the asymmetrical stretching vibration of the methyl groups) is intense in the case of phospholipid bilayers (Saint-Pierre Chazalet et al., 1994).
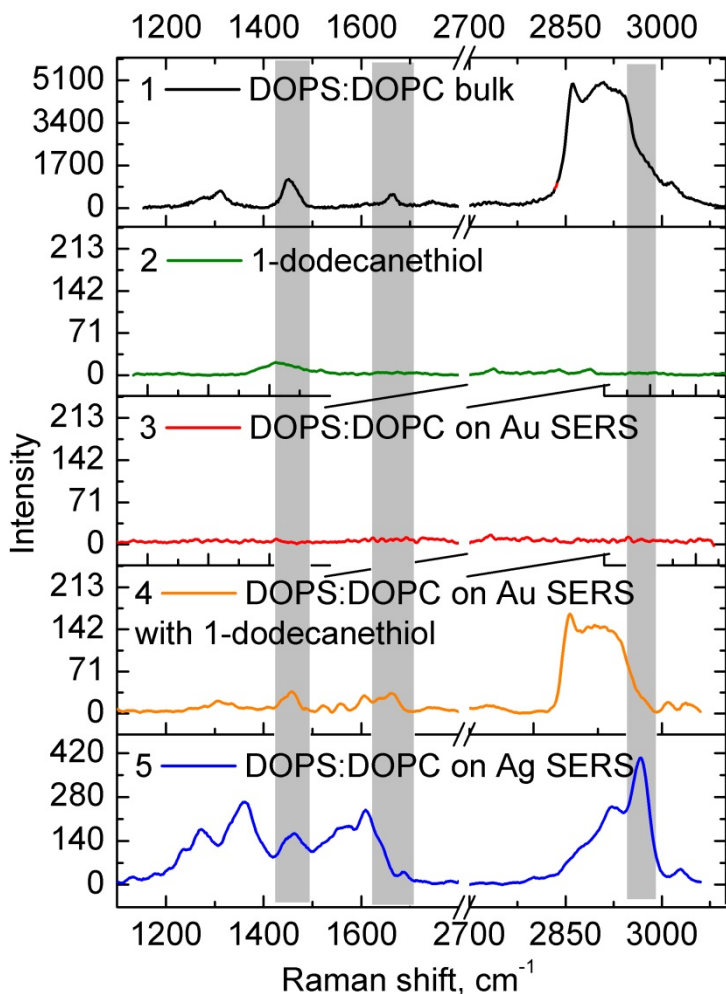
Fig. 4.43. Raman spectra of LMs on different SERS substrates in PBS solution (λ_{ex}- 532 nm)

However, the bilayer LM bands in the Ag SERS spectrum are clearly enhanced and, compared to the spectrum of the LMs on Au SERS substrate and DOPS:DOPC bulk measurements, changed in shape. In general, Ag nanoparticles could interact with cell membranes by first binding at the membrane-water interface. Interfacial interactions are based on surface structure and membrane lipid composition. A nanoparticle from the surface can interact with the membrane and disrupt the lipid organisation and membrane structure (Nel et al., 2009). Considering that the interaction of LM with a nanostructured silver surface can occur through coordination complexes formed between nanoparticles and active functional head groups such as phosphate PO_3^- or COO-, we hypothesised that a bilayer LM with SERS substrate interacts through both groups. The COO- bond region in SERS spectra, suggesting the possible interaction of lipid molecules with Ag, is located at

1,312-1,424 cm^{-1}. Raman scattering of PO_3^- have several typical peaks at 1,138 cm^{-1}, 1,001 cm^{-1} and 710 cm^{-1} (Novita, Boolchand, 2007) (Fig. 4.43, 5 line). In this case, lipid molecules probably interact with Ag NPs through coordination complexes. The lipid membrane formed onto modified Ag SERS also shows high intensity of peaks in both: 2,840-3,040 cm^{-1} and fingerprint (<1,800 cm^{-1}) regions. It is important to note that the shifted peaks can be the result of lipid interactions with the nanostructured silver surface. The assignment of Raman bands for phospholipids is shown in Table 4.6.

Table 4.6. Assignment of Raman bands of phospholipids (Gunstone, 2007)

Raman band position, cm^{-1}	Assignment
800-920	C-C stretching
945-970	C=C in-plane bending
1,060-1,136	C-C stretching
1,250-1,280	=C-H bending
1,295-1,305	C-H twisting deformations
1,400-1,500	C-H scissoring deformations
1,640-1,680	C=C stretching
1,730-1,750	C=O stretching
2,700-3,015	C-H stretching

As it is seen in Fig. 4.43 the peaks of LM obtained on the Ag SERS substrate are of higher intensity in comparison with Au SERS. The difference of spectra recorded on various SERS substrates is thought to be due to the bilayer LM having double the thickness of the monolayer and a different sample preparation method (McClements, 2014). During the preparation procedure, the lipids are deposited directly on the Ag SERS surface. Therefore, some parts of the lipids can interact with Ag NPs and be selectively enhanced. According to that, the Au SERS substrate was modified with a binding layer of 1-dodecanethiol, and the lipids had no direct contact with Au NPs. For this reason, the intensity of the peaks was found to be significantly lower in comparison with Ag SERS.

4.3.2 The interaction of nanoparticles with bilayer lipid membranes

Nanoparticles (NP) are broadly exploited in biomedical sciences in order to develop various methods of targeted drug delivery, novel biosensors and new therapeutic pathways. However, relatively little is known in the negotiation of NPs

with complex biological environments. NP interactions with cell membranes can damage the cell membrane and cause toxicity; therefore, examining interactions between NPs and cell membranes is crucial to understanding NP toxicity mechanisms and the development of safe and non-toxic NP-based commercial and therapeutic applications. To gain a physical understanding of NP-membrane interactions, a simplified system built of well-defined synthetic lipid bilayers and NP was used. The interaction of nanoparticles with bilayer lipid membranes can lead to structural modifications of the BLM and affect the structure and dynamic of lipids.

4.3.2.1   BLM interactions with GO nanoparticles

In this section the interaction of the lipid membrane with GO was analysed using SAF spectroscopy, confocal microscopy and Raman spectroscopy.

Initially, the GO flakes were measured on SAF without the lipid membrane. It was noticed that GO is a fluorescent, non-dynamic material (see Fig. 4.44) and it could be easily detected on the membrane because of this characteristic. GO fluorescence is more noticeable on the undercritical angle fluorescence (UAF) channel, so this is also a good way to separate BLM fluorescence form GO fluorescence.
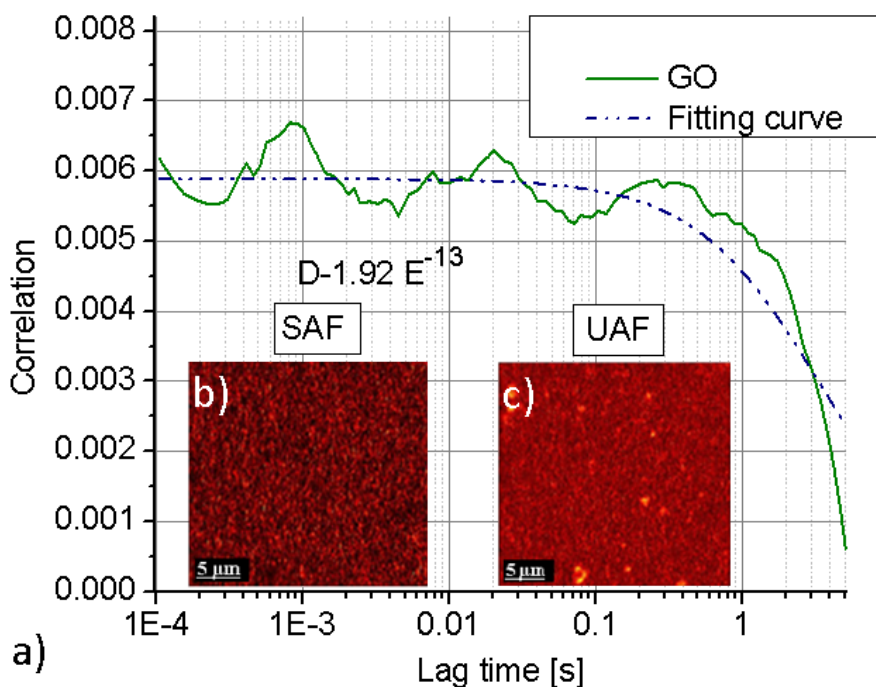
Fig. 4.44. a) The correlation curves of GO and the diffusion coefficient determined by FCS b) SAF 2D image of GO flake fluorescence c) UAF 2D image of GO flake fluorescence

To confirm NP's aggregate attachment to the BLM surface, FCS measurements were used indicating the impact of NP's on the lipid diffusion in the

BLM. The lipid membrane diffusion noticeably decreased in the place where GO flakes are attached to the surface (D is in the range 5-7 E-13 $m^2 s^{-1}$).

As shown in Fig. 4.45, the fluorescence intensities of BLM after 16 hours of exposure to a suspension of GO were recorded. The increased fluorescence intensity of the membrane with GO (0.05 g/ml) reflects on the possible GO flakes deposition on BLM. From Fig. 4.45 it is seen that diffusion curves and coefficients (D, from FCS measurements) indicating the difference in the presence (blue line, when measured near visible GO flake and red line, when measured directly on the GO flake) and the absence (D- 2.57 E-12 $m^2 s^{-1}$, typical diffusion coefficient for pure lipid membrane; black line) of GO. The dotted lines represent the fitting curves for corresponding FCS curves. The significant reduction of D can be explained as a result of lipid-GO flakes binding.
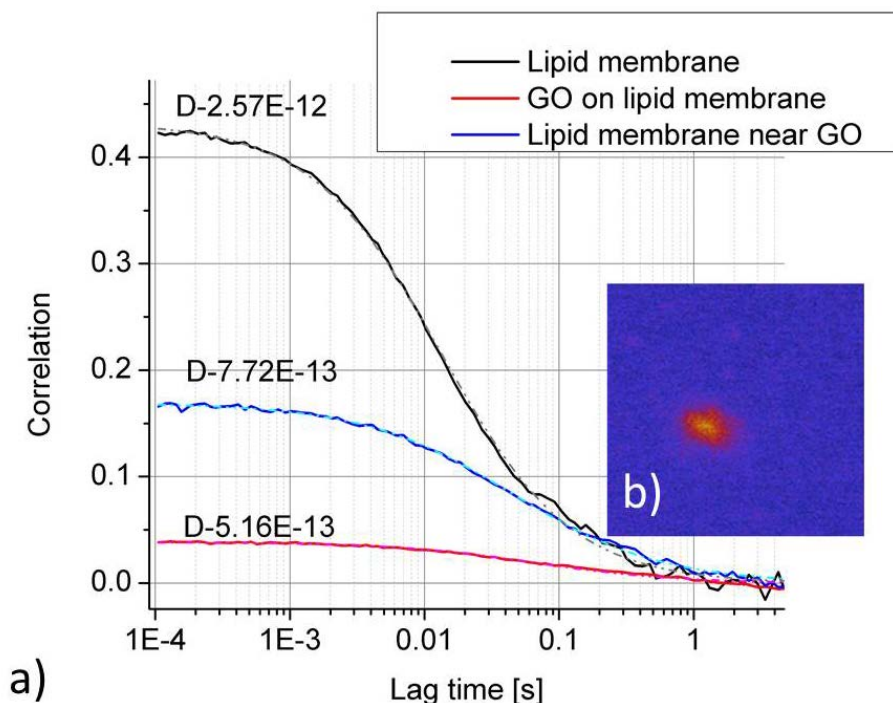
Fig. 4.45. a) The correlation curves of BLM and BLM with GO in different places and the diffusion coefficients determined by fluorescence correlation spectroscopy b) 2D image of lipid membrane and GO nanoparticle fluorescence

The possible model of GO flake-lipid membrane interaction is proposed in Fig. 4.46. It is in line with other studies, where it is explained that the GO flake is cutting the lipid membrane and part of the graphene oxide flake could be not visible in UAF or confocal pictures, but it could be detected by Raman spectroscopy (Fig. 4.46) and after measuring lipid diffusion changes near the visible GO flake (Fig. 4.45, red line).
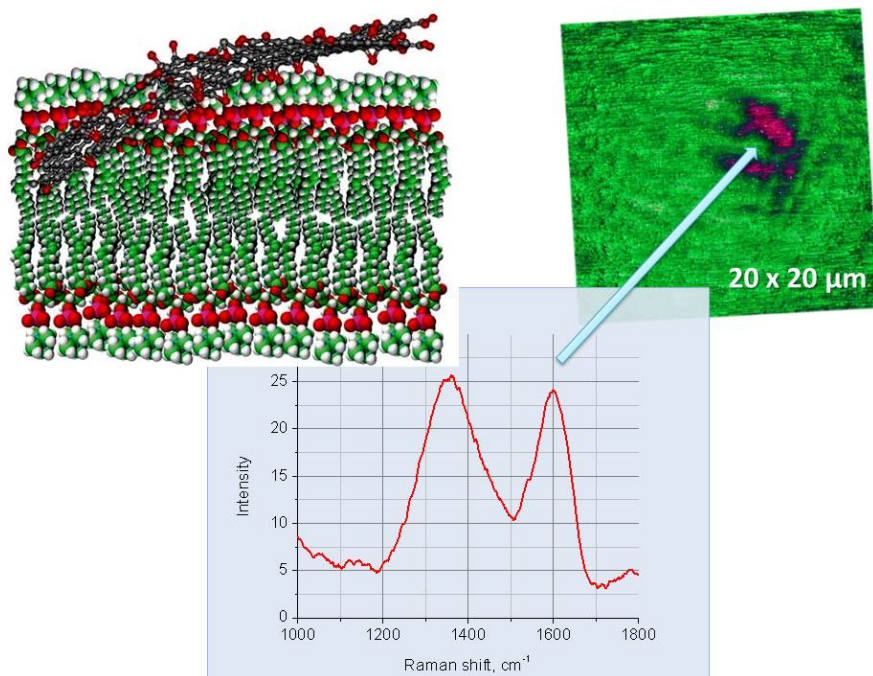
Fig. 4.46. The proposed model of how graphene oxide gets into the membrane

4.3.2.2 BLM interaction with other nanoparticles: TiO₂ and ZnO

TiO$_2$ and ZnO nanoparticles were chosen because of their wide applications and usage in the paper, ink, medicine, food products, cosmetics, toothpaste and skin care product industries, among others. Therefore, a better understanding of the interactions between NP and the lipid membrane may help to clarify the potential risk of NPs.

AFM and TEM were used to determine the size of NPs. The grain analysis function was used and then the distribution of NP size was built. It gives the size of ZnO as 20.2 nm (standard deviation (SD)-9.47 nm) and TiO$_2$ gave the size value of 35.3 nm (SD-9.20 nm) (Fig. 4.47). Also, zeta potential measurements were performed. The magnitude of the zeta potential indicates the degree of electrostatic repulsion between adjacent, similarly charged particles in dispersion. ZnO zeta potential variation with pH 7-8.5, dispersions are stable and positively charged (with pH 7.4 ~ +3 mV). It is known that low zeta potentials tend ZnO suspension to coagulate or flocculate. In TiO$_2$ zeta potential variation with pH 5-9, dispersions are stable and the surface is positive (with pH 7.4 ~33 mV). In this case, a high zeta potential will confer TiO$_2$ stability, i.e., the suspension resists aggregation.
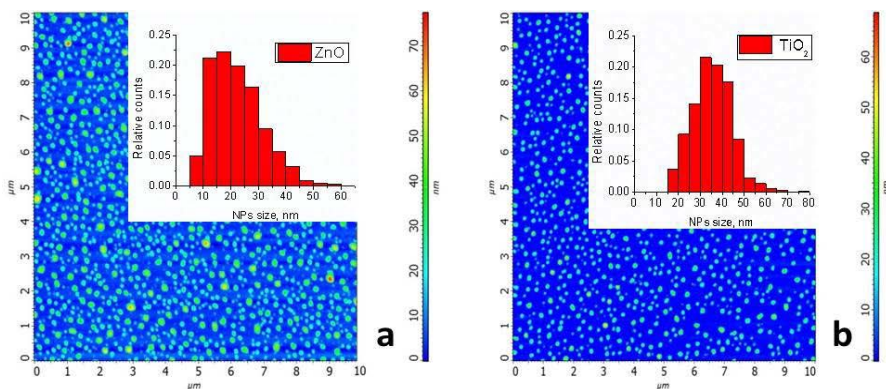
Fig. 4.47. AFM images of a) ZnO and b) TiO$_2$ nanoparticles, respectively

The BLM contained one part of negatively charged phospholipids (DOPS) and the other part of neutral phospholipids (DOPC) because the chosen ratio is similar to the composition of the inner leaflet of neuronal membranes, which is typically enriched with negatively charged phospholipids in the range of 15-30 mol%. Generally, the interaction of nanoparticles with hydrophilic interfaces requires negative surface charges implying a strong contribution of electrostatic forces during the adsorption event. As shown in Fig. 4.48, the fluorescence intensities of BLM after 16 hours of exposure to a suspension of ZnO or TiO$_2$ were recorded. The reduced fluorescence intensity of the membrane with ZnO (2.5 mg/ml) reflects on the possible ZnO aggregates deposition on BLM. The measured zeta potential of ZnO suspension shows the high probability of aggregates formation, which could quench the fluorescence intensity. The possible explanation of why we obtained differences with different NPs is because the various (from 3 to 33 mV) zeta potentials lead to stability of suspension (TiO$_2$ case) or big aggregate attraction to the lipid bilayer (ZnO case).
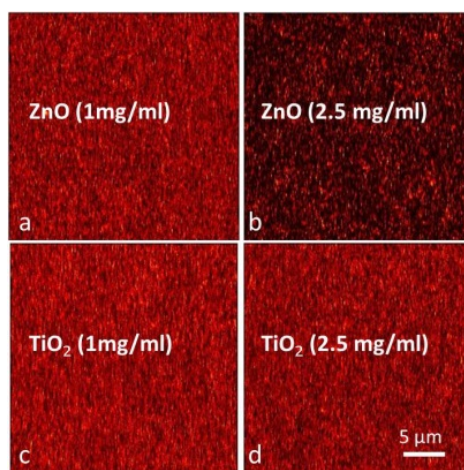
Fig. 4.48. SAF images of the scanned areas acquired after 16 hours of exposure to a suspension of ZnO or TiO$_2$ with different concentrations on the lipid membrane bilayer demonstrating ZnO and TiO$_2$ interaction with the lipid membrane

100

To confirm NP's aggregate attachment to the BLM surface, FCS measurements were performed (Fig. 4.49) indicating the impact of NPs on the lipids diffusion in the supported lipid bilayer at different concentrations. To investigate the ZnO and TiO_2 NP's interaction and aggregation with supported lipid bilayers at different concentrations we employed SAF microscopy combined with the fluorescent correlation spectroscopy (FCS) as a sensitive and efficient method to study the interaction of nanoparticles with supported lipid bilayers under continuous and constant flow conditions.

The influence of the addition of the ZnO or TiO_2 NPs to the lipids suspension and the NP's effect on the supported lipid membranes was studied by analysing the FCS measurements of the labelled DOPE lipids contained inside membranes before and after the addition of nanoparticles. Fig. 4.49 illustrates three independent measurements of the diffusion coefficient without the addition of nanoparticles and after the addition 1 mg/ml and 2.5 mg/ml ZnO or TiO_2 concentration, respectively. Both NPs show slight variations (diffusion coefficient (D) is in the range of 2-3 E-12 m^2 s^{-1}) in the diffusion coefficient values, with no defined trend. FCS measurements reveal that the significant reduction of D (D- 4.91 E-13 m^2 s^{-1}) occurs only after the addition of 2.5 mg/ml ZnO; other samples remained quite stable for a longer period of time. The effect could be due to the unstable suspension caused aggregations connections to the BLM surface.
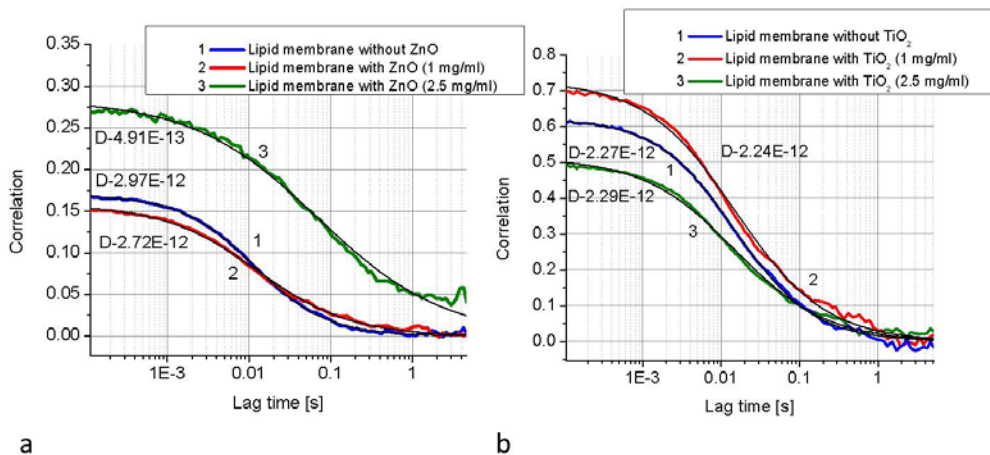
Fig. 4.49. Fluorescence intensities of lipid membrane with and without a) ZnO or with b) TiO_2. Diffusion curves (from FCS measurements) indicating the difference in the presence and absence of 2.5 mg/ml ZnO (the solid black lines represent the fitting curves for corresponding FCS curves)

The lipid-ZnO aggregates binding effect is enlarged with the increasing ZnO concentration. The higher ZnO concentration leads to the enhancement of the D reduction. This is in line with other studies, which reported that a noticeable influence over lipid membranes is observed at higher concentrations of cholesterol, proteins or other nanoparticles (Kahya et al., 2004; Kahya and Schwille, 2006;

Sahoo and Schwille, 2013; Bockmann et al., 2003; Machan and Hof, 2010). This effect is explained by the reduction of the free area because of tighter lipid packing. The scanned images of SAF reveal that the bilayer integrity is not altered for 16 hours after the addition of nanoparticles. Thus, the higher concentration of ZnO fluorescence intensity is significantly lower from the others presented in Fig. 4.48. The possible explanation is that the ZnO zeta potential (with pH 7.4 ~ +3 mV) could affect the lipid's mobility due to the unstable suspension caused aggregations connections to the BLM surface. As opposed to TiO_2 zeta potential variation (with pH 7.4 ~33 mV) that shows stable suspension. Experimental results suggest that the nanoparticle–membrane interaction depends on the NP charge as well as the zeta potential. Cationic nanoparticles are known to penetrate through the cell membrane. It seems evident that the binding of TiO_2- with the membrane takes place through relatively weak contacts since NP did not immerse deeply in the membrane, but floated on top of the bilayer surface, enabling diffusion of the membrane, with no adsorption to the membrane. This is in line with other studies, where it was reported that a noticeable and statistically significant ($p<0,001$) influence on phospholipid vesicles were observed after incubation of ZnO (but not TiO_2) nanoparticles (Šimundic et al., 2013).

This is known that agglomerates larger than 0.2 μm were found attached to the membrane (Rothen-Rutishauser et al., 2006), whereas smaller aggregates and single particles could probably cross the membrane through pores or ion channels (Porter et al., 2006). In addition, aggregates adhere to surfaces and may therefore cause effects without even entering cells.

The effects of NPs on BLM are important for understanding the potential effects of NPs on biological membranes. Limited biological relevance of the results of experiments with BLM does not mean that these results have no value for understanding the effects on biological membranes. It is indicated that ZnO (but not TiO_2) can cause the changes of the membrane characteristics if it can get close to the phospholipid bilayer.

4.3.2.3 Conclusions

The impact of NPs, being essential constituents of drugs and cosmetics, on the dynamics of lipid molecules in bilayer membranes were investigated. Using electrostatically attached NPs of positive charge on negatively charged supported model membranes, we demonstrated that the diffusion mobility of lipids within the GO and ZnO membrane slowed down significantly, depending on concentration and characteristics of NPs. The weak interaction was found between a stable dispersion of TiO_2 and lipid bilayers. As an explanation, we suggest a mechanism of strong interaction between nanoparticles and the negatively charged lipids, thus forming tight nanoparticle-lipid complexes. The finding that diffusion of lipid molecules within the membrane significantly depends on interaction with NP represents a new step in understanding the interactions between NP and cells by demonstrating the non-destructive nature of the NP and lipid bilayer interaction and showing the importance of NP surface properties.

4.4 The introduction into the living cell and the toxicity of graphene oxide in different cell lines

The evaluation of the cyto- and bio-compatibility is critical steps in the development of graphene oxide as a new promising material for *in vivo* biomedical applications. In this study, we report the impact of GO, with and without the addition of bovine serum albumin, on healthy (Chinese hamster ovary) and cancer (mouse hepatoma MH-22A) cell viability and the estimation of the intracellular distribution of GO inside the cells *in vitro*.

4.4.1 Influence of GO on mouse hepatoma MH-22A and CHO cell viability

The influence of GO on CHO and MH-22A cell viability was estimated using three concentrations of GO and the same concentrations of GO coated with BSA. The results of cell viability are presented in Fig. 4.50. Statistical analysis was performed by Student's t-test (*p<0.05, **p<0.01, ***p<0.005). All data of GO and GO-BSA treatment are statistically significantly different from the control (p<0.005); between 12.5 µg/ml GO and 50.0 µg/ml GO - p<0.01 (in the case of CHO cells) and p<0.05 (in the case of MH-22A cells); between 12.5 µg/ml GO-BSA and 50.0 µg/ml GO-BSA - p<0.005 (in the case of CHO cells) and p<0.05 (in the case of MH-22A cells); 12.5 µg/ml GO and 12.5 µg/ml GO–BSA, p<0.05 (in the case of both cells lines); 25.0 µg/ml GO and 25.0 µg/ml GO –BSA, p<0.05 (in the case of both cells lines) and 50.0 µg/ml GO and 50.0 µg/ml GO–BSA, p<0.005 (in the case of MH-22A cells), p<0.01 (in the case of CHO cells). Also, a statistically significant difference has been established between CHO and MH-22A cells in the cases of the treatment with 12.5, 25.0 and 50.0 µg/ml GO, p<0.05.
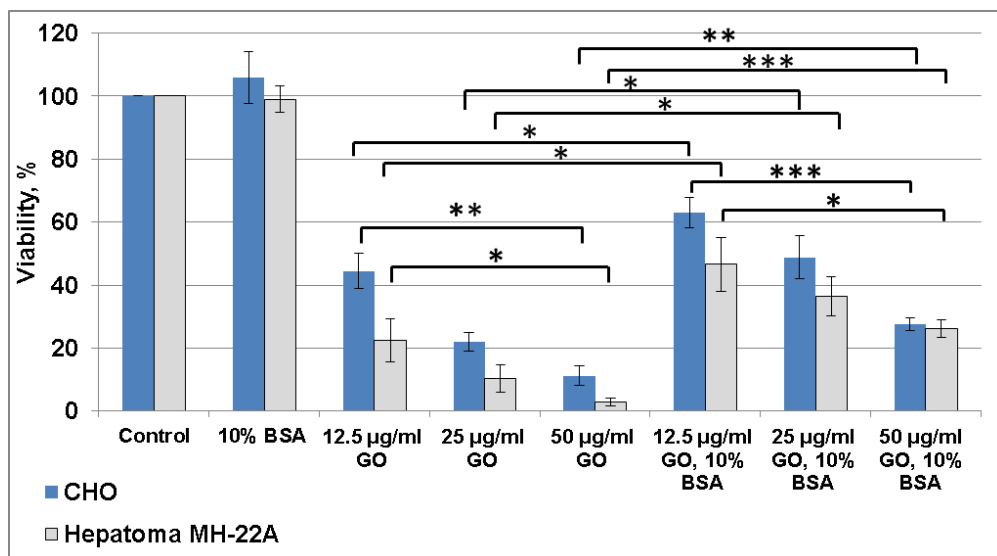
Fig. 4.50. Viability of CHO and mouse hepatoma MH-22A cells after the treatment with BSA, GO and GO-BSA at different concentrations of GO (the data were expressed as mean ± standard error (SE) from three independent experiments)

Data have shown that the viability of the cells after treatment only with BSA was indistinguishable from that of the control. The viability of MH-22A cells decreased with increasing concentrations of GO (12.5-50.0 µg/ml) from 22% to 3%, the viability of cells after treatment with GO (12.5-50.0 µg/ml)-BSA (10%) decreased from 47% to 26%. Obtained results demonstrate that the viability of MH-22A cells was higher in the case of GO-BSA use. The same tendency was observed with CHO cells: the viability of the cells decreases with increasing concentrations of GO from 44% to 11%, in the case of the use of GO-BSA - from 59% to 28%. The impact of GO on the decrease of cell viability was stronger in the case of MH-22A cells (Fig. 4.50).

On the other hand, the results suggest that BSA binds to the surface of GO to form a coating known as a "protein corona", which affects the cytotoxic action of GO and the level of GO cytotoxicity. It has already been reported that roughly one monolayer of BSA is necessary to completely cover the surface of Al_2O_3 particles and BSA starts forming dimers at the surface with increasing protein concentration through protein/protein interactions (Rezwan et al., 2004). It was established (Zhu et al., 2009) that serum proteins reduce the cellular uptake of multi-walled carbon nanoparticles and interpreted that this could happen because of decreased hydrophobicity of nanoparticles which occurred due to the binding with serum proteins. This finding suggests that in our study, BSA could reduce the cellular uptake of GO to the cells as well.

Also, the influence of functionalised GO with DOX on MH-22A cell viability was estimated using lower concentrations of GO - 6.25 µg/ml and the same concentrations of functionalised GO with DOX without heating, after heating and coated with BSA. There are few commercial doxorubicin drug forms in the market, such as injection solution, ADRIAMYCIN or lipid complex, DOXIL. The concentration of both mentioned drugs is 2 mg/ml. To prevent the symptoms of overdose (seizures, unexplained bleeding) and side-effects (nausea, vomiting, diarrhoea and loss of appetite, a reddish colour to urine, tears and sweat and temporary hair loss, etc.) the concentration of DOX for experiments with hepatoma cells was greatly reduced to 0.05 µg/ml. Results of MH-22A cell viability are presented in Fig. 4.51. The usage of functionalised with and without heating GO with cancer drug- doxorubicin even at very low concentrations of DOX (0.05 µg/ml) showed that the viability of hepatoma cells was approx. 20 percent lower than using DOX separately- from 79% to 62% and 57%, respectively. The results demonstrate that viability of hepatoma cells was higher in the case of GO/DOX-BSA use. Statistical analysis was performed by Student's t-test (*$p<0.05$, **$p<0.01$, ***$p<0.005$). All data of GO and GO-DOX, GO-DOX (after heating), GO-DOX-BSA treatment are statistically significantly different from the control ($p<0.05$); between DOX and GO-DOX, GO-DOX (after heating), GO-DOX-BSA - $p<0.005$. Wu et al. (2014) investigated cytotoxicity of graphene oxide and graphene oxide loaded with doxorubicin (50 mg/l and 2 mg/l, respectively) on human multiple myeloma cells and found GO/DOX significantly inhibited cell proliferation as compared to pure DOX ($p<0.01$). F Yang et al. (2008) also performed high-efficiency loading and controlled release of doxorubicin on graphene oxide using

concentrations of DOX 0.47 mg/ml on GO. The loading and release of DOX on GO showed strong pH dependence. Though, there are no publications which investigated the cytotoxicity of the mixture of GO/DOX in such a low concentration on hepatoma cells.
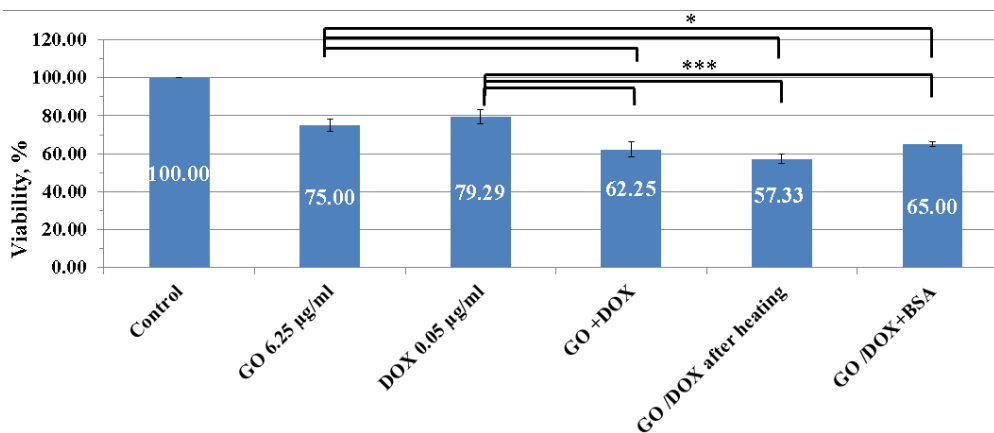
Fig. 4.51. Viability of mouse hepatoma MH-22A cells after the treatment with GO, GO+DOX, GO/DOX and GO/DOX + BSA (the data were expressed as mean ± standard error (SE) from three independent experiments)

The interaction between GO and DOX without heating may be due to the hydrogen-bonding, π-π stacking and with heating due to the covalent bond between them (Yang et al., 2008). This could be the answer why GO/DOX complex affects the viability of hepatoma cells more (~5%) than just mixed GO+DOX. However, the observed difference is not statistically significant.

It is known that the dynamics of cell growth, size and shape of the colony depend on the proliferation rate and metabolism of the cell (Huergo et al., 2012). Therefore, because GO has an influence on cell viability, it has to have an impact on the cell colony growth dynamics. In our work, we used the cell colony size differences to estimate the influence of GO on CHO and MH-22A cells. Colonies treated with GO and GO-BSA were smaller in comparison to the control. Bigger colonies possess considerably larger cell population size and a higher proportion of actively proliferating cells (Kitamura et al., 1986). The test colonies size decreased after the treatment with 12.5 µg/ml of GO. Optical micrograph of the colonies is shown in Fig. 4.52. The decrease of the colonies sizes after the treatment with GO and GO-BSA can be explained by decreased cell division and growth rate. This is in agreement with the results of other authors who supposed that cell cycle and growth rate can be perturbed after treatment with GO (Yuan et al., 2012).
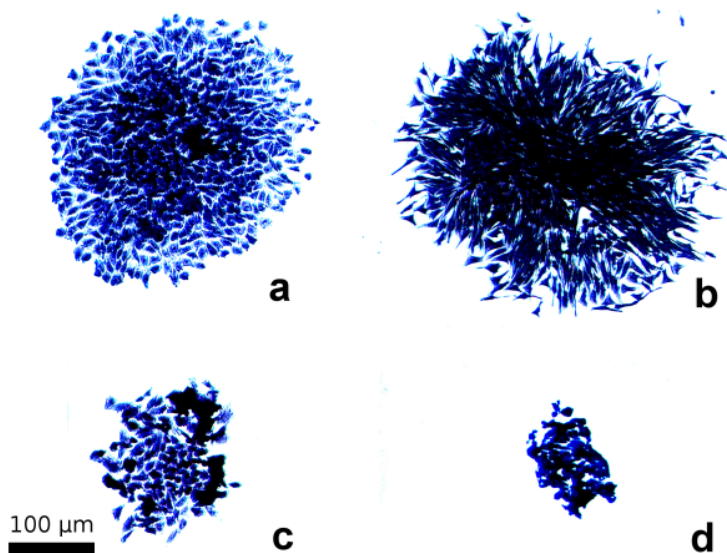
Fig. 4.52. Optical micrograph of the colonies of a) CHO control cells, b) mouse hepatoma MH-22A control cells, c) CHO cells after the treatment with 12.5 µg/ml of GO, d) mouse hepatoma MH-22A cells after the treatment with 12.5 µg/ml of GO

It is known that cells and multicellular structures can mechanically align and concentrate fibres in their extracellular matrix environment (ECM) and can sense and respond to mechanical or other cues by differentiating, branching, or disorganising. The ECM confers mechanical integrity with the tissue and provides chemical, anatomical and mechanical signals to cells, influencing differentiation, development and pathogenesis (Rauzi et al., 2009). Therefore, the single cell and colony morphology changes can be a cellular response to nanoparticles. To validate this hypothesis, we used the AFM investigation of control cells and cells after GO treatment. AFM is an established characterisation technique used for topographic imaging of different samples, including the biological cells. The ability to obtain topography images of cells allows for detailed cell morphology and roughness investigation (Franz et al., 2008; Andolfi et al., 2014; Ban et al., 2010; Oliveira et al., 2011; Toccafondi et al., 2014; Meincken, 2007) and their changes after the cell membrane interaction with nanoparticles (Lee et al., 2012). The studies have shown that surface roughness upon cellular incubation with nanoparticles changes depending on the time after incubation (Tapia-Tapia et al., 2009), this could be due to the restructuring of the membrane during the initial phase of endocytosis or this could also be a result of flattening of the cells or adaptation of the membrane in response to nanoparticle encounters (Hoskins et al. 2012).
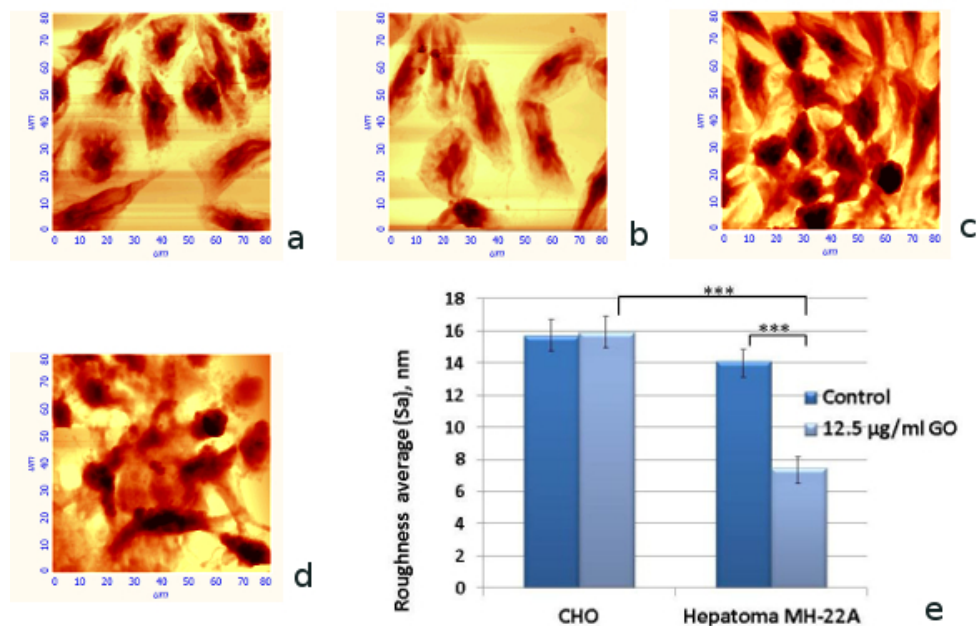
Fig. 4.53. AFM images and e) the roughness average (Sa) of a) CHO control cells, b) CHO cells after the treatment with 12.5 µg/ml of GO, c) mouse hepatoma MH-22A control cells, d) mouse hepatoma MH-22A cells after the treatment with 12.5 µg/ml of GO

AFM images of the CHO and MH-22A control cells (Fig. 4.53 a, c respectively) and cells after the treatment with 12.5 µg/ml of GO for 24 hours (Fig. 4.53 b, d respectively) were taken. The data clearly show that the structure of MH-22A cells after exposure with GO was altered substantially, part of the cells (at the central part of the image) lost plasma membrane integrity. The average roughness of the cell surface in different areas was estimated by AFM (Fig. 4.53 e). The data of roughness average were expressed as a mean ± standard error (SE) from three independent experiments. A statistically significant difference has been revealed between CHO and MH-22A cells after the treatment with 12.5 µg/ml of GO, $p < 0.005$. Also, data of GO treatment are statistically significantly different from the control, $p < 0.005$ (in the case of MH-22A cells). The average roughness of control and treated CHO cells were similar and in the range of 16 ± 3 nm, while of the MH-22A control cells were 14 ± 2 nm and treated MH-22A cells 7 ± 2 nm. The significant changes of the average roughness of the MH-22A cells after the treatment with GO confirms the impact of GO on cells membrane and probably internal structures and interconnections between the cells. MH-22A single cells as well as the cell colony network changed its mechanical structure after treatment (Fig. 4.53 d). The disorganisation of the single cell connections is clearly seen in the case of GO treatment of the MH-22A cells. This disorganisation of interconnections between cells and changes in the cell membrane structure, seen as morphology and surface roughness changes, demonstrates a strong GO influence on the biochemistry

of MH-22A cells and probably directly related with low viability of MH-22A cells after GO treatment.

4.4.2 Distribution of GO in mouse hepatoma MH-22A and CHO cells

Nanoparticle uptake and distribution inside a cell are still not well understood phenomena. In the case of GO, because of its high Raman activity, the Raman mapping (imaging) of GO is a promising technology, allowing it to work with cells in their native environment. In order to understand why GO was more cytotoxic to MH-22A cells as compared to CHO cells (Fig. 4.50), and functionalised GO with DOX and the effect of BSA (Fig. 4.51). Raman imaging was performed for an estimation of distribution of the GO in the studied cells (Fig. 4.54).
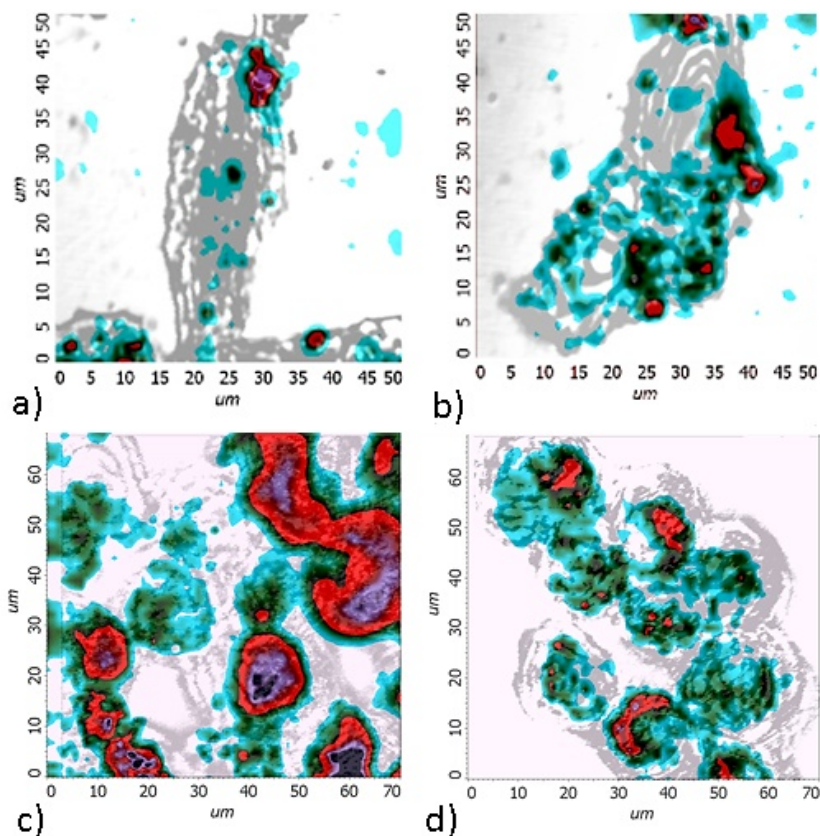
Fig. 4.54. Raman scattering images of a) GO distribution in CHO cell, b) GO distribution in mouse hepatoma MH-22A cell c) GO/DOX distribution in mouse hepatoma MH-22A cell d) GO/DOX distribution with BSA mouse hepatoma MH-22A. Intensity maps of the 'G' band of GO nanoparticles: the white colour represents the area where Raman spectra of nanoparticles were not observed, the blue - red - violet colour areas represent determined spectra of GO with increasing intensity, respectively (the optical scanning confocal image of the investigated cells as a grey background overlapped the Raman images of GO distribution)

To monitor the distribution of GO across the cell, we measured the series of Raman spectra across the cell in the Z axis, perpendicular to the cell surface, starting from the outside of the cell (Fig. 4.55). It was found that at the level of the cell membrane the Raman spectrum of GO was not observed. Positioning the laser beam with the step of 0.3 µm down into the cell the intensity of GO Raman spectra was increasing and reached maximum intensity close to the bottom membrane of the cell. These results demonstrate that GO are localised inside the cells. In comparison of GO/DOX and GO/DOX+BSA groups, after Raman spectra across the cell in the Z axis measurement the lower intensity (~24%) of GO peaks was detected inside the cells. This effect could be explained that lower Raman signals could be obtained due to protein corona which surrounds the GO nanoparticles and protects them from the negative effect to cells viability.
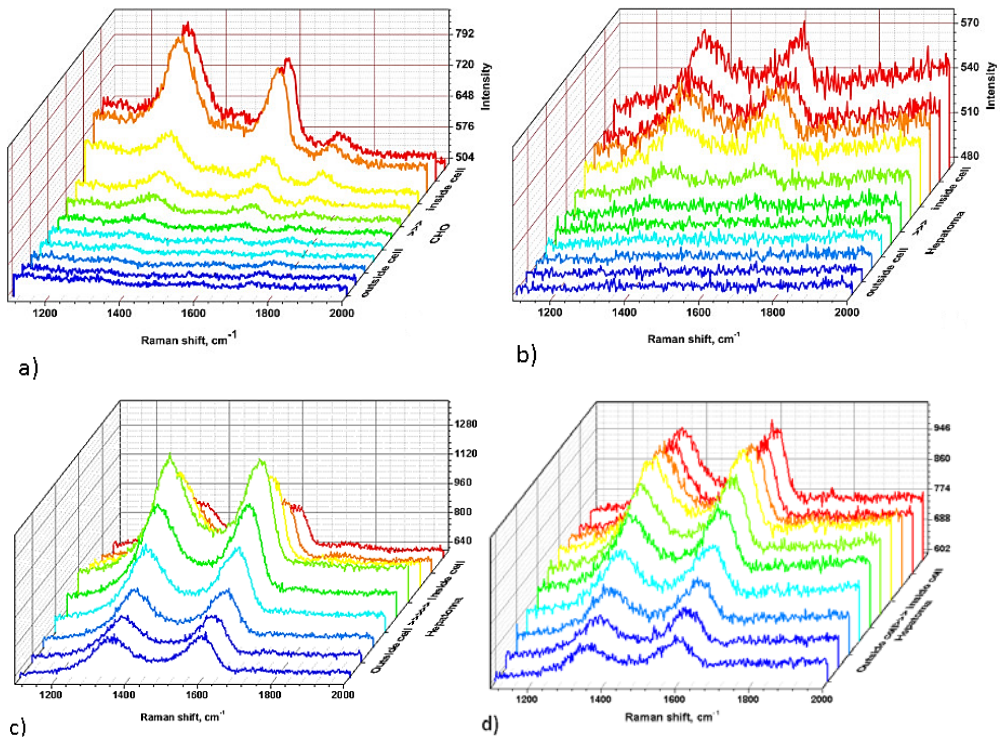
Fig. 4.55. Raman spectra recorded consistently across Z axis (the distance between each Raman spectra $\Delta z=0.3$ µm) of a) CHO cell, b) mouse hepatoma MH-22A cell after interaction with GO c) mouse hepatoma MH-22A cell after interaction with GO/DOX. d) GO/DOX distribution with BSA mouse hepatoma MH-22A (λ_{ex}- 532 nm)

Results of Raman imaging of the cells, treated with the same concentration of GO, have shown that approximately 60% of the MH-22A cells occupied surface area is filled with GO, while in the case of CHO, approx. 20% (Fig. 4.54). GO is concentrated in several spots, preferably in the periphery of cell cytoplasmic area. The Raman imaging of functionalised GO with DOX reveals more intensive areas, this means that a higher amount of functionalised GO was introduced inside the

cells. Additional BSA amounts "protect" the cells from GO/DOX influence. These findings suggest a more detailed explanation of our cell viability results: the viability of MH-22A cells is decreased more in comparison with CHO cell viability because of larger volumes of GO accumulated in these cells. A higher accumulation of GO led to a disordering of cell interconnections and changes in membrane structure (confirmed by AFM imaging) and, as a consequence, to a lower rate of cells proliferation and growth. It is difficult to explain why more GO is accumulated in MH-22A cells. Differences between the plasma membrane composition of healthy and cancer cells could be one of the reasons (Gao et al., 2013). It has already been reported that different uptake pathways are observed for gold nanoparticles in healthy (MCF-10A) and cancer (HeLa) cells (Saha et al., 2013). The results of Raman imaging are in agreement with the results of other authors who investigated the cellular internalisation of GO loaded with Au nanoparticles using surface-enhanced Raman scattering (SERS) spectroscopy. It was shown that GO was distributed inhomogeneously inside the Ca Ski cells (Huang et al., 2012). Authors (Liu et al., 2012) using Raman imaging at the different parts of the Hela 229 cells observed the different Raman intensities and proposed that the internalisation of GO in the Hela 229 cells occurs by the endocytosis pathway.

4.4.3 Conclusions

The cytotoxicity of GO was investigated with the two cell lines using colony-forming assay. Research results have shown that the viability of the cells decreased with an increased concentration of GO (in the case of CHO cells from 44% to 11%, MH-22A cells, from 22% to 3%). It was found that 50 μg/ml of GO was the critical concentration (almost all cells were killed). The usage of functionalised GO with cancer drug, doxorubicin, even at very low concentrations showed a statistically significant result, the viability of hepatoma cells was approx. 20 percent lower than using DOX separately. When nanoparticles were used with the addition of 10% BSA the viability of cells was higher because of protein corona formation on the nanoparticles. The results of cell colony assessment by optical imaging confirmed the results of the cell viability test. Raman imaging results of GO intracellular distribution in the cells suggest that the viability of MH-22A cells was decreased because a larger volume of GO was accumulated in these cells in comparison with CHO cells or with cells where GO was not functionalised. A strong GO influence on cell membrane morphology and interconnections network growth between cells was confirmed by AFM imaging. The AFM data clearly shows that GO has a different influence on the separate cells lines.

5   GENERAL CONCLUSIONS

1. The new hybrid nanostructures were synthesised by functionalisation of: graphene with iron and metal-free meso-tetra (4-sulfonatophenyl) porphines (FeTPPS and TPPS), graphene oxide with hematoporphyrin (HP), graphene oxide with meso-tetra (4-pyridyl) porphine (TPyP) and graphene oxide with anticancer drug- doxorubicin (DOX). The investigation and evaluation of synthesised nanostructures has been performed by Raman spectroscopy and imaging, Atomic force microscopy, Scanning electron microscopy, Fourier transform infrared spectroscopy, Supercritical angle fluorescence and UV-Vis spectroscopies.

2. The graphene functionalisation with iron and metal-free meso-tetra (4-sulfonatophenyl) porphines was carried out by a strong non-covalent interaction through pyrrole and desulphonated phenyl rings of closely located planar TPPS molecules on the graphene surface. The protonation of porphyrin macrocycle or the existence of a central metal atom for the TPPS family plays an important role in the molecular conformation and orientation when interacting with a single-layer graphene. Interaction between diprotonated TPPS and graphene causes the deprotonation process of porphyrin macrocycle, during which a shift in the direction of shorter wavelength for the G and 2D peaks was noticed, this could be caused by the transfer of electron charge from the TPPS molecule to graphene and it chemically strengthens Raman signals. During the interaction between deprotonated TPPS and graphene atomic changes take place, because of which new Raman bands appear. The presence of an iron atom in the porphyrin macrocycle provides stability for the FeTPPS molecule during the interaction and weakens the Raman signals, despite the effect of charge transfer.

3. The functionalisation of graphene oxide with hematoporphyrin leads to the nanocomposite of a layered structure composed of hematoporphyrin oligomers adsorbed on the surface of graphene oxide in a monolayer through covalent, electrostatic and p-stacking interactions. Nanocomposites stable in aqueous media at neutral pH hematoporphyrin/graphene oxide were obtained as a result of esterification reaction catalysed by sulfuric acid.

4. A synthesis of graphene oxide with cationic meso-tetra (4-pyridyl) porphine due to ionic self-assembly leads that a hybrid graphene oxide/TPyP nanofibre-type structures was synthesised. The investigation revealed a three-dimensional fibre structure formation under the acid conditions and leaf-like structures of the graphene oxide/TPyP assemblies under the alkaline conditions of the solution. The characterisation of obtained structures has shown the fibres can vary in diameter from tens to hundreds of nanometres and produce a network-like structure. Due this formation of the nanofibres the proposed cationic porphyrin-graphene oxide synthesis method is not suitable for drug delivery. Indeed, these network-like structures can be used in tissue engineering purposes.

5. The functionalisation of graphene oxide with the anticancer drug doxorubicin leads to the nano- and microcomposites composed of doxorubicin adsorbed on the surface of graphene oxide through covalent and non-covalent interactions, such as electrostatic and π-π stacking interactions. The formation of

such graphene oxide/doxorubicin hybrid opens the way to create drug-drug delivery systems for treating cancer and theranostics.

6. Lipid membranes, as a model for nanoparticle interactions with bio-membranes, have been formed of neutral 1,2-dioleoyl-*sn*-glycero-3-phosphocholine (DOPC) on negatively charged 1,2-dioleoyl-*sn*-glycero-3-phospho-L-serine (DOPS) phospholipids. The diffusion mobility and structural integrity of lipids was investigated by supercritical angle fluorescence spectroscopy and fluorescence correlation spectroscopy; after the interaction of lipid membrane with the graphene oxide and ZnO nanoparticle membrane slowed down significantly (D- 5-7 E-13 m^2 s^{-1}), also the weak interaction (D- 4.91 E-12 m^2 s^{-1}) was found between a stable dispersion of TiO_2 nanoparticles and lipid bilayer membranes.

7. It was approved that the transfer of graphene oxide into the cell proceeds through penetration into the membrane. The cytotoxicity of graphene oxide was investigated with the two cell lines using a colony-forming assay. Research results have shown that the viability of the cells decreased with increasing concentrations of graphene oxide (in the case of Chinese hamster ovary cells from 44% to 11%, mouse hepatoma MH-22A cells, from 22% to 3%). Raman imaging results of graphene oxide intracellular distribution in the cells suggest that the viability of MH-22A cells was decreased because a larger volume of graphene oxide was accumulated in these cells in comparison with Chinese hamster ovary cells.

8. It was found that the functionalised graphene oxide with doxorubicin strengthens the effect of doxorubicin, as an anticancer drug. It was revealed that a statistically significant result, the viability of MH-22A cells, was approx. 20% lower than using doxorubicin separately (from 57% to 79%, respectively).

6   LITERATURE

1. ABDOLHOSSEINZADEH, Sina; ASGHARZADEH, Hamed; KIM, Hyoung Seop. Fast and fully-scalable synthesis of reduced graphene oxide. *Scientific Reports*, 2015, 5

2. ADAMSON, Arthur W., et al. Physical chemistry of surfaces. 6th Ed.; *Wiley-Interscience,* New York, 1997

3. ADJEI, Isaac M.; SHARMA, Blanka; LABHASETWAR, Vinod. Nanoparticles: cellular uptake and cytotoxicity. In: *Nanomaterial. Springer Netherlands,* 2014. p. 73-91

4. ADLER, Alan D., et al. A simplified synthesis for meso-tetraphenylporphine. *The Journal of Organic Chemistry*, 1967, 32.2: 476-476.

5. AKINS, Daniel L.; ZHU, Han-Ru; GUO, Chu. Aggregation of tetraaryl-substituted porphyrins in homogeneous solution. *The Journal of Physical Chemistry,* 1996, 100.13: 5420-5425

6. ALLEN, Theresa M.; CULLIS, Pieter R. Drug delivery systems: entering the mainstream. *Science,* 2004, 303.5665: 1818-1822

7. ANDOLFI, Laura, et al. Investigation of adhesion and mechanical properties of human glioma cells by single cell force spectroscopy and atomic force microscopy. *PloS One*, 2014, 9.11: e112582

8. ANDREW, Alex M. NANOMEDICINE, VOLUME 1: BASIC CAPABILITIES, by Robert A. Freitas Jr., *Landes Bioscience*, Austin, Texas, 1999, xxi+ 509 pp., ISBN 1-57059-645-X Index (Hardback, $89.000). 2000

9. ANSLYN, Eric V.; DOUGHERTY, Dennis A. Modern physical organic chemistry. *University Science Books,* 2006

10. ARDESHIRZADEH, Behnaz, et al. Controlled release of doxorubicin from electrospun PEO/chitosan/graphene oxide nanocomposite nanofibrous scaffolds. *Materials Science and Engineering: C*, 2015, 48: 384-390

11. BACIA, Kirsten, et al. Fluorescence correlation spectroscopy relates rafts in model and native membranes. *Biophysical Journal*, 2004, 87.2: 1034-1043.

12. BAETEN, Vincent. Raman spectroscopy in lipid analysis. *Lipid Technology,* 2010, 22.2: 36-38

13. BAI, Hua, et al. A pH-sensitive graphene oxide composite hydrogel. *Chemical Communications,* 2010, 46.14: 2376-2378

14. BAI, Hua; LI, Chun; SHI, Gaoquan. Functional composite materials based on chemically converted graphene. *Advanced Materials,* 2011, 23.9: 1089-1115

15. BAI, Jingwei; HUANG, Yu. Fabrication and electrical properties of graphene nanoribbons. *Materials Science and Engineering: R: Reports*, 2010, 70.3: 341-353

16. BALANDIN, Alexander A., et al. Superior thermal conductivity of single-layer graphene. *Nano Letters,* 2008, 8.3: 902-907

17. BALCIOGLU, Mustafa; RANA, Muhit; YIGIT, Mehmet V. Doxorubicin loading on graphene oxide, iron oxide and gold nanoparticle hybrid. *Journal of Materials Chemistry B*, 2013, 1.45: 6187-6193

18. BAN, Jelena, et al. Fragmentation as a mechanism for growth cone pruning and degeneration. *Stem Cells and Development*, 2010, 20.6: 1031-1041

19. BANFI, Stefano, et al. Synthesis and photodynamic activity of a panel of BODIPY dyes. *Journal of Photochemistry and Photobiology B: Biology,* 2012, 114: 52-60

20. BINNIG, Gerd; QUATE, Calvin F.; GERBER, Ch. Atomic force microscope. *Physical Review Letters,* 1986, 56.9: 930

21. BÖCKMANN, Rainer A., et al. Effect of sodium chloride on a lipid bilayer. *Biophysical Journal*, 2003, 85.3: 1647-1655

22. BOSE, Suryasarathi; KHARE, Rupesh A.; MOLDENAERS, Paula. Assessing the strengths and weaknesses of various types of pre-treatments of carbon nanotubes on the properties of polymer/carbon nanotubes composites: A critical review. *Polymer,* 2010, 51.5: 975-993.30

23. BOSI, Susanna, et al. Fullerene derivatives: an attractive tool for biological applications. *European Journal of Medicinal Chemistry,* 2003, 38.11: 913-923

24. BRAYFIELD et al. A Martindale: The Complete Drug Reference Pharmaceutical Press. *London (UK)*, 2014

25. BUCHNER, Florian. STM Investigation of Molecular Architectures of Porphyrinoids on a Ag (111) Surface: Supramolecular Ordering, Electronic Properties and Reactivity. *Springer Science & Business Media*, 2010

26. BUNDY, Francis P. The P, T phase and reaction diagram for elemental carbon, 1979. *Journal of Geophysical Research: Solid Earth,* 1980, 85.B12: 6930-6936

27. BUSTOS-RAMÍREZ, Karina, et al. Covalently bonded chitosan on graphene oxide via redox reaction. *Materials*, 2013, 6.3: 911-926

28. BUZEA, Cristina; PACHECO, Ivan I.; ROBBIE, Kevin. Nanomaterials and nanoparticles: sources and toxicity. *Biointerphases,* 2007, 2.4: MR17-MR71

29. CANCADO, L. G., et al. General equation for the determination of the crystallite size La of nanographite by Raman spectroscopy. *Applied Physics Letters,* 2006, 88.16: 163106-163106

30. CASTELLANA, Edward T.; GAMEZ, Roberto C.; RUSSELL, David H. Label-free biosensing with lipid-functionalized gold nanorods. *Journal of the American Chemical Society,* 2011, 133.12: 4182-4185

31. CHA, TaeWoon; GUO, Athena; ZHU, X.-Y. Formation of supported phospholipid bilayers on molecular surfaces: role of surface charge

density and electrostatic interaction. *Biophysical Journal*, 2006, 90.4: 1270-1274

32. CHABOT, Victor, et al. A review of graphene and graphene oxide sponge: material synthesis and applications to energy and the environment. *Energy & Environmental Science,* 2014, 7.5: 1564-1596

33. CHANG, J. P.; LIN, Y.-S. Dielectric property and conduction mechanism of ultrathin zirconium oxide films. *Applied Physics Letters*, 2001, 79.22: 3666-3668

34. CHANG, Yanli, et al. In vitro toxicity evaluation of graphene oxide on A549 cells. *Toxicology Letters,* 2011, 200.3: 201-210

35. CHATTERJEE, Kanu, et al. Doxorubicin cardiomyopathy. *Cardiology*, 2010, 115.2

36. CHAZALET, M. Saint-Pierre, et al. Surface-enhanced Raman scattering studies of lipid planar bilayers in water. *Thin Solid Films*, 1994, 244.1: 852-856

37. CHEN, Jin-Long; YAN, Xiu-Ping. A dehydration and stabilizer-free approach to production of stable water dispersions of graphene nanosheets. *Journal of Materials Chemistry,* 2010, 20.21: 4328-4332

38. CHEN, Junlang, et al. Interaction of Graphene and its Oxide with Lipid Membrane: A Molecular Dynamic Simulation Study. *The Journal of Physical Chemistry C,* 2016

39. CHENG, Rumei, et al. Graphene oxide complex as a pH-sensitive antitumor drug. *Polymer Chemistry*, 2015, 6.13: 2401-2406.

40. CHUNG, Hoon T.; WON, Jong H.; ZELENAY, Piotr. Active and stable carbon nanotube/nanoparticle composite electrocatalyst for oxygen reduction. *Nature Communications,* 2013, 4: 1922

41. DENG, Youquan, et al. Ionic liquid as a green catalytic reaction medium for esterifications. *Journal of Molecular Catalysis A: Chemical,* 2001, 165.1: 33-36

42. DERRICK, O. NJOBUENWU; ESIO, O. OBOHO; RHODA, H. GUMUS. Determination of Contact Angle from Contact Area of Liquid Droplet Spreading on Solid Substrate. 2007

43. DOBROVOLSKAIA, Marina A., et al. Interaction of colloidal gold nanoparticles with human blood: effects on particle size and analysis of plasma protein binding profiles. *Nanomedicine: Nanotechnology, Biology and Medicine,* 2009, 5.2: 106-117

44. DOCTER, Dominic, et al. The protein corona protects against size-and dose-dependent toxicity of amorphous silica nanoparticles. *Beilstein Journal of Nanotechnology,* 2014, 5.1: 1380-1392

45. DOLMANS, Dennis EJGJ; FUKUMURA, Dai; JAIN, Rakesh K. Photodynamic therapy for cancer. *Nature Reviews Cancer,* 2003, 3.5: 380-387

46. DONG, HaiQing, et al. Poly (ethylene glycol) conjugated nano-graphene oxide for photodynamic therapy. *Science China Chemistry,* 2010, 53.11: 2265-2271

47. DOUGHERTY, Thomas J.; POTTER, William R.; WEISHAUPT, Kenneth R. *Hematoporphyrin Derivatives and Process of Preparing*. U.S. Patent No 4,866,168, 1989.

48. DRAIN, CharlesáM, et al. Synthesis of meso substituted porphyrins in air without solvents or catalysts. *Chemical Communications*, 1997, 21: 2117-2118

49. DRESSELHAUS, Mildred S.; DRESSELHAUS, Gene; EKLUND, Peter C. Science of fullerenes and carbon nanotubes: their properties and applications. *Academic Press,* 1996

50. DREYER, Daniel R.; TODD, Alexander D.; BIELAWSKI, Christopher W. Harnessing the chemistry of graphene oxide. *Chemical Society Reviews*, 2014, 43.15: 5288-5301

51. DUAN, Guangxin, et al. Protein corona mitigates the cytotoxicity of graphene oxide by reducing its physical interaction with cell membrane. *Nanoscale,* 2015, 7.37: 15214-15224

52. ELLIOTT, R., et al. Phase separation of saturated and mono-unsaturated lipids as determined from a microscopic model. *The Journal of Chemical Physics,* 2005, 122.4: 044904

53. ENDERLEIN, Jörg; RUCKSTUHL, Thomas; SEEGER, Stefan. Highly efficient optical detection of surface-generated fluorescence. *Applied Optics,* 1999, 38.4: 724-732

54. FAGADAR-COSMA, Eugenia, et al. Novel nanomaterials based on 5, 10, 15, 20-tetrakis (3, 4-dimethoxyphenyl)-21H, 23H-porphyrin entrapped in silica matrices. *Materials Research Bulletin*, 2009, 44.12: 2186-2193

55. FALVO, RaeAnne E et al. Microscale Synthesis and ^{1}H NMR Analysis of Tetraphenylporphyrins. *Journal of Chemical Education*, 1999, 76.2: 237

56. FAN, Hailong, et al. Fabrication, mechanical properties, and biocompatibility of graphene-reinforced chitosan composites. *Biomacromolecules,* 2010, 11.9: 2345-2351

57. FANG, Ming, et al. pH-responsive chitosan-mediated graphene dispersions. *Langmuir,* 2010, 26.22: 16771-16774

58. FENG, Liangzhu; LIU, Zhuang. Graphene in biomedicine: opportunities and challenges. *Nanomedicine,* 2011, 6.2: 317-324

59. FERRARI, Andrea C. Raman spectroscopy of graphene and graphite: disorder, electron–phonon coupling, doping and nonadiabatic effects. *Solid State Communications,* 2007, 143.1: 47-57

60. FERRARI, Andrea C.; ROBERTSON, Jf. Interpretation of Raman spectra of disordered and amorphous carbon. *Physical Review B*, 2000, 61.20: 14095.

61. FERRARI, Andrea. C., et al. Raman spectrum of graphene and graphene layers. *Physical Review Letters,* 2006, 97.18: 187401

62. FRANZ, C. M.; PUECH, P.-H. Atomic force microscopy: a versatile tool for studying cell morphology, adhesion and mechanics. *Cellular and Molecular Bioengineering*, 2008, 1.4: 289-300

63. FRESHNEY, R. L., et al. Culture of animal cells: a manual of basic techniques 2000. R. ISBN, 471348899

64. FRIESEN, Benjamin A., et al. New nanoscale insights into the internal structure of tetrakis (4-sulfonatophenyl) porphyrin nanorods. *The Journal of Physical Chemistry C,* 2009, 113.5: 1709-1718

65. GANDINI, Shirley CM; YUSHMANOV, Victor E.; TABAK, Marcel. Interaction of Fe (III)-and Zn (II)-tetra (4-sulfonatophenyl) porphyrins with ionic and nonionic surfactants: aggregation and binding. *Journal of Inorganic Biochemistry,* 2001, 85.4: 263-277

66. GARCÍA-SÁEZ, Ana J.; CARRER, Dolores C.; SCHWILLE, Petra. Fluorescence correlation spectroscopy for the study of membrane dynamics and organization in giant unilamellar vesicles. *Liposomes: Methods and Protocols*, Volume 2: Biological Membrane Models, 2010, 493-508.

67. GARCÍA-SÁEZ, Ana J.; SCHWILLE, Petra. Fluorescence correlation spectroscopy for the study of membrane dynamics and protein/lipid interactions. *Methods*, 2008, 46.2: 116-122.

68. GAO, Huile, et al. Ligand modified nanoparticles increases cell uptake, alters endocytosis and elevates glioma distribution and internalization. *Scientific Reports*, 2013, 3

69. GAO, Yuan, et al. Graphene oxide-based magnetic fluorescent hybrids for drug delivery and cellular imaging. *Colloids and Surfaces B: Biointerfaces,* 2013, 112: 128-133

70. GEIM, Andre K.; NOVOSELOV, Konstantin S. The rise of graphene. *Nature Materials,* 2007, 6.3: 183-191

71. GEORGAKILAS, Vasilios, et al. Functionalization of graphene: covalent and non-covalent approaches, derivatives and applications. *Chemical Reviews,* 2012, 112.11: 6156-6214

72. GIORDANI, Silvia, et al. Multifunctional hybrid materials composed of [60] fullerene-based functionalized-single-walled carbon nanotubes. *Carbon,* 2009, 47.3: 578-588

73. GONÇALVES, P. J., et al. Effect of protonation on the photophysical properties of meso-tetra (sulfonatophenyl) porphyrin. *Chemical Physics Letters,* 2005, 407.1: 236-241

74. GONÇALVES, P. J., et al. Excited state dynamics of meso-tetra (sulphonatophenyl) metalloporphyrins. *The Journal of Physical Chemistry A,* 2008, 112.29: 6522-6526

75. GRIFFITHS, Peter R.; DE HASETH, James A. *Fourier Transform Infrared Spectrometry*. John Wiley & Sons, 2007.

76. GUNSTONE, Frank D.; HARWOOD, John L.; DIJKSTRA, Albert J. *The Lipid Handbook with CD-ROM*. CRC press, 2007.

77. GUO, Shaojun; DONG, Shaojun. Graphene nanosheet: synthesis, molecular engineering, thin film, hybrids, and energy and analytical applications. *Chemical Society Reviews*, 2011, 40.5: 2644-2672

78. HAGG, Gunnar, et al. General and inorganic chemistry. *9th ed., Almqvist & Wiksell, Uppsala,* 1988

79. HANNEMANN, Klaus; SEILER, Friedrich (ed.). Shock Waves: 26th International Symposium on Shock Waves. *Springer Science & Business Media*, 2009

80. HAKIMI, Mohammad; ALIMARD, Paransa. Graphene: synthesis and applications in biotechnology-a review. 2012

81. HAMBRIGHT, PETER; SMITH, K. M. Porphyrins and Metalloporphyrins. by *KM Smith, Elsevier*, Amsterdam, 1975, 232-278

82. HAMILTON, Christopher Eric. Functionalization, coordination, and coating of carbon nanomaterials. 2009

83. HAUBOLD, A. D. Blood/carbon interactions. ASAIO journal, 1983, 6.2: 88-92

84. HE, Qiyuan, et al. Centimeter-long and large-scale micropatterns of reduced graphene oxide films: fabrication and sensing applications. *ACS Nano*, 2010, 4.6: 3201-3208

85. HE, Xiao Cong, et al. Advances in studies of nanoparticle-biomembrane interactions. *Nanomedicine,* 2015, 10.1: 121-141

86. HEIKKILÄ, Elena, et al. Atomistic simulations of anionic Au 144 (SR) 60 nanoparticles interacting with asymmetric model lipid membranes. *Biochimica et Biophysica Acta (BBA)-Biomembranes,* 2014, 1838.11: 2852-2860

87. HIANIK, Tibor; PASSECHNIK, Victor Ivanovich. Bilayer lipid membranes. Structure and mechanical properties. *Springer Science & Business Media*, 1995

88. HONG, Hao, et al. In vivo targeting and imaging of tumor vasculature with radiolabeled, antibody-conjugated nanographene. *ACS Nano*, 2012, 6.3: 2361-2370

89. HORVÁTH, Ottó, et al. Photophysics and photochemistry of kinetically labile, water-soluble porphyrin complexes. *Coordination Chemistry Reviews,* 2006, 250.13: 1792-1803

90. HOSKINS, Clare; CUSCHIERI, Alfred; WANG, Lijun. The cytotoxicity of polycationic iron oxide nanoparticles: common endpoint assays and alternative approaches for improved understanding of cellular response mechanism. *Journal of Nanobiotechnology*, 2012, 10.1: 1.

91. HU, Wenbing, et al. Graphene-based antibacterial paper. *ACS Nano,* 2010, 4.7: 4317-4323

92. HUANG, Jie, et al. Mechanism of Cellular Uptake of Graphene Oxide Studied by Surface-Enhanced Raman Spectroscopy. *Small*, 2012, 8.16: 2577-2584

93. HUANG, Jie, et al. Tracking the intracellular drug release from graphene oxide using surface-enhanced Raman spectroscopy. *Nanoscale,* 2013, 5.21: 10591-10598

94. HUANG, Xiao, et al. Graphene-based composites. *Chemical Society Reviews,* 2012, 41.2: 666-686

95. HUANG, Xiao, et al. Graphene-based materials: synthesis, characterization, properties, and applications. *Small,* 2011, 7.14: 1876-1902

96. HUERGO, M. A. C., et al. Growth dynamics of cancer cell colonies and their comparison with noncancerous cells. *Physical Review E*, 2012, 85.1: 011918.

97. IIJIMA, Sumio, et al. Helical microtubules of graphitic carbon. *Nature,* 1991, 354.6348: 56-58

98. IKAWA, Yoshiya, et al. Acid–base properties and DNA-binding of water soluble N-confused porphyrins with cationic side-arms. *Organic & Biomolecular Chemistry*, 2008, 6.22: 4157-4166

99. INHOFFEN, Hans Herloff, et al. Zur weiteren Kenntnis des Chlorophylls und des Hämins, XXX1) Photoprotoporphyrine und ihre Umwandlung in Spirographis-sowie Isospirographis-porphyrin2). *Justus Liebigs Annalen der Chemie,* 1969, 730.1: 173-185

100. JANSCH, Mirko, et al. Adsorption kinetics of plasma proteins on ultrasmall superparamagnetic iron oxide (USPIO) nanoparticles. *International Journal of Pharmaceutics,* 2012, 428.1: 125-133

101. JESLINE, A., et al. Antimicrobial activity of zinc and titanium dioxide nanoparticles against biofilm-producing methicillin-resistant Staphylococcus aureus. *Applied Nanoscience,* 2015, 5.2: 157-162

102. JIANG, Hongji. Chemical preparation of graphene-based nanomaterials and their applications in chemical and biological sensors. *Small,* 2011, 7.17: 2413-2427

103. KAH, James Chen Yong, et al. Stability of gold nanorods passivated with amphiphilic ligands. *Langmuir,* 2012, 28.24: 8834-8844

104. KAHYA, Nicoletta, et al. Lipid domain formation and dynamics in giant unilamellar vesicles explored by fluorescence correlation spectroscopy. *Journal of Structural Biology*, 2004, 147.1: 77-89

105. KAHYA, Nicoletta; SCHWILLE, Petra. How phospholipid-cholesterol interactions modulate lipid lateral diffusion, as revealed by fluorescence correlation spectroscopy. *Journal of Fluorescence*, 2006, 16.5: 671-678

106. KAPLAN, Amir; KORIN, Eli; BETTELHEIM, Armand. Structures Self-Assembled from Anionic Graphene and Cationic Manganese Porphyrin: Characterization and Application in Artificial Photosynthesis. European *Journal of Inorganic Chemistry*, 2014, 2014.13: 2288-2295

107. KARLSSON, Hanna L., et al. Cell membrane damage and protein interaction induced by copper containing nanoparticles—Importance of the metal release process. *Toxicology,* 2013, 313.1: 59-69

108. KELBAUSKAS, L., et al. Excitation relaxation and structure of TPPS 4 J-aggregates. *Journal of Luminescence,* 2003, 101.4: 253-262

109. KHENFOUCH, M., et al. Photoluminescence and dynamics of excitation relaxation in graphene oxide-porphyrin nanorods composite. *Journal of Luminescence,* 2014, 145: 33-37

110. KITAMURA, Hitoshi, et al. Morphological characterization of transformed colonies in rat tracheal epithelial cell cultures exposed to carcinogen. *Cancer Research*, 1986, 46.9: 4631-4641

111. KOTKOWIAK, M.; ŁUKASIEWICZ, J.; DUDKOWIAK, A. Photophysical and thermodynamic parameters of hematoporphyrin in solutions and monolayers. *International Journal of Thermophysics,* 2013, 34.4: 588-596

112. KOYNOVA, Rumiana; CAFFREY, Martin. Phases and phase transitions of the phosphatidylcholines. *Biochimica et Biophysica Acta (BBA)- Reviews on Biomembranes,* 1998, 1376.1: 91-145

113. KRIEG, Marianne; WHITTEN, David G. Self-sensitized photooxidation of protoporphyrin IX and related free-base porphyrins in natural and model membrane systems. Evidence for novel photooxidation pathways involving amino acids. *Journal of the American Chemical Society,* 1984, 106.8: 2477-2479

114. KRISHNA, K. Vijaya, et al. Graphene-based nanomaterials for nanobiotechnology and biomedical applications. *Nanomedicine,* 2013, 8.10: 1669-1688

115. KUDIN, Konstantin N., et al. Raman spectra of graphite oxide and functionalized graphene sheets. *Nano Letters,* 2008, 8.1: 36-41

116. KÜHLER, Paul; WEBER, Max; LOHMÜLLER, Theobald. Plasmonic Nanoantenna Arrays for Surface-Enhanced Raman Spectroscopy of Lipid Molecules Embedded in a Bilayer Membrane. *ACS applied materials & interfaces,* 2014, 6.12: 8947-8952

117. KUNDU, Janardan; LEVIN, Carly S.; HALAS, Naomi J. Real-time monitoring of lipid transfer between vesicles and hybrid bilayers on Au nanoshells using surface enhanced Raman scattering (SERS). *Nanoscale,* 2009, 1.1: 114-117

118. LEE, Haisung, et al. Functional Nanoparticles Translocation Into Cell and Adhesion Force Curve Analysis. *Journal of Nanoscience and Nanotechnology*, 2012, 12.10: 7752-7763

119. LESNIAK, Anna, et al. Effects of the presence or absence of a protein corona on silica nanoparticle uptake and impact on cells. *ACS Nano,* 2012, 6.7: 5845-5857

120. LEWIS, Ruthven NAH; MCELHANEY, Ronald N. Membrane lipid phase transitions and phase organization studied by Fourier transform infrared spectroscopy. *Biochimica et Biophysica Acta (BBA)- Biomembranes*, 2013, 1828.10: 2347-2358

121. LI, Yue, et al. Lipid and lipid oxidation analysis using surface enhanced Raman spectroscopy (SERS) coupled with silver dendrites. *Food Research International,* 2014, 58: 1-6

122. LINDER, Stefan; PINKOWSKI, Wolfhard; AEPFELBACHER, Martin. Adhesion, cytoskeletal architecture and activation status of primary human macrophages on a diamond-like carbon coated surface. *Biomaterials*, 2002, 23.3: 767-773

123. LIPOWSKY, Reinhard; SACKMANN, Erich (ed.). Structure and dynamics of membranes: I. from cells to vesicles/II. generic and specific interactions. *Elsevier,* 1995

124. LIPSON, Richard L.; BALDES, Edward J.; OLSEN, Arthur M. The Use of a Derivative of Hematoporphyrin in Tumor Detection23. 1961

125. LIU, Chang, et al. Membraneless enzymatic biofuel cells based on graphene nanosheets. *Biosensors and Bioelectronics,* 2010, 25.7: 1829-1833

126. LIU, Jia-Hui, et al. Biocompatibility of graphene oxide intravenously administrated in mice—effects of dose, size and exposure protocols. *Toxicology Research*, 2015, 4.1: 83-91

127. LIU, Qinghai, et al. Cell imaging by graphene oxide based on surface enhanced Raman scattering. *Nanoscale*, 2012, 4.22: 7084-7089

128. LIU, Zhi-Bo, et al. Porphyrin and fullerene covalently functionalized graphene hybrid materials with large nonlinear optical properties. *The Journal of Physical Chemistry B,* 2009, 113.29: 9681-9686

129. LIU, Zhuang, et al. PEGylated nanographene oxide for delivery of water-insoluble cancer drugs. *Journal of the American Chemical Society,* 2008, 130.33: 10876-10877

130. LODISH, Harvey, et al. Noncovalent bonds. 2000

131. LOH, Kian Ping, et al. Graphene oxide as a chemically tunable platform for optical applications. *Nature Chemistry*, 2010, 2.12: 1015-1024

132. LONKAR, Sunil P.; DESHMUKH, Yogesh S.; ABDALA, Ahmed A. Recent advances in chemical modifications of graphene. *Nano Research,* 2015, 8.4: 1039-1074

133. LU, Bin, et al. Nanoparticle-Membrane Interactions Studied with Lipid Bilayer Arrays. *Biophysical Journal,* 2014, 106.2: 415a

134. LU, Chun-Hua, et al. A graphene platform for sensing biomolecules. *Angewandte Chemie,* 2009, 121.26: 4879-4881

135. LUNDQVIST, Martin, et al. Nanoparticle size and surface properties determine the protein corona with possible implications for biological impacts. *Proceedings of the National Academy of Sciences,* 2008, 105.38: 14265-14270

136. LUZGINA et al. Hematoporphyrin IX Physicochemical Properties, Synthesis, Biological Activity, and Clinical Use. *Pharmaceutical Chemistry Journal,* 1977, 613-620

137. LYNCH, Iseult; DAWSON, Kenneth A. Protein-nanoparticle interactions. *Nano Today,* 2008, 3.1: 40-47

138. MACHÁŇ, Radek; HOF, Martin. Lipid diffusion in planar membranes investigated by fluorescence correlation spectroscopy. *Biochimica et Biophysica Acta (BBA)-Biomembranes*, 2010, 1798.7: 1377-1391

139. MARCANO, Daniela C., et al. Improved synthesis of graphene oxide. *ACS Nano*, 2010, 4.8: 4806-4814

140. YUTA, Nishina. Improved synthesis of graphene oxide and its application to nanocomposites. *Japanese patent No.5098064*, 2013

141. MARCHETTI, J. M.; ERRAZU, A. F. Esterification of free fatty acids using sulfuric acid as catalyst in the presence of triglycerides. *Biomass and Bioenergy,* 2008, 32.9: 892-895

142. MARQUÊS, J. T.; DE ALMEIDA, R. F. M.; VIANA, A. S. Lipid bilayers supported on bare and modified gold–Formation, characterization and relevance of lipid rafts. *Electrochimica Acta*, 2014, 126: 139-150

143. MASHETER, Adam T., et al. Investigating the reactive sites and the anomalously large changes in surface p K a value of chemically modified carbon nanotubes of different morphologies. *Journal of Materials Chemistry*, 2007, 17.25: 2616-2626.34

144. MCCLEMENTS, DavidáJulian, et al. Fabrication of lipophilic gold nanoparticles for studying lipids by surface enhanced Raman spectroscopy (SERS). *Analyst,* 2014, 139.13: 3352-3355

145. MCGILLIVRAY, Duncan J., et al. Molecular-scale structural and functional characterization of sparsely tethered bilayer lipid membranes. *Biointerphases,* 2007, 2.1: 21-33

146. MCHALE, J. L. Light-harvesting chromophore aggregates and their potential for solar energy conversion. *The Journal of Physical Chemistry Letters*, 2012, 3: 587-597

147. MEHTA, Akul. Ultraviolet-Visible (UV-Vis) Spectroscopy–Principle. *Pharma XChange,* 2011, 13: 12

148. MEINCKEN, M. Atomic force microscopy to determine the surface roughness and surface polarity of cell types of hardwoods commonly used for pulping. *Research in Action*, 2007, 103: 5

149. MIAO, Wenjun, et al. Safety and tumor tissue accumulation of pegylated graphene oxide nanosheets for co-delivery of anticancer drug and photosensitizer. *Biomaterials,* 2013, 34.13: 3402-3410

150. MIESSLER, Gary L.; TARR, Donald A. Inorganic Chemistry. *Pearson Education. Upper Saddle River, NJ,* 2004, 345

151. MINGEOT-LECLERCQ, Marie-Paule, et al. Atomic force microscopy of supported lipid bilayers. *Nature Protocols,* 2008, 3.10: 1654-1659

152. MOAN, Johan; KESSEL, David. Photoproducts formed from photofrin II in cells*. Journal of Photochemistry and Photobiology B: Biology,* 1988, 1.4: 429-436

153. MONOPOLI, Marco P., et al. Physical− chemical aspects of protein corona: relevance to in vitro and in vivo biological impacts of

nanoparticles. *Journal of the American Chemical Society,* 2011, 133.8: 2525-2534

154. NEL, Andre E., et al. Understanding biophysicochemical interactions at the nano–bio interface. *Nature Materials*, 2009, 8.7: 543-557.

155. NETO, AH Castro, et al. The electronic properties of graphene. *Reviews of Modern Physics,* 2009, 81.1: 109.

156. NI, Zhenhua, et al. Raman spectroscopy and imaging of graphene. *Nano Research,* 2008, 1.4: 273-291

157. NICOLAÏ, Adrien, et al. Molecular dynamics simulations of graphene oxide frameworks. *Journal of Chemical Theory and Computation,* 2013, 9.11: 4890-4900

158. NOVITA, Deassy I.; BOOLCHAND, P. Synthesis and structural characterization of dry Ag P O 3 glass by Raman scattering, infrared reflectance, and modulated differential scanning calorimetry. *Physical Review B*, 2007, 76.18: 184205.

159. NOVOSELOV, Kostya S., et al. Electric field effect in atomically thin carbon films. *Science,* 2004, 306.5696: 666-669

160. HUMMERS JR, William S.; OFFEMAN, Richard E. Preparation of graphitic oxide. *Journal of the American Chemical Society*, 1958, 80.6: 1339-1339.

161. OLIVEIRA, Hugo, et al. Molecular recognition force spectroscopy: a new tool to tailor targeted nanoparticles. *Small*, 2011, 7.9: 1236-1241

162. ORECCHIONI, Marco, et al. Impact of carbon nanotubes and graphene on immune cells. *Journal of Translational Medicine,* 2014, 12.1: 138

163. ORENDORFF, Christopher J., et al. Phospholipid− gold nanorod composites. *ACS Nano,* 2009, 3.4: 971-983

164. PAN, Dengyu, et al. Hydrothermal route for cutting graphene sheets into blue-luminescent graphene quantum dots. *Advanced Materials,* 2010, 22.6: 734-738

165. PAN, Yongzheng; SAHOO, Nanda Gopal; LI, Lin. The application of graphene oxide in drug delivery. *Expert Opinion on Drug delivery*, 2012, 9.11: 1365-1376

166. PATSKOVSKY, Sergiy, et al. Wide-field hyperspectral 3D imaging of functionalized gold nanoparticles targeting cancer cells by reflected light microscopy. *Journal of Biophotonics,* 2015, 8.5: 401-407

167. PAWLEY, James B. Fundamental limits in confocal microscopy. In: Handbook of biological confocal microscopy. *Springer US,* 2006. p. 20-42

168. PETERSEN, Frederic NR; NIELSEN, Claus Hélix. Raman Spectroscopy as a Tool for Investigating Lipid–Protein Interactions. *Spectroscopy,* 2009, 24.10: 1-8

169. PETIT, A., et al. Microwave irradiation in dry media: A new and easy method for synthesis of tetrapyrrolic compounds. *Synthetic Communications*, 1992, 22.8: 1137-1142

170. PHAM, Viet Hung, et al. Fast and simple fabrication of a large transparent chemically-converted graphene film by spray-coating. *Carbon*, 2010, 48.7: 1945-1951

171. PIMENTA, M. A., et al. Studying disorder in graphite-based systems by Raman spectroscopy. *Physical Chemistry Chemical Physics,* 2007, 9.11: 1276-1290

172. POGODIN, Sergey; BAULIN, Vladimir A. Coarse-grained models of phospholipid membranes within the single chain mean field theory. *Soft Matter*, 2010, 6.10: 2216-2226

173. PORTER, Alexandra E., et al. Uptake of C 60 by human monocyte macrophages, its localization and implications for toxicity: studied by high resolution electron microscopy and electron tomography. *Acta Biomaterialia,* 2006, 2.4: 409-419

174. PRABHU, Sukumaran; POULOSE, Eldho K. Silver nanoparticles: mechanism of antimicrobial action, synthesis, medical applications, and toxicity effects. *International Nano Letters,* 2012, 2.1: 1-10

175. PUMERA, Martin, et al. Graphene for electrochemical sensing and biosensing. *TrAC Trends in Analytical Chemistry*, 2010, 29.9: 954-965

176. QU, Liangti, et al. Nitrogen-doped graphene as efficient metal-free electrocatalyst for oxygen reduction in fuel cells. *ACS Nano,* 2010, 4.3: 1321-1326

177. RADMACHER, Manfred. Measuring the elastic properties of biological samples with the AFM. *Engineering in Medicine and Biology Magazine, IEEE,* 1997, 16.2: 47-57

178. RAHMAN, Masoud, et al. Protein-nanoparticle interactions. *Berlin Heidelberg: Springer*, 2013

179. RAO, C. emsp14N emsp14R, et al. Graphene: the new two-dimensional nanomaterial. *Angewandte Chemie International Edition,* 2009, 48.42: 7752-7777

180. RASSMUSSEN-TAXDAL, D. S.; WARD, Grant E.; FIGGE, Frank HJ. Fluorescence of human lymphatic and cancer tissues following high doses of intravenous hematoporphyrin. *Cancer,* 1955, 8.1: 78-81

181. RAUZI, Matteo; LECUIT, Thomas. Closing in on mechanisms of tissue morphogenesis. *Cell*, 2009, 137.7: 1183-1185

182. REN, Wen, et al. SERS imaging for label-free detection of the phospholipids distribution in hybrid lipid membrane. *Science China Chemistry,* 2011, 54.8: 1334-1341

183. REZWAN, Kurosch, et al. Bovine serum albumin adsorption onto colloidal Al2O3 particles: A new model based on Zeta potential and UV-Vis measurements. *Langmuir,* 2004, 20.23: 10055-10061

184. RICHTER, Ralf; MUKHOPADHYAY, Anneke; BRISSON, Alain. Pathways of lipid vesicle deposition on solid surfaces: a combined QCM-D and AFM study. *Biophysical Journal,* 2003, 85.5: 3035-3047

185. RÖCKER, Carlheinz, et al. A quantitative fluorescence study of protein monolayer formation on colloidal nanoparticles. *Nature Nanotechnology,* 2009, 4.9: 577-580

186. RODAITE-RISEVICIENE, Raminta; SNOPOK, Boris; SNITKA, Valentinas. In situ confocal Raman spectroscopy of single living Chinese hamster ovary cells grown on different substrates. In: *Nano/Molecular Medicine and Engineering (NANOMED), 2013 IEEE 7th International Conference on. IEEE*, 2013. p. 7-10

187. ROSSI, S. *Australian Medicines Handbook (2013 ed.). Adelaide: The Australian Medicines Handbook Unit Trust.* ISBN 978-0-9805790-9-3, 2013.

188. ROTHEMUND, Paul. A new porphyrin synthesis. The synthesis of porphin1. *Journal of the American Chemical Society*, 1936, 58.4: 625-627

189. ROTHEMUND, Paul. Formation of porphyrins from pyrrole and aldehydes. *Journal of the American Chemical Society*, 1935, 57.10: 2010-2011

190. ROTHEN-RUTISHAUSER, Barbara M., et al. Interaction of fine particles and nanoparticles with red blood cells visualized with advanced microscopic techniques. *Environmental Science & Technology,* 2006, 40.14: 4353-4359

191. ROTOMSKIS, R.; STRECKYTE, G.; BAGDONAS, S. Phototransformations of sensitizers 2. Photoproducts formed in aqueous solutions of porphyrins. *Journal of Photochemistry and Photobiology B: Biology,* 1997, 39.2: 172-175

192. ROTOMSKIS, Ricardas, et al. Hierarchical structure of TPPS4 J-aggregates on substrate revealed by atomic force microscopy. *The Journal of Physical Chemistry B*, 2004, 108.9: 2833-2838

193. RUCKSTUHL, Thomas; RANKL, Michael; SEEGER, Stefan. Highly sensitive biosensing using a supercritical angle fluorescence (SAF) instrument. *Biosensors and Bioelectronics,* 2003, 18.9: 1193-1199

194. RUCKSTUHL, Thomas; VERDES, Dorinel. Supercritical angle fluorescence (SAF) Microscopy. *Optics express,* 2004, 12.18: 4246-4254

195. SAHA, Krishnendu, et al. Surface functionality of nanoparticles determines cellular uptake mechanisms in mammalian cells. *Small*, 2013, 9.2: 300-305

196. SAHOO, Harekrushna; SCHWILLE, Petra. Influence of glycosaminoglycans on lipid dynamics in supported phospholipid bilayers. *Soft Matter*, 2013, 9.14: 3859-3865

197. SĂNDULESCU, Robert, et al. New Materials for the Construction of Electrochemical Biosensors. 2015

198. SANO, N., et al. Nanotechnology: Synthesis of carbon'onions' in water. *Nature,* 2001, 414.6863: 506-507

199. SASIDHARAN, Abhilash, et al. Hemocompatibility and macrophage response of pristine and functionalized graphene. *Small,* 2012, 8.8: 1251-1263

200. SCHNEIDER, Klaus-Peter. Computer simulation of the surface roughness of lipid membranes. *Chemical Physics Letters*, 1996, 261.1: 81-85

201. SCHUBERT, David, et al. Cerium and yttrium oxide nanoparticles are neuroprotective. *Biochemical and Biophysical Research Communications,* 2006, 342.1: 86-91

202. SCHWARTZ, S. K.; ABSOLON, K.; VERMUND, H. Some relationships of porphyrins, X-rays and tumors. *University of Minnesota Medical Bulletin,* 1955, 27: 7-8

203. SEZGIN, Erdinc; SCHWILLE, Petra. Fluorescence techniques to study lipid dynamics. *Cold Spring Harbor perspectives in biology*, 2011, 3.11: a009803.

204. SHANG, Jingzhi, et al. The origin of fluorescence from graphene oxide. *Scientific Reports,* 2012, 2

205. SHANNAHAN, Jonathan H., et al. Formation of a protein corona on silver nanoparticles mediates cellular toxicity via scavenger receptors. *Toxicological Sciences,* 2014, kfu217

206. SHEEJA, D.; TAY, B. K.; NUNG, L. N. Feasibility of diamond-like carbon coatings for orthopaedic applications. *Diamond and Related Materials*, 2004, 13.1: 184-190

207. SHEN, He, et al. Biomedical applications of graphene. *Theranostics,* 2012, 2.3: 283-294

208. SIMBERG, Dmitri, et al. Differential proteomics analysis of the surface heterogeneity of dextran iron oxide nanoparticles and the implications for their in vivo clearance. *Biomaterials,* 2009, 30.23: 3926-3933

209. SIMÓ, Carolina; CIFUENTES, Alejandro; GALLARDO, Alberto. Drug delivery systems: polymers and drugs monitored by capillary electromigration methods. *Journal of Chromatography B,* 2003, 797.1: 37-49

210. ŠIMUNDIĆ, Metka, et al. Effect of engineered TiO 2 and ZnO nanoparticles on erythrocytes, platelet-rich plasma and giant unilamelar phospholipid vesicles. *BMC Veterinary Research,* 2013, 9.1: 1.

211. SINGER, S. Jonathan; NICOLSON, Garth L. The fluid mosaic model of the structure of cell membranes. *Science,* 1972, 175.4023: 720-731

212. SMITH, Michael B.; MARCH, Jerry. March's advanced organic chemistry: reactions, mechanisms, and structure. *John Wiley & Sons,* 2007

213. SMOLUCHOWSKI, V. M. Graetz Handbuch der Electrizitat und des Magnetismus*, vol. IIVEB Georg Thieme*, Barth, Leipzig, 1921, 385

214. SNITKA, Valentinas. Graphene Based Materials: Opportunities and Challenges in Nanomedicine, *Journal of Nanomedicine Research*, 2015, 2.4: 00035

215. SNOPOK, B. A.; BOLTOVETS, P. N.; ROWELL, F. J. Simple analytical model of biosensor competition analysis for detection of low-molecular-weight analytes. *Theoretical and Experimental Chemistry*, 2006, 42.2: 106-112

216. SOETEDJO, Hariyadi; MORA, Maria F.; GARCIA, Carlos D. Optical properties of single-wall carbon nanotube films deposited on Si/SiO 2 wafers. *Thin Solid Films*, 2010, 518.14: 3954-3959.32, 33

217. SREEPRASAD, T. S.; BERRY, Vikas. How do the electrical properties of graphene change with its functionalization?. *Small*, 2013, 9.3: 341-350

218. STAMATIALIS, Dimitrios F., et al. Medical applications of membranes: drug delivery, artificial organs and tissue engineering. *Journal of Membrane Science*, 2008, 308.1: 1-34

219. ŠTEFL, Martin; KUŁAKOWSKA, Anna; HOF, Martin. Simultaneous characterization of lateral lipid and prothrombin diffusion coefficients by z-scan fluorescence correlation spectroscopy. *Biophysical Journal*, 2009, 97.3: L1-L3

220. STEINBECK, J., et al. A model for pulsed laser melting of graphite. *Journal of Applied Physics,* 1985, 58.11: 4374-4382

221. STOLLER, Meryl D., et al. Graphene-based ultracapacitors. *Nano Letters,* 2008, 8.10: 3498-3502

222. STRECKER, Edward A.; PALMER, Harold P.; BRACELAND, Francis J. Hematoporphyrin as a therapeutic agent in the psychoses. *American Journal of Psychiatry,* 1934, 90.6: 1157-1173

223. SU, Chenliang, et al. Probing the catalytic activity of porous graphene oxide and the origin of this behaviour. *Nature Communications,* 2012, 3: 1298

224. SUESS, Hans E.; UREY, Harold C. Abundances of the elements. *Reviews of Modern Physics,* 1956, 28.1: 53

225. SUGA, Keishi, et al. Membrane surface-enhanced Raman spectroscopy for sensitive detection of molecular behavior of lipid assemblies. *Analytical Chemistry*, 2015, 87.9: 4772-4780

226. SUN, Shengtong; WU, Peiyi. A one-step strategy for thermal-and pH-responsive graphene oxide interpenetrating polymer hydrogel networks. *Journal of Materials Chemistry,* 2011, 21.12: 4095-4097

227. SUN, Xiaoming, et al. Nano-graphene oxide for cellular imaging and drug delivery. *Nano Research,* 2008, 1.3: 203-212

228. SWEETENHAM, Claire S.; NOTINGHER, Ioan. Raman spectroscopy methods for detecting and imaging supported lipid bilayers. *Journal of Spectroscopy*, 2010, 24.1-2: 113-117.

229. TACAR, Oktay; SRIAMORNSAK, Pornsak; DASS, Crispin R. Doxorubicin: an update on anticancer molecular action, toxicity and novel drug delivery systems. *Journal of Pharmacy and Pharmacology*, 2013, 65.2: 157-170

230. TANG, Libin, et al. Bottom-up synthesis of large-scale graphene oxide nanosheets. *Journal of Materials Chemistry*, 2012, 22.12: 5676-5683

231. TANG, Zhen-Xing; LV, Bin-Feng. MgO nanoparticles as antibacterial agent: preparation and activity. *Brazilian Journal of Chemical Engineering,* 2014, 31.3: 591-601

232. TAPIA-TAPIA, M., et al. Nanoscopic characterization of the membrane surface of the HeLa cancer cells in the presence of the gold nanoparticles: an AFM study. *Revista Mexicana de Fisica S*, 2009, 55.1: 64-67

233. TAYEL, Ahmed A., et al. Antibacterial action of zinc oxide nanoparticles against foodborne pathogens. *Journal of Food Safety,* 2011, 31.2: 211-218

234. TEGOS, George P., et al. Cationic fullerenes are effective and selective antimicrobial photosensitizers. *Chemistry & Biology,* 2005, 12.10: 1127-1135

235. TERO, Ryugo; WATANABE, Hidekazu; URISU, Tsuneo. Supported phosopholipid bilayer formation on hydrophilicity-controlled silicon dioxide surfaces. *Physical Chemistry Chemical Physics*, 2006, 8.33: 3885-3894

236. TIAN, Bo, et al. Photothermally enhanced photodynamic therapy delivered by nano-graphene oxide. *ACS Nano,* 2011, 5.9: 7000-7009

237. TOCCAFONDI, C., et al. Thin Substrates of Anodic Porous Alumina for Living Cells Sensing. *AAC Anodizing 2014*, 2014

238. VEMULA, Venukumar; NI, Zhixu; FEDOROVA, Maria. Fluorescence labeling of carbonylated lipids and proteins in cells using coumarin-hydrazide. *Redox Biology,* 2015, 5: 195-204

239. VROMAN, L., et al. Interaction of high molecular weight kininogen, factor XII, and fibrinogen in plasma at interfaces. *Blood,* 1980, 55.1: 156-159

240. WANG, Kan, et al. Biocompatibility of graphene oxide. *Nanoscale Res Lett,* 2011, 6.8: 1

241. WANG, Lu, et al. Graphene oxide as an ideal substrate for hydrogen storage. *ACS Nano,* 2009, 3.10: 2995-3000

242. WOJTONISZAK, Malgorzata. Graphene/graphene oxide–multifunctional platform for drug delivery and photodynamic therapy in cancer treatment, 2013

243. WOOTEN, Marilyn; GORSKI, Waldemar. Facilitation of NADH electro-oxidation at treated carbon nanotubes. *Analytical Chemistry,* 2010, 82.4: 1299-1304.29

244. WU, Shaoling, et al. Adsorption properties of doxorubicin hydrochloride onto graphene oxide: equilibrium, kinetic and thermodynamic studies. *Materials,* 2013, 6.5: 2026-2042

245. WU, Shaoling, et al. Cytotoxicity of graphene oxide and graphene oxide loaded with doxorubicin on human multiple myeloma cells. *International Journal of Nanomedicine*, 2014, 9: 1413

246. WU, Si-Ying; AN, Seong Soo A.; HULME, John. Current applications of graphene oxide in nanomedicine. *International Journal of Nanomedicine*, 2015, 10: 9

247. XIE, Wenli, et al. Combination anticancer therapy activity studies for the complex of hypocrellin A and gallium ion. *Dyes and Pigments,* 2014, 101: 43-50

248. XUAN, Yi, et al. Atomic-layer-deposited nanostructures for graphene-based nanoelectronics. *Birck and NCN Publications,* 2008, 207

249. YAN, Liang, et al. The use of polyethylenimine-modified graphene oxide as a nanocarrier for transferring hydrophobic nanocrystals into water to produce water-dispersible hybrids for use in drug delivery. *Carbon,* 2013, 57: 120-129

250. YANG, Kai, et al. The influence of surface chemistry and size of nanoscale graphene oxide on photothermal therapy of cancer using ultra-low laser power. *Biomaterials*, 2012, 33.7: 2206-2214

251. YANG, Min-Quan; XU, Yi-Jun. Selective photoredox using graphene-based composite photocatalysts. *Physical Chemistry Chemical Physics,* 2013, 15.44: 19102-19118

252. YANG, Xiaoming, et al. Well-dispersed chitosan/graphene oxide nanocomposites. *ACS Applied Materials & Interfaces,* 2010, 2.6: 1707-1713

253. YANG, Xiaoying, et al. High-efficiency loading and controlled release of doxorubicin hydrochloride on graphene oxide. *The Journal of Physical Chemistry C,* 2008, 112.45: 17554-17558

254. YANG, Xiaoying, et al. Multi-functionalized graphene oxide based anticancer drug-carrier with dual-targeting function and pH-sensitivity. *Journal of Materials Chemistry,* 2011, 21.10: 3448-3454

255. YE, Ting-xiu, et al. Spectroscopic characterization of tetracationic porphyrins and their noncovalent functionalization with graphene. *Spectrochimica Acta Part A: Molecular and Biomolecular Spectroscopy,* 2012, 86: 467-471

256. YI, Xin; GAO, Huajian. Cell interaction with graphene microsheets: near-orthogonal cutting versus parallel attachment. *Nanoscale,* 2015, 7.12: 5457-5467

257. YI, Xin; SHI, Xinghua; GAO, Huajian. A universal law for cell uptake of one-dimensional nanomaterials. *Nano Letters,* 2014, 14.2: 1049-1055

258. YUAN, Jifeng, et al. Cytotoxicity evaluation of oxidized single-walled carbon nanotubes and graphene oxide on human hepatoma HepG2 cells: an iTRAQ-coupled 2D LC-MS/MS proteome analysis. *Toxicological Sciences*, 2012, 126.1: 149-161

259. ZHANG, Liming, et al. Functional graphene oxide as a nanocarrier for controlled loading and targeted delivery of mixed anticancer drugs. *Small*, 2010, 6.4: 537-544

260. ZHANG, Nan; ZHANG, Yanhui; XU, Yi-Jun. Recent progress on graphene-based photocatalysts: current status and future perspectives. *Nanoscale,* 2012, 4.19: 5792-5813

261. ZHANG, Qi, et al. Tailoring the interlayer interaction between doxorubicin-loaded graphene oxide nanosheets by controlling the drug content. *Carbon,* 2013, 51: 164-172

262. ZHANG, Weiying, et al. Enhancement of photocatalytic H2 evolution of eosin Y-sensitized reduced graphene oxide through a simple photoreaction. *Beilstein Journal of Nanotechnology*, 2014, 5.1: 801-811

263. ZHANG, Xiaoyong, et al. Distribution and biocompatibility studies of graphene oxide in mice after intravenous administration. *Carbon,* 2011, 49.3: 986-995.

264. ZHANG, Yongbin, et al. Cytotoxicity effects of graphene and single-wall carbon nanotubes in neural phaeochromocytoma-derived PC12 cells. *ACS Nano,* 2010, 4.6: 3181-3186

265. ZHAO, Jijun; CHEN, Xiaoshuang; XIE, John RH. Optical properties and photonic devices of doped carbon nanotubes. *Analytica Chimica Acta,* 2006, 568.1: 161-170.28

266. ZHOU, Ting; ZHOU, Xiaoming; XING, Da. Controlled release of doxorubicin from graphene oxide based charge-reversal nanocarrier. *Biomaterials*, 2014, 35.13: 4185-4194

267. ZHU, Yanwu, et al. Graphene and graphene oxide: synthesis, properties, and applications. *Advanced Materials,* 2010, 22.35: 3906-3924

268. ZHU, Ying, et al. Effects of serum proteins on intracellular uptake and cytotoxicity of carbon nanoparticles. *Carbon*, 2009, 47.5: 1351-1358

269. ZUO, Ping-Ping, et al. Fabrication of biocompatible and mechanically reinforced graphene oxide-chitosan nanocomposite films. *Chemistry Central Journal*, 2013, 7.1: 1.

LIST OF PUBLISHED WORKS ON THE TOPIC OF THE DISSERTATION

Publications corresponding to the list of Thomson Reuters™ Web of Science database

1. **Grinceviciute, N**., Snopok, B., & Snitka, V. (2014). Functional two-dimensional nanoarchitectures based on chemically converted graphene oxide and hematoporphyrin under the sulfuric acid treatment. *Chemical Engineering Journal*, *255*, 577-584 [IF-4.3]

2. Naumenko, D., Naumenko, I., **Grinceviciute, N.**, & Snitka, V. (2015). The interaction of iron and metal-free meso-tetra (4-sulfonatophenyl) porphines with CVD graphene: a comparative Raman spectroscopy study. *Journal of Raman Spectroscopy*, *46*(1), 94-99 [IF-2.7]

3. Batiuskaite, D., **Grinceviciute, N**., & Snitka, V. (2015). Impact of graphene oxide on viability of Chinese hamster ovary and mouse hepatoma MH-22A cells. *Toxicology in Vitro*, 29(5), 1195-1200 [IF-3.2]

4. Rodaite-Riseviciene, R., **Grinceviciute, N**., Selskis, A., & Snitka, V. (2016). Synthesis of hybrid graphene–porphyrin micro/nanofiber structures by ionic self-assembly. *Materials Letters*, *164*, 160-164 [IF-2.5]

Articles published in journal referred to in international databases

1. **Grinceviciute, N.**, Verdes, D., Snitka, V. (2015) Effect of zinc oxide and titanium dioxide nanoparticles on supported lipid bilayers. *Nanomedicine Research*, 2(3), 00030

CONFERENCES

1. D. Naumenko, I. Naumenko, N. Grinceviciute, V. Snitka. Raman spectroscopy characterisation of interaction of graphene with iron or metal-free meso-tetra (4-sulfonatophenyl) porphines. International Conference on Diamond and Carbon Materials 2013. 2–5 September 2013. Riva del Garda, Italy

2. A. Bukontaite, N. Grinceviciute, V. Snitka. The study of electroporation of variuos impulses on cell morphology" The International Conference of Natural and Life sciences 2014 COINS 3-8 March 2014 Vilnius, Lithuania

3. D. Batiuskaite, N. Grinceviciute, V. Snitka. Impact of graphene oxide on viability of mouse hepatoma MH-22A cells. 2014 International Conference of Advanced Materials 2-4 July 2014, Aveiro, Portugal

4. R. Žūkienė, N. Grincevičiūtė, L. Ramanauskaitė, V. Snitka. The effect of bovine serum albumin-coated zinc oxide nanoparticles on cell viability and ROS generation. The XIIIth International Conference of Lithuanian Biochemical Society.18-20 June 2014, Birštonas, Lithuania

5. V. Snitka, N. Grinceviciute. Synthesis and properties of gold-oligoaniline-graphene composite. ICCE-22 Malta, July 13-19, 2014 Saint Julien, Malta

6. N. Grinceviciute, B. Snopok, V. Snitka. Functional two-dimensional nanoarchitectures based on chemically converted graphene oxide and hematoporphyrin under the sulfuric acid treatment. Faraday Discussion 175. Physical Chemistry of functionalised Biomedical Nanoparticles 17-19 September 2014, Bristol, UK

7. N. Grinceviciute, L. Ramanauskaitė, V. Snitka. Investigation of bilayer lipid membranes on nanostructured Au and Ag substrates by surface enhanced Raman spectroscopy. ImagineNano 2015, 9-13 March, 2015, Bilbao, Spain

8. V. Snitka, L. Ramanauskaite, N. Grinceviciute, H.Xu. Plasmonic nanoprobes for surface enhanced Raman spectroscopy of biological molecules EMN Phuket Meeting 2015, 05 4-7, Phuket, Thailand

9. V. Snitka, L. Ramanauskaite, N. Grinceviciute and H. Xu. Investigation of amyloidogenic proteins interaction with lipid bilayers using local plasmonic probes. META'15, the 6th International Conference on Metamaterials, Photonic Crystals and Plasmonics August 4-7, 2015 New York City, USA

10. V. Snitka, L. Ramanauskaite, N. Grinceviciute. Synthesis of hybrid graphene-porphyrin nanofiber structures by ionic self-assembly. EMN Meeting Energy Materials Nanotechnology, 2015, 12 8-12, Hong Kong, China

ACKNOWLEDGEMENTS